Antenna De-Embedding for On-Body Communications with Wearables and Implants

Von der Fakultät für Elektrotechnik und Informatik
der Gottfried Wilhelm Leibniz Universität Hannover
zur Erlangung des akademischen Grades
Doktor-Ingenieur
(abgekürzt: Dr.-Ing.)
genehmigte Dissertation

von Herrn
Lukas Berkelmann, M.Sc.

2022

1. Referent:
Prof. Dr.-Ing. Dirk Manteuffel

2. Referent:
Prof. Yang Hao

Vorsitzender der Prüfungskommission:
Prof. Dr.-Ing. Holger Blume

Tag der Promotion:
26. Juli 2022

Danksagung

Diese Dissertation entstand während meiner Tätigkeit als wissenschaftlicher Mitarbeiter am Institute of Microwave and Wireless Systems der Leibniz Universität Hannover. An dieser Stelle möchte ich mich herzlichst bei allen Personen bedanken, die mich während dieser Zeit unterstützt haben.

Besonders bedanken möchte ich mich bei Prof. Dr.-Ing. Dirk Manteuffel, der mir die Möglichkeit zur Promotion gab, jederzeit für fachliche Diskussionen zur Verfügung stand und die Begeisterung für das spannende Themenfeld teilte. Außerdem möchte ich mich für die vielen Möglichkeiten, überfachliche Projektverantwortung zu übernehmen, bedanken, was mich in meiner persönlichen Entwicklung über die Promotion hinaus gehend sehr vorangebracht hat.

Mein weiterer Dank gilt Prof. Yang Hao für das Interesse an meiner Arbeit und die Erstellung des Gutachtens sowie Prof. Dr.-Ing. Holger Blume für die Übernahme des Vorsitzes der Prüfungskommission. Weiterhin möchte ich mich herzlich bei meinen ehemaligen Studenten und später Kollegen Lukas Grundmann, Leonardo Mörlein und Hendrik Jäschke bedanken, die mich vielfältig bei meinen Themen unterstützt haben. Ebenso möchte ich Dr.-Ing. Aline Friedrich und Dr.-Ing. Quang Huy Dao danken, die mir einen guten Start als wissenschaftlicher Mitarbeiter ermöglicht haben, sowie Steffen Seewald, mit dem ich anschließend lange Zeit sehr gerne ein Büro geteilt habe. Auch bei allen weiteren ehemaligen Kollegen und Kolleginnen, Saba Harke, Dr.-Ing. Nikolai Peitzmeier, Axel Hoffmann, Tim Hahn,

Henning Hartmann, Steffen Probst, Bernhard Lüers, Timo Martinelli sowie apl. Prof. Dr.-Ing. Bernd Geck, Bettina Richter und Tatjana Lehmann möchte ich mich für die kollegiale Zusammenarbeit bedanken. Außerdem sei an dieser Stelle allen Studierenden gedankt, die mich im Rahmen einer Abschlussarbeit oder als studentische Hilfskraft bei meiner Arbeit unterstützt haben.

Zusätzlich möchte ich mich bei den Mitarbeitern der Firma Sivantos bzw. WS Audiology, Oliver Nipp, Dr.-Ing. Martin Schmidt und Dr. Andreas Pfrommer bedanken, die durch die fachlichen Diskussionen im Rahmen unserer Kooperation meinen Blick für die praxisrelevanten Fragestellungen meines Promotionsthemas geschärft haben.

Schließlich bedanke ich mich bei meinen Freunden und meiner gesamten Familie, die mich stets in jeder Phase meiner Karriere unterstützt haben, insbesondere bei meiner Mutter Katja Behm und meinem Bruder Felix Berkelmann. Besonders bedanken möchte ich mich zum Schluss bei meiner Frau Maike Senne, die mir mit Ihrer Liebe und ihrem Verständnis immer Motivation gegeben hat.

Kurzfassung

Die besondere Herausforderung bei der Modellierung von am Körper getragenen und implantierbaren drahtlosen Systemen liegt in der Nahfeldkopplung der Antenne und des dissipativen Gewebes. Daher konnten bisher die Antennen nicht getrennt vom Ausbreitungskanal in der Systembeschreibung berücksichtigt werden. Aus diesem Grund werden Methoden für die systematische Antennenentwicklung von On-Body-Anwendungen entwickelt, wobei die Antennen separat (de-embedded) charakterisiert werden können. Zunächst wird eine Methode zur Charakterisierung von On-Body-Antennen entwickelt, die auf der physikalischen Modellierung der Ausbreitung entlang des Gewebes basiert. Darüber hinaus wurden On-Body-Antennenparameter abgeleitet, die eine angepasste Form der Standardantennenparameter für den freien Raum darstellen. Desweiteren wird eine Methode zur Modellierung von On-Body-Verbindungen auf Grundlage von sphärischen Wellenfunktionen entwickelt. Diese ermöglicht es, getrennte Modelle der Antennen und des Kanals auf einer höheren Abstraktionsebene zu erhalten.

Da die entwickelten On-Body-Antennenparameter in enger Anlehnung an die Standarddefinitionen für den freien Raum definiert sind, ist eine intuitive Charakterisierung von On-Body-Antennen möglich. Weiterhin wird ein Antennenmesssystem entwickelt, um die definierten Antennenparameter für physische Prototypen auswerten zu können. Wie die untersuchten Beispiele zeigen, können die On-Body-Antennenparameter und die ermittelte Übertragungsgleichung, analog

zur Friis-Gleichung im Freiraum, auch zur Modellierung des gesamten Funksystems verwendet werden. Die Schwierigkeit liegt hier jedoch in der Bestimmung des Kanalmodells, die aufwändig und nicht für jede Anwendung universell möglich ist.

Die entwickelte Methode auf Basis sphärischer Wellenfunktionen (SWF) ergänzt die Charakterisierungsmethoden, da aufgrund der numerischen Implementierung hiermit Kanäle beliebiger Komplexität modelliert werden können. Neben der Charakterisierung von On-Body-Antennen und -Kanälen stellt der Entwurf von optimierten Antennen für diese Anwendungen eine große Herausforderung dar. Mithilfe der abgeleiteten Übertragungsgleichung für On-Body Antennen kann die Antennenoptimierung direkt basierend auf den On-Body Antennenparametern erfolgen, indem der Gewinn der On-Body Antenne in Richtung des Hauptausbreitungspfads maximiert wird. Für komplexere Kanäle wird auch eine Antennenoptimierung auf der Grundlage der SWF-Modellierung entwickelt. Auf diese Weise können die optimalen Eigenschaften der Antenne auf Grundlage vieler verschiedener möglicher Kanalmodelle berechnet werden. Um auch hier eine Möglichkeit zur messtechnischen Validierung zu erhalten, werden beide entwickelten Methoden miteinander verknüpft, sodass eine Bestimmung der On-Body Antennenparameter auch auf Basis der SWF-Koeffizienten möglich ist.

Anhand mehrerer Anwendungsbeispiele konnte validiert werden, dass die entwickelten Methoden eine effiziente Modellierung sowie ein fundiertes Design von tragbaren und implantierten Antennen für die On-Body-Kommunikation ermöglichen.

Abstract

The particular challenge for modeling wearable and implantable wireless systems for on-body communications lies in the near-field coupling of the antenna and the dissipative tissue. Hence, so far, the antennas could not be considered separately from the propagation channel in the system description. Therefore, methods for the systematic antenna design of on-body applications are developed, whereas the antennas are characterized de-embedded. First, a method for characterizing on-body antennas is developed based on physical modeling of the propagation along the tissue. Furthermore, on-body antenna parameters are derived, representing an adapted form of the standard free-space antenna parameters. Secondly, a method for modeling on-body links based on spherical wave functions (SWF) is developed. It enables obtaining separate models of the antennas and the channel at a higher level of abstraction.

Since the developed on-body antenna parameters are defined closely to the standard free-space definitions, an intuitive characterization of on-body antennas is possible. Furthermore, an antenna test range is developed for assessing the defined on-body antenna parameters for physical prototypes. As shown by the examples evaluated, the on-body antenna parameters and the determined transmission equation, analogous to the Friis equation in free-space, can also be used to model the entire wireless system. However, the difficulty lies in determining the directional channel model, which is costly and not universally possible for any

application. The developed method based on SWF complements the characterization methods, as channels of any complexity can be modeled since the method could be implemented numerically.

Beyond the characterization of on-body antennas and channels, the design of optimized antennas for these applications presents a substantial challenge. Based on the derived on-body transmission equation, antenna optimization can be done directly by maximizing the on-body antenna gain in the direction of the main propagation path. For more complex channels, antenna optimization based on SWF modeling is also developed. With this, optimal characteristics of the antenna can be calculated based on many different possible channel models. To also obtain a possibility for validation with measurements here, both developed methods are linked with each other so that a determination of the on-body antenna parameters is also possible based on the optimal SWF coefficients.

With several application examples, it has been validated that the developed methods enable efficient de-embedded modeling and educated design of wearable and implanted antennas for on-body communications.

Keywords: Wireless Body Area Networks, On-Body Propagation, Wearable Antennas, Implanted Antennas, Antenna De-Embedding, Antenna Measurements, Spherical Wave Functions

Contents

List of Abbreviations and Symbols

In this work, references are marked separately for own publications and external works. For own publications, the alphabetical citation style [XY22] is used, external works are listed in the standard IEEE citation style [99].

Acronyms and formula symbols used in this work are listed below. The formula symbols do not distinguish between real and complex quantities. Vectors and matrices are marked in bold type. In addition, indices and high-indexes are used to distinguish between certain quantities.

Acronyms

AUT	Antenna under test
CTIA	Cellular Telecommunications and Internet Association
FDTD	Finite Difference Time Domain
ICNIRP	International Commission on Non-Ionizing Radiation
IEEE	Institute of Electrical and Electronics Engineers
IFA	Inverted-F antenna
ISM	Industrial, scientific, and medical
KPI	Key performance indicator
LOS	Line-of-sight
NLOS	Non-line-of-sight

OTA	Over-the-air
PLA	Polylactic acid
QZ	Quiet Zone
RCS	Radar cross-section
RF	Radio frequency
RSSI	Received signal strength indicator
SAR	Specific absorption rate
SWF	Spherical wave functions
TE	Transverse electric
TM	Transverse magnetic
WBAN	Wireless Body Area Networks

Greek Symbols

Symbol	Description	Unit
Δ	Mesh cell surface area	m^2
η_0	Wave impedance in free-space	Ohm
γ_0	Complex propagation constant of free-space	rad m^{-1}
γ_1	Complex propagation constant of tissue	m^{-1}
$\Gamma_\perp$	Fresnel reflection coefficient for normal polarization	
κ_{SW}	Surface wave attenuation factor	
λ	Wavelength	m
$\mu 0$	Vacuum permeability	NA^{-2}
$\psi_{0;1}$	Angle of direct and reflected ray	rad
ρ	Radial distance, normally distance to antenna	m

σ	Conductivity	Sm^{-1}
ε_0	Vacuum permittivity	Fm^{-1}
ε_r	Relative permittivity	
Ξ	Closed surface surrounding the antenna	m^2

Roman Symbols

Symbol	Description	Unit
F	Spherical wave function	
I	Identity matrix	
M	Channel SWF scattering matrix	
n	Surface normal	
R	SWF receiving vector	
r	Observation point	m
$\mathbf{r}'$	Point on antenna surface	m
S	Antenna SWF scattering matrix	
T	SWF transmission vector	
ϕ	Polar angle	rad
θ	Azimut angle	rad
a, **a**	SWF coeffcients of incoming waves	
A_e	Effective antenna aperture	m^2
b, **b**	SWF coeffcients of outgoing waves	
D	Maximum antenna dimension / diameter of minimum sphere enclosing the antenna	m
$D(\phi,\theta)$	Antenna directivity	m^{-1}
e	Radiation efficiency	

$E, \mathbf{E}$	Electric field strength	Vm^{-1}
f	Frequency	Hz
$F(w)$	Sommerfeld surface wave attenuation factor (half-space)	
$G(\phi,\theta)$	Free-space antenna gain	
$G, \mathbf{G}$	(Dyadic) Green's functions	
$G_B(\phi,\theta)$	On-body antenna gain	
h	Antenna height with respect to the tissue surface	m
$H, \mathbf{H}$	Magnetic field strength	Am^{-1}
j	Imaginary unit	
$J, \mathbf{J}$	Electric current density	Am^{-2}
k	Wavenumber	rad $\mathrm{m}^{-}1$
L	Path loss factor	
$M, \mathbf{M}$	Magnetic current density	Vm^{-2}
P	Power	W
$R_{0;1}$	Path length for direct and reflected wave	m^2
U	Radiation density	W / Steradian
v	Incoming wave at physical antenna port	$\sqrt{\mathrm{W}}$
W	Power density	Wm^{-2}
w	Outgoing wave at physical antenna port	$\sqrt{\mathrm{W}}$
$W(x,q)$	Creeping wave attenuation factor	m^{-1}
z	Observation point height with respect to the tissue surface	m

List of Author's Publications

This thesis contains textual materials and figures from the author's publications as listed below. The relevant publications are cited at corresponding passages, including captions of respective figures. The use of those materials requires the permission of the Institute of Electrical and Electronics Engineers (IEEE).

[BM21a] L. Berkelmann and D. Manteuffel, "Antenna parameters for on-body communications with wearable and implantable antennas", *IEEE Transactions on Antennas and Propagation*, 2021. DOI: 10.1109/TAP.2021.3060944,
The author developed the content. Prof. Manteuffel supervised the work.

[BM21b] L. Berkelmann and D. Manteuffel, "Characterization of wearable and implanted antennas: Test procedure and range design", *IEEE Transactions on Antennas and Propagation*, 2021. DOI: 10.1109/TAP.2021.3126386,
The author developed the content. Prof. Manteuffel supervised the work.

[Ber+22] L. Berkelmann, H. Jäschke, L. Mörlein, L. Grundmann, and D. Manteuffel, "Antenna optimization for WBAN based on spherical wave functions de-embedding", *IEEE Transactions on Antennas and Propagation*, 2022. DOI: 10.1109/TAP.2022.3191199,
The author was responsible for developing the idea and content of the paper. H. Jäschke, L. Mörlein and L. Grundmann developed the numerical framework for the evaluation. Prof. Manteuffel supervised the work.

[BM21c] L. Berkelmann and D. Manteuffel, "Implantable antenna design for surface-wave based in-body to on-body communications", in *2021 IEEE International Symposium on Antennas and Propagation and USNC-URSI Radio Science Meeting - AP-S/URSI*, 2021,
The author developed the content. Prof. Manteuffel supervised the work.

[BM21d] L. Berkelmann and D. Manteuffel, "On-body antenna radiation pattern measurement system", in *2021 International Conference on Electromagnetics in Advanced Applications (ICEAA)*, Aug. 2021, pp. 031–031. DOI: 10.1109/ICEAA52647.2021.9539732,
The author developed the content. Prof. Manteuffel supervised the work.

[BM19] L. Berkelmann and D. Manteuffel, "Slot antenna design with optimized on-body pattern for eyewear applications", in *2019 IEEE International Symposium on Antennas and Propagation*, 2019,
The author developed the content. Prof. Manteuffel supervised the work.

[MBM22] L. Mörlein, L. Berkelmann, and D. Manteuffel, "Antenna de-embedding in FDTD using spherical wave functions by

exploiting orthogonality", in *2022 16th European Conference on Antennas and Propagation (EuCAP)*, 2022, pp. 1–5. DOI: 10.23919/EuCAP53622.2022.9769333,
The author was involved in the development of the idea. L. Mörlein developed the content of the paper. Prof. Manteuffel supervised the work.

[MBM19] S. Meshksar, L. Berkelmann, and D. Manteuffel, "Evaluation of Bannister's subsurface-to-air model for implanted antennas", in *IEEE International Symposium on Antennas and Propagation and USNC-URSI Radio Science Meeting - AP-S/URSI*, 2019,
The author was responsible for developing the idea. S. Meshksar developed the content of the paper. Prof. Manteuffel supervised the work.

[Ber+18] L. Berkelmann, T. Martinelli, A. Friedrich, and D. Manteuffel, "Design and integration of a wearable antenna system for on and off-body communication based on 3D-MID technology", in *European Conference on Antennas and Propagation (EUCAP)*, 2018. DOI: 10.1049/cp.2018.0849,
The author was responsible for the evaluation of the on-body performance. T. Martinelli developed the antenna. A. Friedrich was responsible for the description of the MID manufacturing process. Prof. Manteuffel supervised the work.

[Gra+21] C. Grabowski, A. Pfrommer, L. Berkelmann, and D. Manteuffel, "Circuit board of a hearing aid", de, DE102019219484B4, EP3836565A1, US20210185461A1, CN112995872A, 2021, Patent, assignee: Sivantos Pte. Ltd.

Chapter 1

Introduction

Wireless body area networks (WBAN) are body-centric networks of wearable or implantable computing devices. Their applications involve medical devices, e.g., electronic implants like pacemakers, as well as devices from the consumer sector like smartwatches, which often also process medical/physiological data. Combined with personalized health management, WBAN are an essential element for future healthcare procedures. To facilitate this progress, new methods are needed to provide reliable and efficient wireless communication links.

Body-centric propagation with WBAN is usually classified into three different categories: *off-body, in-body,* and *on-body* [1]. These terms are defined as:

- *Off-body*: Only one communication node is on (wearable) or inside the body (implant). The channel is mainly influenced by the surrounding free-space.
- *In-body*: Communication between implanted transceivers. The channel is inside the body.
- *On-body*: Most of the channel is on the body surface. This can include two communication nodes on the body (wearable) or mixed combinations with communication nodes inside the body (implant).[1]

[1] The definition is slightly broadened here compared to the original definition (on-body domain only defined concerning wearable antennas) [1].

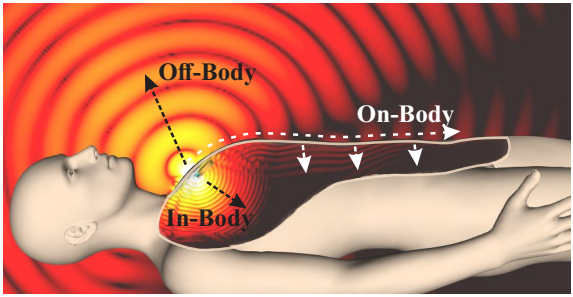

Figure 1.1: Classification of body-centric propagation.

All three categories are illustrated in Fig. 1.1. As can be seen, in the off-body domain, spherical waves travel off the body. The body leads to shadowing of the radiated fields in directions in which no line-of-sight (LOS) component is present. With in-body propagation, a high attenuation of the radiated waves is observed due to the losses inside the tissue. Thus, only short distances can be covered. This work focuses on on-body communications. In this case, as shown in Fig. 1.1, propagation takes place along the interface between the tissue and air. The fields propagate on both sides of the interface, which is why both wearable and implanted antennas can be considered in this case.

Wireless communication systems are most commonly designed and evaluated with the modeling being subdivided into the system blocks of antennas and channel. However, the standard antenna characterization methods are fundamentally linked to the assumption of free-space propagation. This fact becomes already clear from the definition of the term antenna:

> *"The antenna is a transitional structure between* ***free-space*** *and a guiding device."* -Constantine A. Balanis, *Antenna Theory* [2]

As shown in Fig. 1.1, free-space propagation can be assumed with WBAN only for the off-body domain. In the on-body domain, the propagation is very different from free-space. Thus, the standard antenna characterization methods cannot be used, and the system can only be characterized as a whole with the antennas embedded into the channel.

In standardization, WBAN network architectures are specially covered in IEEE standard 802.15.6 [3] for short-range, wireless communications in the vicinity of, or inside, the body. Standardized frequency bands are existing industrial scientific medical (ISM) bands as well as frequency bands approved by national medical and/or regulatory authorities in the range between 0.4 GHz - 2.5 GHz (narrowband) and 3 GHz - 10 GHz (ultra wideband). However, although the standard was already issued in 2012, currently there are no devices supporting it on the market [4]. Presumably, the interoperability, e.g., with widely available smartphones as WBAN user interface lead to the fact that already established standards in the 2.4 GHz ISM-band (industrial, medical, and science), like Bluetooth, are utilized for WBAN applications. Today, partly even actual medical devices like pacemakers communicate via Bluetooth [5].

Standardization concerning the characterization of antennas for WBAN is only partially established. The *IEEE Standard Test Procedures for Antennas* [6] are only applicable for free-space propagation. Thus, with regard to WBAN, these methods can only be used for off-body communications by including the human body into the antenna characteristics. This is also the basis for the *Test Plan for Over-the-Air Performance* of the Cellular Telecommunications and Internet Association (CITA) [7], which specifies standards for the measurements for off-body radiation with mobile devices and gives specifications for in-situ measurements with head and hand phantoms. In terms of safety, the *Guidelines on Limiting Exposure to Electromagnetic Fields* of the International Commission on Non-Ionizing Radiation (ICNIRP) for the protection of humans exposed to radiofrequency (RF) electromagnetic fields in the range 100 kHz to 300 GHz are most widely accepted [8]. For measuring the main limiting factor, the Specific Absorption Rate (SAR), *IEEE/IEC standard 62209-1528* specifies protocols and test procedures inside simplified models of the human body [9].

As can be seen, although many WBAN applications are long-established, standardization for the antenna performance characterization, especially for on-body links, does not exist. Hence, it can be concluded that there is not yet a universally accepted solution to the problem of antennas embedded in the channel that arises with wearable and implanted antennas for on-body communications. As a consequence thereof, the design of antennas for these systems often is still based on trial-and-error.

In this work, antenna de-embedding methods for on-body communications are evaluated to enable an educated antenna design for these applications. First, in Chapter 2, the modeling issue with wireless communications in the on-body domain is analyzed. Furthermore, the state-of-the-art is evaluated before the objectives and outline for this work are explained in more detail. Then, in Chapter 3, on-body propagation modeling is provided to gain insights into the physical propagation mechanisms. Based thereon, an on-body far-field is defined. This enables the antenna de-embedding in the form of on-body antenna parameters as described in Chapter 4. In addition, a corresponding measurement principle is introduced, and the design of a dedicated antenna test range is presented, enabling an evaluation of the defined parameters for physical prototypes. In Chapter 5, a second antenna de-embedding method for on-body communications is presented, which adds capabilities for the efficient evaluation of the antennas within more complex on-body channels. In addition, an optimization method is developed that enables the antennas to be optimally adapted to corresponding on-body channels. Finally, in Chapter 6, the developed methods are compared and discussed, also with respect to possibilities for future work.

Chapter 2

Antenna De-Embedding for On-Body Communications

Wireless systems have been analyzed and designed subdivided into the system blocks antennas and channel for a long time. The utilized Friis transmission equation is one of the most fundamental equations for modeling radio systems. Moreover, as already recognized in the original paper by Harald Friis, it is advantageous to use because of its simplicity [10]. Hence, for operation in free-space, de-embedding of antennas with wireless communication systems is performed by default. Also, measurements are usually performed independently for antenna and channel. In the following, first, a brief overview of the standard antenna characterization and wireless system modeling is given as a baseline. Based on that, the problems for on-body antenna characterization are analyzed. After that, the state-of-art for on-body antenna de-embedding is considered. Finally, detailed objectives are defined and the outline of the thesis is presented.

2.1 Free-Space Antenna Characterization

According to the *IEEE Standard Definitions of Terms for Antennas* [11], several parameters have been defined for describing the performance of antennas. In most cases, these are defined in the far-field. The definition of the far-field and its main requirements are briefly summarized in the following as the baseline for the problem analysis as well as for the adapted derivation for on-body propagation. Furthermore, the antenna parameters and the Friis transmission equation are considered, as the essentials for the de-embedding of antennas and channel in free-space. Lastly, standard channel modeling concepts and antenna measurement techniques are summarized.

2.1.1 Far-Field

The primary condition for the characterization of the antenna parameters and the modeling is that the antennas are mutually positioned in the (Fraunhofer) far-field. Here, the following properties apply [2]:

- The angular field distribution is (essentially) independent from the distance to the antenna.
- The power density W decreases with approximately $1/\rho^2$.
- The field components $\mathbf{E}$ and $\mathbf{H}$ are virtually transverse.
- The radiated waves can locally be approximated as a plane wave.

A widely accepted criterion for this approximation is the Fraunhofer distance:

$$\rho_{\mathrm{ff}} \geq \frac{2D^2}{\lambda}, \tag{2.1}$$

with D the maximum dimension of the antenna and λ the wavelength. It is derived by limiting the phase deviation over the antenna's aperture of an incoming spherical wave to a maximum of $\pi/8$ rad ($22.5°$). The equation can also be rearranged for D and a formula is obtained which gives the width of the far-field region of a point source in dependency of the distance ρ:

$$D_{\mathrm{ff}}(\rho) = \sqrt{\frac{\rho\lambda}{2}}. \tag{2.2}$$

This observation is beneficial for understanding the upcoming derivation procedure of the on-body far-field region in Chapter 3.3 and is thus evaluated in the following example. In Fig. 2.1(a), the E-field E_{h} of a point source (Hertzian dipole) radiating in free-space is depicted. As summarized above, the far-field in free-space E_{ff} is defined as a local plane wave in the direction under consideration with a decrease in the power density of $1/\rho^2$:

$$E_{\mathrm{ff}} = K_{\mathrm{e}} \frac{e^{-\gamma_0 \rho}}{\rho}, \tag{2.3}$$

with γ_0 the complex propagation constant of free-space and K_{e} a constant describing the excitation. The far-field reference fields E_{ff} are depicted in Fig. 2.1(b). The far-field region is now characterized by the condition that only negligible deviations from the far-field reference exist. Hence, in Fig. 2.1(c) and Fig. 2.1(d), the amplitude and phase deviations between the fields of the point source in Fig. 2.1(a) and the far-field reference in Fig. 2.1(b) are depicted. As can be seen, the boundary of the far-field region is described very well by (2.2).

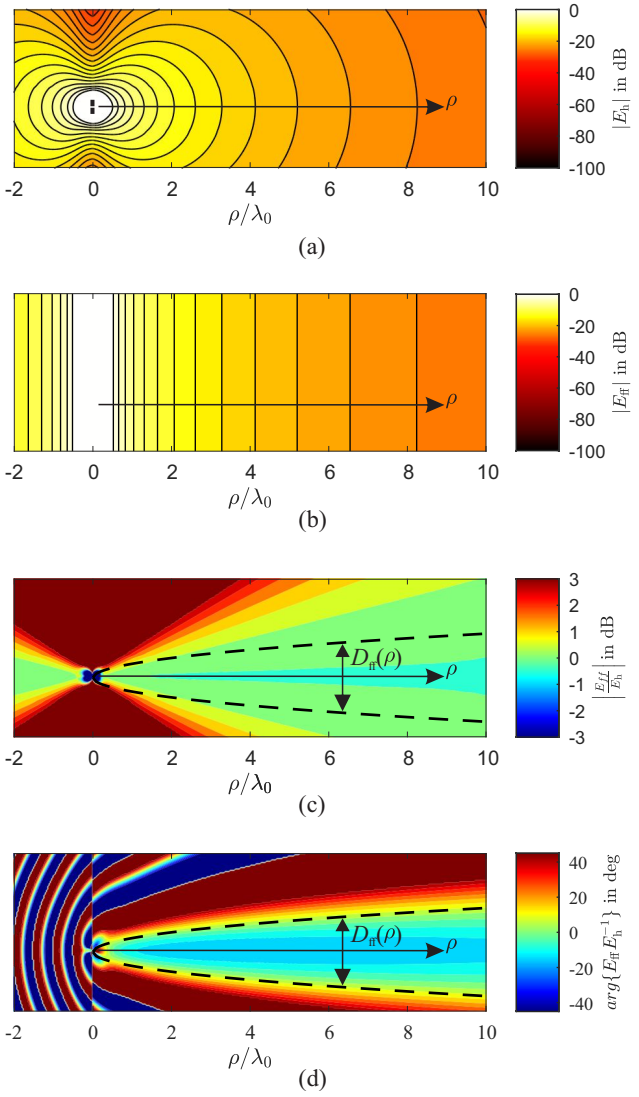

Figure 2.1: Free-space far-field region; (a) E-field of a point source (Hertzian dipole); (b) E-field of a local plane wave (far-field reference); (c) Amplitude deviation between fields of point source and local plane wave; (d) Phase deviation between fields of point source and local plane wave; Fraunhofer far-field region $D_{\mathrm{ff}}(\rho)$ is depicted by a dashed line.

2.1.2 Antenna Parameters

The directional radiation properties of an antenna are usually analyzed in spherical coordinates (θ,ϕ) in the form of the antenna radiation pattern, which is quantified in the antenna's far-field. An isotropic source, as an ideal source that radiates equally in all directions, is used as a consistent reference to obtain comparable, relative parameters. Its radiation power density W_0 is therefore given as:

$$W_0 = \frac{P_{\text{rad}}}{4\pi\rho^2}. \tag{2.4}$$

Thus, the radiated power P_{rad} is uniformly distributed on a sphere with the radius ρ. To eliminate the distance-dependency, usually, the radiation intensity as an angle-related radiation quantity is used:

$$U(\theta,\phi) = \rho^2 W(\theta,\phi). \tag{2.5}$$

The antenna directivity is defined as the ratio between the radiation intensity of the antenna over that of the isotropic source U_0, respectively the average radiation intensity over the entire solid angle of 4π:

$$D(\theta,\phi) = \frac{U(\theta,\phi)}{U_0} = \frac{4\pi U(\theta,\phi)}{P_{\text{rad}}}. \tag{2.6}$$

The antenna gain also considers losses of the antenna structure by the normalization to the power accepted P_{in} at the antenna's input terminals:

$$G(\theta,\phi) = \frac{4\pi U(\theta,\phi)}{P_{\text{in}}}. \tag{2.7}$$

The antenna's radiation efficiency as another important antenna parameter is defined as:

$$e = \frac{P_{\text{rad}}}{P_{\text{in}}} = \frac{G(\theta,\phi)}{D(\theta,\phi)}. \tag{2.8}$$

2.1.3 Friis Transmission Equation

The Friis transmission equation is used to analytically calculate the ratio between transmitted (P_t) and received power (P_r) at the terminals of the antennas of a communication system (link budget). In its simplest form it can be written as:

$$\frac{P_\mathrm{r}}{P_\mathrm{t}} = G_\mathrm{t} \underbrace{\left(\frac{\lambda}{4\pi\rho}\right)^2}_{L_\mathrm{FS}^{-1}} G_\mathrm{r}\,, \tag{2.9}$$

with G_r and G_t the gains of the receiving and transmitting antenna and ρ the separation of both antennas. The term L_FS is often called free-space loss, whereas the term "loss" does not refer to dissipation but rather to the decreasing power density with the square of the separation distance. Additionally, it accounts for the increasing effective area of the receiving isotropic antenna with the square of the wavelength [11].

2.1.4 Channel Modeling

Using the Friis equation, the power budget of a radio system can be calculated analytically for LOS free-space propagation. However, it can also be used as the basic principle for describing a radio system broken down into three system blocks of the antennas (represented by the antenna gain G) and channel (defined by the propagation loss factor L_P):

$$\frac{P_\mathrm{r}}{P_\mathrm{t}} = G_\mathrm{t}\, L_\mathrm{P}^{-1}\, G_\mathrm{r}\,. \tag{2.10}$$

For characterizing the channel, models for the loss factor L_P have been found for many different scenarios [12]. For example, in real applications, reflections from the environment occur, and multiple components that are delayed from each

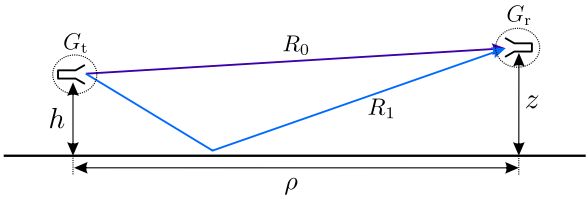

Figure 2.2: Geometry for two-ray model.

other in time and suffer different attenuation are received by an antenna. This phenomenon is summarized under the term multipath propagation. The simplest case can be described in terms of the so-called two-ray model, whereas as depicted in Fig. 2.2 in addition to the LOS ray, a reflected ray from the ground is considered. Assuming the separation ρ between both antennas to be much greater then their heights h,z above the ground ($\rho \gg h$,z) the propagation loss of this channel can be approximated as [12]:

$$L_{2-\text{ray}} = \frac{\rho^4}{h^2 z^2}. \tag{2.11}$$

Compared to the free-space loss model (2.9), it is noticeable that the power density with (2.11) decreases with the inverse fourth (instead of second) power of the distance in the far-field, which is explained by the destructive combination of the direct and reflected paths.

Channel models were also developed based on simplified geometries, which statistically consider that many different reflection paths occur in practical applications. Likewise, statistical models can be created based on channel measurements. In the simplified example in Fig. 2.2, it was assumed that the gain of the antennas is approximately constant in the direction of LOS and reflected ray. For more complex scenarios also the angles of departure and arrival of different rays at transmitter and receiver can also be taken into account. For these double-directional channel models, (2.10) can be redefined to summarize multiple propagation paths, whereas also the phase of the different waves impinging at the receiver must be considered.

All these models have in common that it is assumed that the channel has no feedback effect on the antenna, i.e., the antennas are de-embedded from the channel. This means that the interaction of the antenna with the channel takes place in the far-field of the antennas, e.g., in the form of reflections so that the antennas can be included in the transmission equation via their far-field antenna gain.

2.1.5 Measurement of Antenna Parameters

Antenna measurements ensure that the antenna meets design specifications or can be used to characterize unknown antenna structures. Standardization for this exists in the *IEEE Standard 149-1979: Test Procedures for Antennas* [6]. Antenna measurement techniques can be subdivided into near-field and far-field measurements. We will concentrate on far-field techniques here since adapting near-field measurements for WBAN with the interfering tissue seems challenging to realize. The method most commonly used to measure the absolute antenna gain is the Gain-Transfer (Gain-Comparison) method [2]. Two measurements need to be performed, one with the antenna under test (AUT) with the unknown gain G_T, and a second one with a standard antenna with known gain G_S. The unknown gain G_T can then be calculated from (2.9) as the ratio between the received power P_r in both cases, if the distance R between the antennas and the input power P_t are kept constant as:

$$\frac{\frac{P_{\mathrm{r,T}}}{P_\mathrm{t}}}{\frac{P_{\mathrm{r,S}}}{P_\mathrm{t}}} = \frac{\left(\frac{\lambda}{4\pi R}\right)^2 G_\mathrm{r} G_\mathrm{T}}{\left(\frac{\lambda}{4\pi R}\right)^2 G_\mathrm{r} G_\mathrm{S}} \quad \rightarrow \quad G_\mathrm{T} = \frac{P_{\mathrm{r,T}}}{P_{\mathrm{r,S}}} G_\mathrm{S}. \tag{2.12}$$

Since the calculation of the gain of the AUT is based on the Friis equation, free-space propagation between both antennas must be ensured, and the antennas must be sufficiently separated to ensure the far-field criteria.

2.2 On-Body Antenna Characterization

With antennas for the on-body domain, the propagation environment of the antennas differs significantly from free-space. Thus, the standard free-space modeling methods described above cannot be used without modifications. First, the differences in the wave propagation in the on-body domain are compared with free-space propagation. Then, the issues arising from this concerning the standard modeling methods are summarized. Finally, an overview of the state-of-the-art with regard to adapted wireless system modeling methods for WBAN is given as a baseline for the defining the objectives of this work.

2.2.1 Problem Analysis

As the summary of the standard modeling methods (ref. Chapter 2.1) for free-space shows, the main requirement is that the interaction between the channel and the antennas takes place in the far-field. Since there is no feedback between channel and antennas, the antennas are always de-embedded in free-space modeling. In great contrast to this, the feedback effect of the propagation environment, i.e., the body tissue, on the antenna cannot be neglected with WBAN. At the same time, the channel properties are significantly determined by the influence of the body tissue.

By reviewing the requirements of the far-field definition, ref. Chapter 2.1.1, it becomes clear that none of the required properties apply if propagation near the tissue is considered. Due to the lossy dielectric properties of the tissue, additional attenuation is observed for the propagation inside or close to the tissue. Thus, the assumption of ρ^{-2}-dependence of the power density in the far-field cannot be made. Through the scattering at the tissue surface, the angle-dependent field distribution changes continuously depending on the distance to the antenna. This

also leads to the fact that the assumption of local plane waves in the far-field has to be reevaluated for propagation with WBAN. Consequently, any definitions of criteria for the far-field approximation, e.g., the Fraunhofer far-field distance (2.1), are invalid for propagation close to the tissue.

Since the definition of the free-space antenna parameters, ref. Chapter 2.1.2, is based on the assumptions made in the definition of the far-field, there are also issues with their validity. Due to the fact that the attenuation with $L \sim \rho^{-2}$ near the tissue is no longer given, the choice of the isotropic source as a reference is not valid for characterizing antennas for the on-body domain because it leads to a range-dependency in the antenna's radiation pattern. As an example, in Fig. 2.3 the standard free-space antenna gain G_θ of short dipole antenna above an infinite half-space of muscle tissue, calculated at different distances ρ, is depicted.

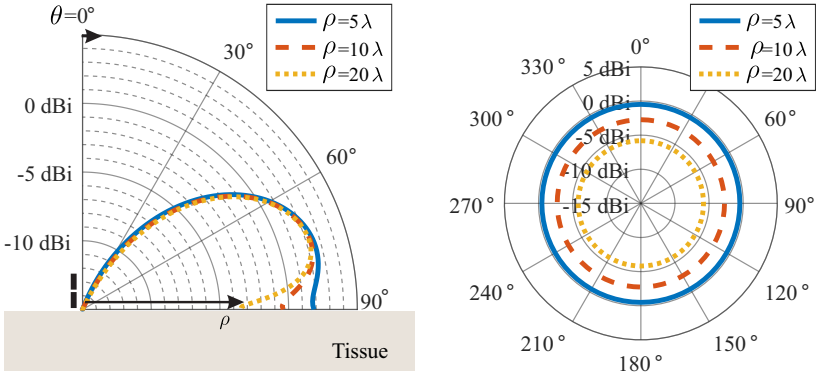

Figure 2.3: Standard free-space antenna gain G_θ of a short dipole antenna orientated normally at a height of $h = \lambda/4$ above an infinite half-space of muscle tissue at $f = 2.45\,\text{GHz}$ calculated at different distances ρ: (a) θ-cut; (b) ϕ-cut.

Due to the losses in the propagation along the tissue surface, the standard definition for the antenna gain (2.7) yields decreasing antenna gain values with increasing distance ρ. This also leads to the fact that the antenna radiation efficiency (2.8) is not constant with WBAN antennas, as the radiated Power P_{rad} decreases with increasing distance from the antenna.

The commonly utilized Friis transmission equation (2.9), respectively the general channel modeling approach (ref. Chapter 2.1.4), cannot be used for WBAN systems because of the non-constant antenna gain values. Thus, the interface between the channel and the antennas is undefined due to the absence of a valid far-field definition. Furthermore, the near-field interaction between antenna and channel prevents the definition of universally valid channel models. Therefore, especially channel measurements are not possible; respectively, their results are to be considered specific to the antennas used in the measurements.

Finally, antenna measurements according to the *IEEE Standard 149-1979: Test Procedures for Antennas* [6] are not possible for WBAN systems since these also require free-space propagation. Measurements with the antenna placed on an anatomical body phantom, as defined for example in the *CTIA Test Plan for Over-the-Air Performance* [7], can model the near-field influence of the tissue on the antenna. However, only the radiated off-body components are characterized. Furthermore, the results are specific to the body phantom used; accordingly, parts of the channel would also be included in the characterization if considered for on-body communications.

As becomes clear from the evaluation of the standard wireless system modeling methods for the on-body domain, the main problem with on-body communication lies with the antennas being embedded in the channel. Without appropriate modeling methods, goal-oriented optimization of antennas for reliable and energy-efficient on-body communications is not possible. Thus, antenna de-embedding methods must be utilized.

2.2.2 State-of-the-Art

The development of adapted methods for WBAN systems spans already a period of about 20 years. The fact that there are still no approved standards for many of the discussed issues clarifies that no generally accepted solutions have yet been found. Nevertheless, many interesting approaches have already been published, which will be addressed in the following to provide starting points for further developments. Therefore, three overall approaches for modeling wireless systems in the on-body domain have been identified as: antenna-embedded modeling, analytical modeling and antenna de-embedding.

Antenna-Embedded Modeling for On-Body Communication

Many published approaches for on-body communications circumvent the de-embedding problem by keeping the antennas embedded in the model. Channel models were developed based on measurements or numerical simulations by observing different antenna positions and body poses. The dynamic behavior of the on-body channel is taken into account in a frame-by-frame calculation of the path loss during typical movements such as walking [13]–[19]. Evaluating ultra-wideband measurements enables a detailed evaluation of channel behavior and data analysis in the time domain by examining the corresponding channel impulse responses [16], [17], [20]. The fact that the results are specific to the antennas used is partly compensated by carrying out measurements with multiple different antennas [13], [20] or alternatively infinitesimally small dipoles are utilized to approximate the characteristics of small antennas [14], [15]. The influence of different polarizations on the path loss at different positions was also investigated, taking into account normal and tangential polarization with respect to the body surface [15], [19]. Furthermore, path-loss variations with different body shapes were investigated [18], [21]. Statistical channel parameters were then derived from these simulations and measurements [15]–[17].

From these antenna-embedded evaluations, many essential properties of the on-body propagation can already be identified. Also, it is possible to define certain criteria for optimal antenna designs, for example, for the polarization. However, the numerical simulations and path gain measurements treat the whole system as a black box, and measured quantities are only available at the outer ports. Therefore, they are antenna- and subject-specific (posture, morphology/anatomy, and locations of the WBAN nodes).

Analytical Modeling for On-Body Communications

Analytical modeling for on-body communications has been extensively performed for simplified geometries [22]–[34]. Here, basic propagation mechanisms, such as available propagation modes at the tissue boundary, were investigated [22], [23]. Furthermore, the necessity of a layered tissue representation, i.e., the skin, was evaluated. The applicability of the Norton surface wave theory was investigated for on-body propagation at approximately flat tissue surfaces [22], [25], [26]. For a cylindrical approximation of the body, creeping-wave theory was considered [24], [27]–[29], [31], [33]. Green's functions have been defined for modeling the on-body propagation environment with cylindrical [24], [27], [29], [30] and spherical shapes [32]. A particularly sophisticated model was developed for the ear-to-ear channel based on creeping wave theory and the geometrical theory of diffraction [34]–[37].

The presented approaches for modeling on-body propagation have so far only taken wearable antennas into account. Analytical models have also been developed for in-body to on-body links, where the antennas are in close distance and displaced to each other mainly in the normal direction to the body surface (e.g., for wireless power transfer) [38], [39]. However, for in-body to on-body links with greater separation between the antennas, surface waves or creeping waves above the body surface play an essential role due to the high attenuation in the tissue [40], which has not been considered for the modeling so far.

With the proposed analytical modeling, it is possible to determine the coupling between simple point-source antennas (e.g., short dipoles) in the presence of the body [24], [27], [29]. For more complex structures, the described methods could be extended using an integral-equation approach [24], [29]. However, a high computational effort is necessary to consider each antenna, and no corresponding results have been presented in any publication so far. In addition, the separation between antenna and channel is still missing. Based on the development of the ear-to-ear channel model [34], it can also be seen that the development of application-specific channel models is very complex.

On-Body Antenna De-Embedding Methods

As discussed before, de-embedding the antennas from the channel is the essential issue in the on-body domain. First approaches in the form of the domain-decomposition technique compute the antenna and the human body in different computational domains [41]–[43]. Here the Huygens method, i.e., surface equivalence, is used to perform the separation. Nevertheless, these methods only reduce the computational effort; a real de-embedding of the antennas is not achieved as the input to the channel is specific to the antenna.

Antenna de-embedding based on an antenna gain, as with the standard for modeling in free-space, has also been considered for on-body propagation [28], [31], [34], [44]. Primarily, the approach was to embed the antennas into analytically calculated channels based on the standard free-space gain definition [28], [31], [34]. E.g., the free-space gain calculated at a specific body phantom, which is also used for the path loss measurements, was utilized [28], [34]. Thus, the utilized antenna gain also depends on the channel, implying an undefined separation between antenna and channel. In [31] the concept of assessing an on-body gain above a perfect conducting PEC (perfect electric conductor) plane was described, as this case is considered the reference field in the creeping wave theory [45]. However, this is only applicable for point sources as the impact of the

antenna's near-field and thus its input impedance and current distribution is different with PEC compared to the tissue in the on-body domain. Additionally, as shown in [46], the standard gain calculation of an on-body antenna with reference to the isotropic source reveals a dependency on the distance. Thus, published solutions for the calculation of an on-body gain are still subject-specific and not comparable for different applications.

Another approach for defining an antenna radiation pattern adapted for the on-body domain is based on the modeling using Norton surface wave theory and by approximating the body as an infinite half-space [44]. Instead of the normalization with the isotropic source, the fields radiated by a Hertzian dipole in the same environment as the antenna under test are utilized. However, a certain subject-specificity remains due to variable positioning of the reference Hertzian dipole with respect to the tissue.

An approach completely different from standard antenna modeling for solving the de-embedding problem with antennas for the on-body domain is based on spherical wave functions (SWF) modeling [47]. Here, the channel is characterized by the coupling between all SWF modes at the source and the receiver. Similarly, the antennas can be characterized by their ability to excite those SWF modes. Since the method can be implemented numerically, no simplification of the geometry is necessary. Although this method provides a mathematically exact solution to the de-embedding problem, it is more of a black box approach. Since the antenna and channel are characterized with complex value matrices little information about the on-body propagation behavior is given, which hinders the design of optimized antennas.

2.3 Objectives and Outline

Based on the detailed analysis of the problem and the existing approaches to its solution in the literature, the objectives and outline of this thesis are defined as follows. As the analysis shows, the main problem with modeling in the on-body domain is that antenna de-embedding methods need to be defined for enabling a definite separation between channel and antenna. A problem of existing approaches lies either in their respective specificity for certain geometries, antennas, etc., or the lack of interpretability especially with regard to the main objective of an optimized antenna design.

Hence, the aim of this contribution is to develop methods that are as general as possible and that can be applied to any on-body application without further adaptations. This should explicitly include implanted antennas, as these have not yet been modeled for the on-body domain, but practical applications already exist (e.g. pacemaker-smartphone link [5]). Furthermore, it is important to enable validating the defined parameters in measurements in order to objectively evaluate any prototypes. In addition to developing antenna characterization and modeling capabilities, it is important that these also enable an educated antenna design. Therefore, the characterization methods must yield parameters that provide information about the performance of the designed antenna within its subsequent application environment.

Among the state-of-the art approaches for solving the de-embedding problem, especially the approach of an on-body radiation pattern with an adapted normalization seems promising with regard to the defined objective of an universal antenna characterization method. Therefore, first, in Chapter 3 a method is developed for modeling the on-body propagation with wearable and implantable antennas based on dydadic Green's functions in combination with surface equivalence. Then, an on-body far-field approximation is defined as well as equations for defining the

far-field region. Based on that, in Chapter 4, adapted on-body antenna parameters are defined, whereas the definition follows closely the known principles in free-space. Finally, also the definition of an adapted transmission equation similar to the Friis equation is provided for the on-body domain. Furthermore, in Chapter 4 an antenna test range is developed for measuring the defined on-body antenna parameters.

To model the entire wireless link, i.e. to verify the antenna performance within its subsequent application, a channel model is also required. As the analysis of the state-of-the-art shows, it is difficult to find an universal method for the analytical calculation of the channel models due to the great variety of on-body application, respectively the body geometries that determine the channel behavior. Therefore, as described in Chapter 5, the on-body antenna parameters are complemented with the modeling approach based on SWF. Thus, also de-embedded channel models can be developed. The numerical implementation of this method and the associated possibility of efficient modeling of different body poses, morphologies and antenna positions furthermore enable the implementation of antenna optimization method which is also described in Chapter 5.

All methods developed throughout this thesis are subsequently evaluated based on example applications close to current commercially available devices. While the derived methods are in general independent of the frequency, for conciseness all evaluations and example application make use of the 2.4 GHz ISM-Band. Hence, for modeling the body, homogeneous muscle tissue was assumed in all evaluations. Any limitations and necessary adaptions for other frequency bands are considered subsequently in Chapter 4 and Chapter 5. In conclusion, Chapter 6 compares and discusses the developed methods as well as provides an outlook on possible future work.

Chapter 3

On-Body Propagation Modeling and Far-Field Definition

The analytical modeling of on-body propagation provides essential insights into the physical propagation mechanisms. Based thereon, fundamental requirements for associated optimal antennas can be derived. Furthermore, antenna de-embedding can be achieved by defining an on-body far-field. Overall, the problem of wireless transmission in the vicinity of the human body is very complex. The complex geometries of the human body and the high amount of different dielectric materials (tissues) involved make it basically impossible to solve the complete problem analytically. However, as shown in the following through some simplifications, analytical modeling becomes possible. First, a general propagation model is developed, which subsequently can be used as an on-body near-field to far-field transformation. Based thereon, a far-field approximation is defined for the on-body domain. Finally, limits for the on-body far-field region are derived. Thus, all fundamentals are provided for the derivation of the adapted on-body antenna parameters in Chapter 4. [2]

[2] This chapter is based on the following publications: [BM211, BM212] (©2021 IEEE).

3.1 On-Body Propagation Modeling

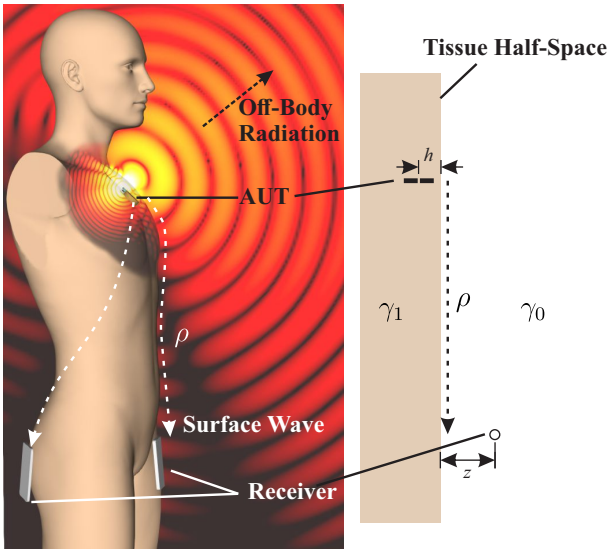

Figure 3.1: On-body propagation modeling [BM212].

Links between WBAN nodes are often non-line-of-sight, e.g., as depicted in Fig. 3.1 for the application of an implanted pacemaker that communicates with a body-worn receiver. As shown in Fig. 3.1, surface waves traveling along the body surface are crucial for these on-body links. The similarity to the so-called Sommerfeld problem of near-earth propagation can be utilized to model the propagation behavior along the tissue surface. This analogy was first discussed in [1] and its applicability to on-body propagation has been investigated, e.g., in [22], [25], [26], [44], [48].

For utilizing solutions for the Sommerfeld problem, the body surface is approximated as an infinitely extended half-space, ref. Fig. 3.1. Since the solution of the Sommerfeld problem cannot be formulated in closed-form, there have been many

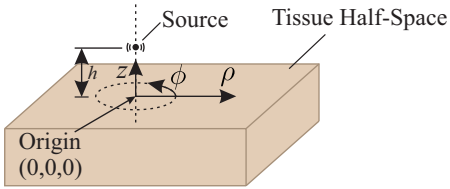

Figure 3.2: Coordinate system for on-body propagation modeling.

attempts in the literature to derive approximate formulas [49]. The formulation of Norton [50] and especially its extended form by Bannister [51] have been proven to be a suitable approximate solution for the radiation of Hertzian dipoles in the vicinity of a tissue half-space [22], [25], [48].

The solutions for the half-space problem used in the following are defined in a cylindrical coordinate system as depicted in Fig. 3.2. As can be seen, the origin is defined as the point at the tissue surface closest to the source. The z-axis is the normal pointing away from the tissue surface and the z-coordinate of the source is defined as the source height h. Negative values of the source height $(h < 0)$ for implanted antennas and positive values $(h > 0)$ for wearable antennas therefore follow from the choice of origin. Furthermore, ρ is the radial distance parallel to the tissue surface and ϕ the angular coordinate in the plane parallel to the tissue surface.

3.1.1 On-Body Green's Functions

On-body Green's functions can be defined based on the solutions of the Sommerfeld half-space problem. These are based on two fundamental solutions with the current flowing either parallel $(\parallel)$ or perpendicular $(\perp)$ to the tissue boundary, ref. Fig. 3.3, each for magnetic currents M and electric currents J. Far from the antenna with $|\gamma_0 \rho| >> 1$ the solutions of the Sommerfeld problem,

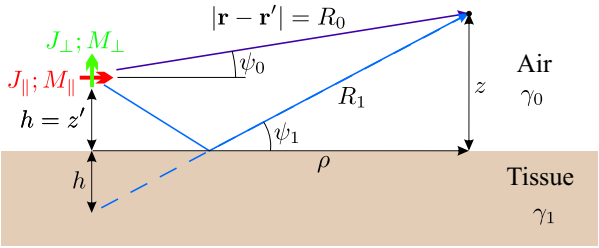

Figure 3.3: Sommerfeld half-space problem.

respectively the on-body Green's functions derived from it, can be indicated in a simplified manner. For an electric current J flowing perpendicular ($\perp$) above the tissue surface, the Green's function for the z-component of the E-field is defined as ($h > 0; z > 0$):

$$G_{\mathrm{J},\perp}^{\mathrm{E,z}} = \cos^2(\psi_0)\frac{e^{-\gamma_0 R_0}}{R_0} + \Gamma_\perp \cos^2(\psi_1)\frac{e^{-\gamma_0 R_1}}{R_1} + (1-\Gamma_\perp)F(w)\cos^2(\psi_1)\frac{e^{-\gamma_0 R_1}}{R_1}, \tag{3.1}$$

where γ_0 is the complex propagation constant of air. R_0, R_1, ψ_0 and ψ_1 are the lengths and elevation angles of direct and reflected paths from the source currents (ref. Fig. 3.3). $\Gamma_\perp$ is the specular reflection coefficient for perpendicular-polarized waves and $F(w)$ is the Sommerfeld surface wave attenuation factor with the numerical distance w which depends on geometry and material parameters. Other than in free-space, the Green's functions not only depend on the distance $\mathbf{r} - \mathbf{r}'$ between source and observation point, but also directly on the height h of the source above the tissue boundary (in the selected coordinate system, ref. Fig 3.3, $h = z'$).

Equation (3.1) illustrates Norton's observation that the fields above a dissipative ground (in our case the tissue) can be described in terms of three quasi-optical

components. The first term can be seen as a direct wave along R_0, ref. Fig. 3.3. The second term can be described as a reflected wave along R_1 and the third term as a so-called Norton surface wave component. Although, at first sight, the solutions look like a far-field solution with plane wave reflections, e.g. like the two-ray channel model (ref. Chapter 2.1.4), the antenna's near-field interaction with the tissue is also solved correctly within the Norton surface wave term by the spectral decomposition of the spherical waves.

If also implantable antennas are considered, the height h of radiating current element and/or the observer height z (ref. Fig. 3.3) becomes negative. Green's functions can also be obtained for these cases, whereas the solution with both transmitter and observer in air serves as the basis. As derived by Bannister [51], the Green's functions can be formulated for the current element inside the tissue ($h < 0$) as:

$$G(h < 0) = G(h = 0)e^{\gamma_1 h}. \tag{3.2}$$

In addition, the solution for the perpendicular electrical current must be multiplied by $\gamma_1^2\gamma_0^{-2}$ for fulfilling the boundary condition at the tissue surface[3]. This causes the paths R_0 and R_1 to be of equal length and the angles ψ_0 and ψ_1 to be of equal value. Similarly, the solutions for the observer inside the tissue ($z < 0$) are defined as [51]:

$$G(z < 0) = G(z = 0)e^{\gamma_1 z}. \tag{3.3}$$

In this case, for fulfilling the boundary condition at the tissue surface, all Green's functions for the z-polarized E-field (perpendicular component at the interface) must be multiplied by $\gamma_1^2\gamma_0^{-2}$. Finally, for both transmitter and observer inside the tissue the solution is defined by [51]:

$$G(h < 0, z < 0) = G(h = 0, z = 0)e^{\gamma_1(h+z)}. \tag{3.4}$$

[3]The resulting individual Green's functions are listed in Appendix A.

As before, the factor $\gamma_1^2\gamma_0^{-2}$ applies for all Green's functions for the z-polarized E-field and additionally for the perpendicular electrical current elements.

In summary, the individual terms for the different polarizations can be summarized in form of dyadic Green's functions $\overline{\mathbf{G}}_{\mathrm{J}}^{\mathrm{E}}$ and $\overline{\mathbf{G}}_{\mathrm{M}}^{\mathrm{E}}$ for calculating the E-field in presence of the tissue halfspace in cylindrical coordinates (z-axis normal on tissue surface) as:

$$\overline{\mathbf{G}}_{\mathrm{J}}^{\mathrm{E}} = \frac{\gamma_0\eta_0}{4\pi}\begin{pmatrix} G_{\mathrm{J},\parallel}^{\mathrm{E},\rho} & 0 & G_{\mathrm{J},\perp}^{\mathrm{E},\rho} \\ 0 & G_{\mathrm{J},\parallel}^{\mathrm{E},\phi} & 0 \\ G_{\mathrm{J},\parallel}^{\mathrm{E},\mathrm{z}} & 0 & G_{\mathrm{J},\perp}^{\mathrm{E},\mathrm{z}} \end{pmatrix}, \tag{3.5}$$

$$\overline{\mathbf{G}}_{\mathrm{M}}^{\mathrm{E}} = \frac{\gamma_0}{4\pi}\begin{pmatrix} 0 & G_{\mathrm{M},\parallel}^{\mathrm{E},\rho} & 0 \\ G_{\mathrm{M},\parallel}^{\mathrm{E},\phi} & 0 & G_{\mathrm{M},\perp}^{\mathrm{E},\phi} \\ 0 & G_{\mathrm{M},\parallel}^{\mathrm{E},\mathrm{z}} & 0 \end{pmatrix}. \tag{3.6}$$

All individual terms are listed in Appendix A. The magnetic field's Green's function can be derived equivalently.

3.1.2 Surface Equivalence for On-Body Propagation Modeling

The solutions above serve only for calculating the fields of small dipole antennas. In [44] it was shown that on-body fields of arbitrary antennas can be modeled by decomposing the antenna's current distribution into small electric dipoles. However, some difficulties arise when utilizing this method for typical WBAN applications, e.g., for characterizing hearing aid antennas. If the antenna is positioned in close proximity to protruding body parts whose near-field influence cannot be approximated well by the half-space, e.g., the pinna, this modeling approach fails to reproduce the radiated fields correctly.

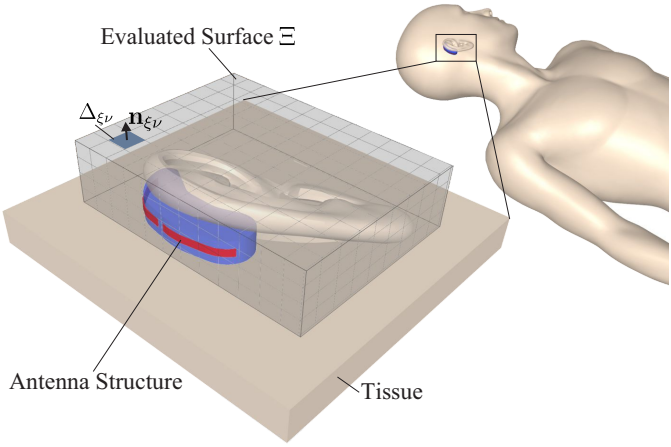

Figure 3.4: Surface equivalence for on-body propagation modeling. The antenna's near-field is evaluated on an enclosing surface Ξ. For a numerical implementation, the discretized fields (mesh cell $\Delta_{\xi\nu}$) can be processed using (3.10).

Using the surface equivalence theorem, the actual antenna can be replaced by equivalent currents on a closed surface Ξ enclosing the original sources, as shown in Fig. 3.4. The choice of the surface is free; it can be above the tissue, intersect with the tissue boundary (as for the hearing aid antenna in Fig. 3.4) or be inside the tissue. Setting the fields inside the surface to zero, the equivalent electric and magnetic source current densities $\mathbf{J}_\mathrm{s}$ and $\mathbf{M}_\mathrm{s}$ flowing on the surface Ξ can be calculated as [52]:

$$\mathbf{J}_\mathrm{s}(\mathbf{r}') = \mathbf{n} \times \mathbf{H}(\mathbf{r}'), \tag{3.7}$$

$$\mathbf{M}_\mathrm{s}(\mathbf{r}') = -\mathbf{n} \times \mathbf{E}(\mathbf{r}'), \tag{3.8}$$

where $\mathbf{E}(\mathbf{r}')$ and $\mathbf{H}(\mathbf{r}')$ are the (numerically) calculated near-fields of the antenna on the surface Ξ and $\mathbf{n}$ is the surface normal pointing outwards the closed surface.

The fields radiated by the structure inside Ξ can be then calculated using the dyadic on-body Green's functions (3.5) and (3.6) as:

$$\mathbf{E}(\mathbf{r}) = \oiint_{\Xi} \left[\overline{\mathbf{G}}_{\mathrm{J}}^{\mathrm{E}}(\mathbf{r},\mathbf{r}') \cdot \mathbf{J}_{\mathrm{s}}(\mathbf{r}') + \overline{\mathbf{G}}_{\mathrm{M}}^{\mathrm{E}}(\mathbf{r},\mathbf{r}') \cdot \mathbf{M}_{\mathrm{s}}(\mathbf{r}') \right] \mathrm{d}\Xi. \tag{3.9}$$

This approach has the advantage that the modeling can be implemented more streamlined for numerical input data. Taking the antenna's discretized on-body near-field as a basis (same as with the standard free-space near-field to far-field transformation), the integral in (3.9) can be written as a sum:

$$\mathbf{E}(\mathbf{r}) = \sum_{(\xi,\nu)\in\Xi} \overline{\mathbf{G}}_{\mathrm{J}}^{\mathrm{E}}(\mathbf{r},\mathbf{r}'_{\xi\nu}) \Delta_{\xi\nu} \left(-\mathbf{n}_{\xi\nu} \times \mathbf{E}_{\xi\nu} \right) + \overline{\mathbf{G}}_{\mathrm{M}}^{\mathrm{E}}(\mathbf{r},\mathbf{r}'_{\xi\nu}) \Delta_{\xi\nu} \left(\mathbf{n}_{\xi\nu} \times \mathbf{H}_{\xi\nu} \right), \tag{3.10}$$

where the discrete surface currents $[J_{\mathrm{s}}] = \mathrm{A/m}$, respectively $[M_{\mathrm{s}}] = \mathrm{V/m}$, multiplied with the corresponding mesh cells surface area $[\Delta_{\xi\nu}] = \mathrm{m}^2$ correspond with the dipole moments $[p] = \mathrm{Am}$ and $[m] = \mathrm{Vm}$ in the derivation of the Sommerfeld problem solution [51].

3.1.3 Example Application

To prove the applicability of the approach, an example of a simplified hearing aid model (ref. Fig. 3.4) which is modeled consisting of ABS plastic (permittivity $\varepsilon_{\mathrm{r}} = 2.7$, loss tangent $\tan\delta = 0.005$) is evaluated. The antenna is designed as a conformal half-wave dipole on the hearing aid housing at $f = 2.45$ GHz. The near-field on the surface Ξ of the antenna, including the pinna as depicted in Fig. 3.4 , is utilized for the modeling. This way, the pinna is basically treated as part of the antenna. As can be seen from the results in Fig. 3.6(a), calculated above a flat phantom (equivalent to the infinite half-space of the analytical model), the new modeling approach is proven to be precise. The deviation of the E-field is less

than 1 dB in the far-field of the antenna compared to numerically calculated data. Secondly, the E-field captured on a realistic path along the body at a constant height of 10 mm above the phantom surface is evaluated. The results for the E-field on this surface and the evaluated path are depicted in Fig. 3.5. In Fig. 3.6(b) the fields along the path obtained from the numerical simulation are compared to the results calculated with the derived modeling approach. As can be seen, the model reveals a deviation of less than 3 dB from the numerical results along nearly the whole evaluated path.

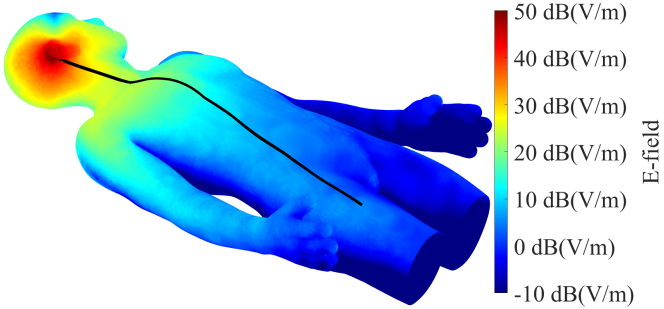

Figure 3.5: E-field distribution at a constant height of 10 mm above the phantom surface and the evaluated path [BM211].

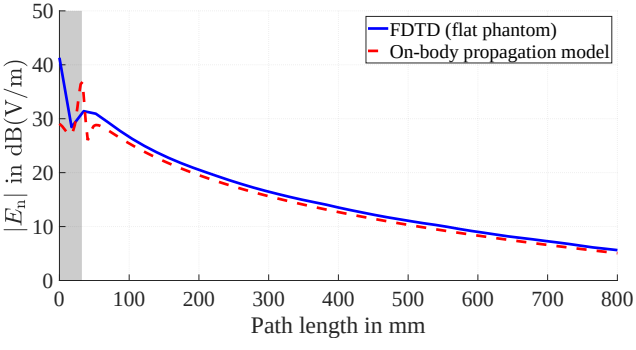

(a)

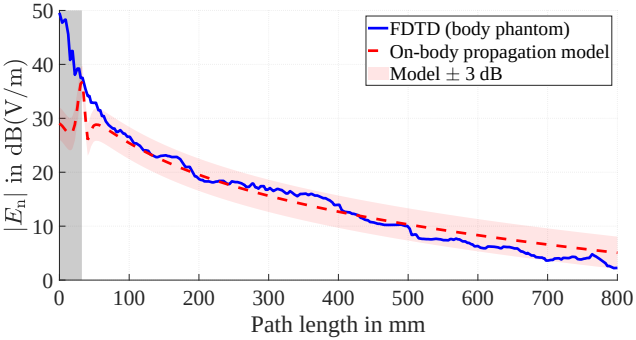

(b)

Figure 3.6: Verification of the implemented method by comparison of the calculated E-field to numerical results: (a) Ideal flat tissue half-space, (b) Realistic path along body phantom (ref. Fig. 3.5). The section inside surface Ξ is marked with a grey background. Only the normal component of the E-field with respect to the body surface is evaluated, as this is the dominating component (in the example by more than 10 dB) close to the tissue interface [BM211].

3.2 On-Body Far-Field

The previous section shows that the solutions for the Sommerfeld half-space problem enable modeling the on-body fields of wearable and implantable antennas. However, only a small part of the possible applications include sufficiently flat paths that can be directly modeled through the Sommerfeld problem. Besides that, it is desirable to evaluate an on-body antenna completely independent of the application scenario, i.e., de-embedded from the propagation channel. Therefore, this section defines the on-body far-field based on the half-space approximation, enabling the definition of adapted on-body antenna parameters.

As discussed in Chapter 2.1.1, for radiation in free-space, the far-field region is defined by considering that the radiated waves can locally be represented by a plane wave. In the free-space far-field, the power density decreases quadratically with increasing distance from the radiator for any antenna. Thus, the antenna gain defined as a relative indication of the radiation properties of the antenna compared with those of a reference is independent of the distance from the radiator. The case of an antenna above or inside a dissipative tissue is more complex due to the interference of the different wave components (direct, reflected, and Norton surface wave). Additionally, waves propagating along the boundary are attenuated by losses in the tissue. Thus, the standard antenna gain calculation for on-body antennas reveals a dependency on the distance (ref. Chapter 2.2.1). This inconsistency because of the additional attenuation due to losses in the tissue can be dealt with with an adapted normalization (replacement of the lossless isotropic source). Therefore, in the on-body far-field, this attenuation needs to be equal for all antennas to be considered. Additionally, amplitude and phase deviation across the wavefront near the tissue boundary must be negligible to recreate the local plane wave criteria.

By analyzing the structure of the on-body Green's functions, a boundary case for the definition of the on-body far-field can be found if surface-to-surface propagation is considered with $h = 0$ and $z = 0$. In this case, the angles in the solution of the half-space problem become:

$$\psi_0 = \psi_1 = 0^\circ. \tag{3.11}$$

Furthermore, the length of the two paths for direct and reflected waves are now equal:

$$R_0 = R_1 = \rho. \tag{3.12}$$

Hence the Green's functions can be simplified, e.g. in the Green's function $G^{\mathrm{E,z}}_{\mathrm{J},\perp}$ all cosine terms are replaced:

$$\begin{aligned} G^{\mathrm{E,z}}_{\mathrm{J},\perp} = &\underbrace{\cos^2(\psi_0)}_{1} \frac{e^{-\gamma_0\rho}}{\rho} + \Gamma_\perp \underbrace{\cos^2(\psi_1)}_{1} \frac{e^{-\gamma_0\rho}}{\rho} \\ &+(1-\Gamma_\perp)F(w) \underbrace{\cos^2(\psi_1)}_{1} \frac{e^{-\gamma_0 R_1}}{R_1}. \end{aligned} \tag{3.13}$$

Also, the specular reflection coefficient for perpendicular-polarized waves $\Gamma_\perp$ can be set to:

$$\Gamma_\perp = \frac{\sin(\psi_1) - \Delta_m}{\sin(\psi_1) + \Delta_m} \xrightarrow{\psi_1 = 0} \Gamma_\perp = -1 \tag{3.14}$$

Finally, for all Green's functions for the z- and ρ-polarization only the Norton surface wave term remains:

$$G(\rho) = K_{\mathrm{e}} F(\rho) \frac{e^{-\gamma_0\rho}}{\rho}. \tag{3.15}$$

where K_{e} is a constant representing the excitation strengths of the surface wave in the different Green's functions. This can be explained physically by the fact that with $h = 0$ and $z = 0$, the direct wave, and the reflected wave cancel each other

out. Additionally, the Sommerfeld attenuation factor $F(w)$ can be simplified for $h = z = 0$ by only depending on the radial distance ρ as [51]:

$$F(\rho) = 1 - j\sqrt{\pi K \rho} \cdot w_{\mathrm{F}}(-\sqrt{K\rho}), \tag{3.16}$$

with $w_{\mathrm{F}}(x)$ the Faddeeva function and $K = -0.5\gamma_0\Delta_{\mathrm{m}}^2$.

As noted, the form in (3.15) results only for the ρ- and z-polarization. However, comparing the magnitude of the different Green's functions near the tissue surface at ($z = \lambda/4$) as shown in Fig. 3.7, it becomes clear that the Green's functions for ρ- and ϕ-polarization are attenuated by more than 10 dB - 20 dB compared to the z-polarization. Thus, the on-body far field above the tissue surface ($z \geq 0$) can be approximated to be purely z-polarized. For wearable antennas ($h > 0$), the terms $G_{\mathrm{J},\perp}^{\mathrm{E,z}}$ and $G_{\mathrm{M},\parallel}^{\mathrm{E,z}}$ dominate, which correlates with the prior knowledge that antennas polarized normally to the body surface provide a higher on-body path gain [22], [24], [34], [44]. For implanted antennas ($h < 0$), besides $G_{\mathrm{M},\parallel}^{\mathrm{E,z}}$, the Green's function $G_{\mathrm{J},\parallel}^{\mathrm{E,z}}$ for currents aligned parallel to the boundary layer dom-

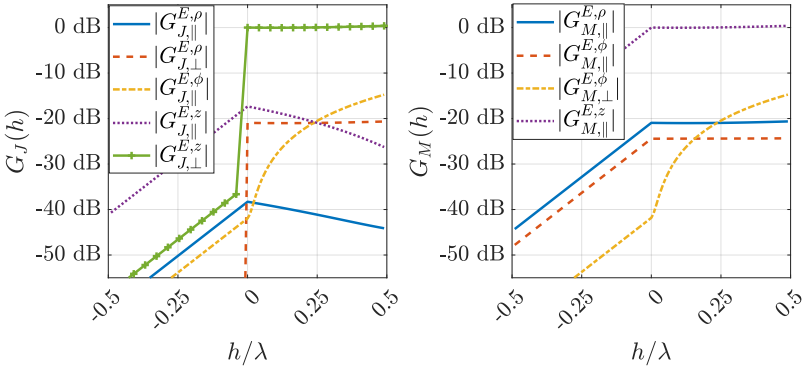

Figure 3.7: Normalized magnitude of the Green's functions at $\rho = 10\lambda$ and $z = \lambda/4$ as a function of the height h [BM211].

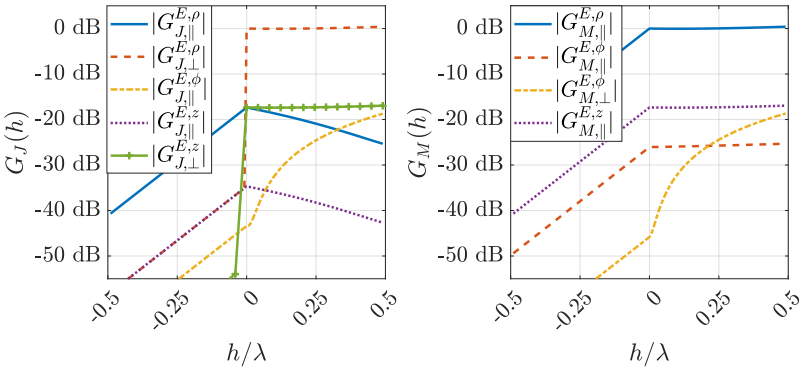

Figure 3.8: Normalized magnitude of the Green's functions at $\rho = 10\lambda$ and $z = -\lambda/4$ as a function of the height h.

inates due to the boundary condition for the normal E-field. If the same consideration is made for the Green's functions to calculate the fields within the tissue ($z < 0$) as shown in Fig. 3.8, the Green's functions for the same current elements dominate ($h \geq 0$: $J_\perp$ and $M_\parallel$, respectively, $h < 0$: $J_\parallel$ and $M_\parallel$). However, with $z < 0$, the E-field polarization of the dominating terms changed from z to ρ. This can be attributed to the fact that the z-polarized E-field (perpendicular component at the tissue surface) has a step of $\gamma_0^2\gamma_1^2$ at the interface, whereas the ρ-polarized E-field (tangential component at the tissue surface) is continuous.

Based on the observation made for the derived on-body Green's functions, a definition of the on-body far-field reference can be found as:

$$\mathbf{E}_{\mathrm{SW}} = \begin{cases} K_{\mathrm{e}} F(\rho) \frac{e^{-\gamma_0 \rho}}{\rho} \mathbf{e_z} & \text{if } z \geq 0, \\ K_{\mathrm{e}} F(\rho) \frac{e^{-\gamma_0 \rho}}{\rho} \frac{\gamma_0}{\gamma_1} e^{\gamma_1 z} \mathbf{e}_\rho & \text{if } z < 0. \end{cases} \tag{3.17}$$

Above the tissue for $z \geq 0$, this definition is very similar to the far-field reference in free-space, ref. (2.1). The difference here is that the defined plane wave, in ad-

dition to its ρ^{-1} dependence, is attenuated by the factor $F(\rho)$ corresponding to the on-body surface wave. From the tissue surface, the surface wave also propagates into the tissue ($z < 0$) whereas the field strength decreases with $e^{\gamma_1 z}$ due to the lossy tissue properties, as analyzed within the derivation of the on-body Green's functions, ref. Chapter 3.1.1. Furthermore, as can be seen in (3.17), the on-body far-field can be simplified to be purely z-polarized above the tissue and purely ρ-polarized inside the tissue. The factor $\gamma_0\gamma_1^{-1}$ can be found as a constant offset between all corresponding Green's functions for the ρ- and z-polarization[4].

3.3 On-Body Far-Field Region

The definition of the on-body far-field is based on the boundary case with both excitation and observer directly at the tissue surface ($h = z = 0$). Realistic antenna structures naturally have a non-zero height. Therefore, limits have to be defined for which the Norton surface wave can sufficiently approximate the Green's functions. Thus, the far-field region can be estimated within which the on-body far-field reference sufficiently approximates the radiated fields of an antenna, ref. (3.17). As evaluated before, at the tissue surface, the influence of the direct and reflected wave on the field distribution is eliminated by their mutual cancellation so that only the surface wave remains. This condition can be translated into two requirements. Firstly, the phase difference $\Delta\varphi$ between direct (R_0) and reflected wave (R_1) must be negligible:

$$\Delta\varphi = |\gamma_0| \, (R_0 - R_1) \approx 0. \tag{3.18}$$

[4] See appendix A for the individual Green's functions.

An estimation can be made by restricting the phase difference to $\Delta\varphi \leq \pi/8$.[5] With the approximation of parallel paths R_0 and R_1 this leads to a far-field distance of:

$$\rho \geq \rho_{\Delta\varphi} = \sqrt{\left(\frac{16hz\,|\gamma_0|}{\pi}\right)^2 - h^2}. \tag{3.19}$$

Secondly, the reflection coefficient $\Gamma_\perp$ needs to be negative such that direct and reflected waves interfere destructively. According to (3.14), the coefficient $\Gamma_\perp$ can be calculated from the angle ψ_1, which varies with the distance ρ, and Δ_m which is a constant complex number depending on the material parameters of the tissue. By analyzing its behavior as a function of the distance ρ, it can be found that:

$$\arg\{\Gamma_\perp\}(\rho \to 0) \approx 0, \qquad \arg\{\Gamma_\perp\}(\rho \to \infty) = \pi.$$

The distance where $\arg\{\Gamma_\perp\} \approx \pi/2$ can be determined by $\psi_1 = \mathrm{Re}\{\Delta_m\}$. This leads to a second restriction for the far-field distance:[6]

$$\rho \geq \rho_{\Delta\Gamma} = \frac{z+h}{|\Delta_m|^2\sqrt{\varepsilon_{r,1}}}\,. \tag{3.20}$$

Both conditions must be satisfied to ensure the field's approximation by the surface wave term only, thus fulfilling the on-body far-field criteria. As can be seen, both depend on the transmitter's height h and the receiver's height z. The distance of the highest point above the tissue surface needs to be used for extended antenna structures. In Fig. 3.9 the dominating Green's functions $G^{\mathrm{E},\perp}_{\mathrm{J,z}}$ and $G^{\mathrm{E},\parallel}_{\mathrm{M,z}}$ are depicted exemplary, calculated at a height of $z = h = \lambda/2$. Here, the far-field distance according to (3.20) gives a value of $\rho \geq 7.5\lambda$. As required, at this range, the trajectories of both Green's functions have sufficiently converged into the surface wave attenuation term $F(\rho)$.

[5] Same limit was chosen for the definition of the widely accepted Fraunhofer far-field distance
[6] See Appendix B for the complete derivation

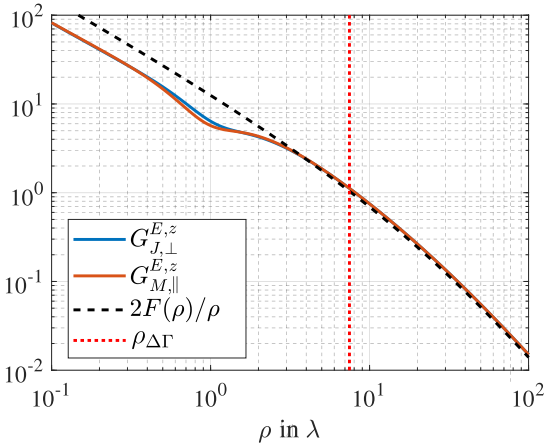

Figure 3.9: Dominant Green's functions for $z = h = \lambda/2$ compared to surface wave attenuation factor $F(\rho)$ and corresponding far-field distance (3.20) [BM211].

Using the two above determined conditions, it is ensured that the distance-dependent attenuation along the tissue is sufficiently modeled by the on-body far-field approximation from equation (3.15). In addition, for heights ($z > 0$), it must be noted that the surface wave term F is also height-dependent. Analytically, this height-dependency of the surface wave in the air can be approximated under the assumptions $\gamma_0\rho \gg 1$ and $\rho^2 \gg h^2; z^2$ through an additional factor $H(h,z)$ [53]:

$$F(\rho,h,z) = F(\rho) \cdot H(h,z), \tag{3.21}$$

$$H(h,z) = (1 + h\gamma_0^2/\gamma_1)(1 + z\gamma_0^2/\gamma_1), \tag{3.22}$$

with $w_{\mathrm{F}}(x)$ the Faddeeva function and $K = -0.5\gamma_0\Delta_{\mathrm{m}}^2$. Considering a constant source height h and limiting the amplitude variation to:

$$|H(h,z_{\max})/H(h,z=0)| = 1 + \delta \tag{3.23}$$

the maximum z-value can be found as ($\alpha_1 = \mathrm{Re}\{\gamma_1\}$):

$$z \leq z_{\Delta F} = \frac{\alpha_1 + \sqrt{\alpha_1^2 + (\delta^2 + 2\delta)\,|\gamma_1|^2}}{|\Delta|^2 |\gamma_1|^2}. \tag{3.24}$$

Compared to (3.20) and (3.19), Equation (3.24) gives a constant value which only depends on the dielectric parameters of the tissue.

In the formulas up to this point, only the extended height of the antenna above the tissue surface is considered for the extension of the far-field region. Additionally, the far-field distance accounting for an extended width D of the antenna structure parallel to the tissue boundary layer can be calculated. Since the phase term of the surface wave corresponds to that of the free space the common Fraunhofer far-field approximation can be used [2]:

$$\rho \geq \rho_D = \frac{2D^2}{\lambda}. \tag{3.25}$$

The combination of all four far-field conditions, (3.19), (3.20), (3.24), and (3.25) defines the limit for the on-body far-field region sought.

In Fig. 3.10, the derived on-body far-field and its limits can be analyzed equivalently to the consideration in free-space (ref. Chapter 2.1.1). In Fig. 3.10(a), the numerically calculated E-field of Hertzian dipole at the tissue interface is depicted in the ρz-plane. Below in Fig. 3.10(b), the on-body far-field reference field as defined in (3.17) is depicted. The difference between these can be analyzed for the amplitude in Fig. 3.10(c) and for the phase in Fig. 3.10(d). As can be seen in Fig. 3.10(c), the constant term $z_{\Delta F}$ is needed mainly for limiting the z-dependent amplitude deviation for the on-body far-field as expected from the derivation. For the graphical representation (3.20) and (3.19) can also be rearranged for z. Since the height h of the radiating current element for the depicted fields is very small, the limit $z_{\Delta\varphi}$ calculated using (3.19) for limiting the phase difference between

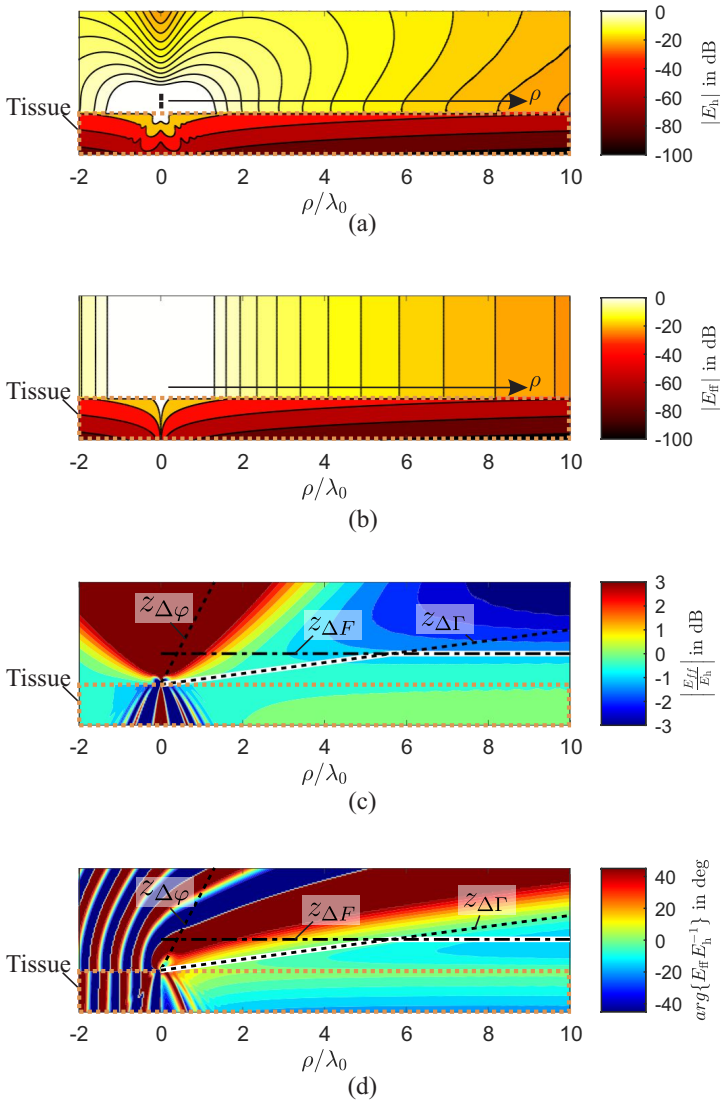

Figure 3.10: On-body far-field region; (a) E-field of a point source (Hertzian dipole) at the tissue interface; (b) E-field of on-body far-field reference (3.17); (c) Amplitude deviation between fields of point source and far-field reference; (d) Phase deviation between fields of point source and far-field reference.

direct and reflected wave covers a very large angular range in the chosen example. Therefore, $z_{\Delta\Gamma}$ calculated from (3.20) is the limiting factor for distance $\rho < 6\lambda_0$ in the example as depicted. As shown in Fig. 3.10(d), this limit also ensures a sufficiently plane wave concerning the phase. Thus, the combination of all limits, depicted by the white graph in Fig. 3.10(c) and (d), defines the far-field region as required. Inside the tissue no further restrictions have to be made since due to the high losses all other wave components rapidly decay besides the surface wave, which continuously radiates into the tissue while traveling along the interface.

3.4 Influence of the Body's Curvature

Up to this point, on-body propagation was modeled purely with the approximation of the body as an infinitely extended half-space. However, in real applications, curvatures also play an essential role. Fortunately, both problems are closely related as shown by Wait in [45]. For the half-space problem with pure surface wave propagation ($h = z = 0$), which, as shown, is also a valid approximation in the on-body far-field, Wait rewrites the solution for the normally polarized E-field as:

$$E^{\perp} = E_0 F(\rho), \tag{3.26}$$

where $F(\rho)$ is the aforementioned Sommerfeld attenuation factor. The term E_0 is denoted as a reference field. This term can also be found in Wait's notation for the creeping wave propagation around a cylindrical curvature [45]:

$$E^{\perp} = E_0 W(x,q). \tag{3.27}$$

Here, $W(x,q)$ represents the attenuation function for the creeping wave problem, which depends on the x as a normalized range parameter and q accounting for the curvature's radius. Thus, the excitation properties, i.e., the antenna, are quan-

tified with E_0 in both cases. After normalization by the attenuation term $F(\rho)$, as derived in the following, applying the on-body antenna parameters calculated in the case of a flat tissue half-space is equally possible for propagation channels with curved surfaces.

This work does not provide a more detailed consideration of these properties or the extension of the far-field definition to curved surfaces. Due to the additional parameter of the radius of curvature, which is also not constant in practical applications, it can be assumed that the definition will be considerably more complex so that its practical applicability can be doubted. Furthermore, it will be shown in the following employing practical examples that already with the investigations made so far for the tissue half-space, according to the close relation to the curved surface, meaningful antenna characterization possibilities can be developed. For modeling more complex problems in Chapter 5 an alternative method is proposed.

Chapter 4

On-Body Antenna Parameters

The on-body far-field defined in the previous chapter allows for the characterization of wearable or implanted antennas independent of the application, just as it is done by default for antennas radiating in free-space, ref. Chapter 2.1.2. The derivation of the on-body antenna parameters in the following is based as far as possible on the known definitions for free-space in order to ensure good comprehensibility.

First, a complete redefinition of the standard antenna parameters according to the *IEEE Standard for Definitions of Terms for Antennas* [11] is carried out for the on-body domain. For the numerical evaluation of the defined parameters an adapted near-field to far-field transformation is defined. Secondly, the Friis transmission equation is redefined for the on-body domain. Example applications are then used to validate the definitions. For the practical applicability of the methods, a test procedure for measuring the defined on-body antenna parameters is defined. Furthermore, a corresponding test range is designed and validated using another example application.[7]

[7] This chapter is based on the following publications: [BM211, BM212, BM213, BM214] (©2021 IEEE).

4.1 Definition

Based on the defined on-body far-field, an on-body radiation pattern can be defined. To quantify an antenna's ability of exciting waves traveling along the body surface, a two-dimensional angle-dependent measure for the radiation parallel to the body surface is sufficient. Thus, based on the definition in free-space (FS), ref. Chapter 2.2, the antenna's directivity can be adapted for on-body (B) propagation to:

$$D_{\mathrm{FS}}(\theta,\phi) = \frac{U(\theta,\phi)}{\overline{U}} \;\rightarrow\; D_{\mathrm{B}}(\phi) = \frac{U^{\perp}(\phi)}{\overline{U^{\perp}}}. \tag{4.1}$$

Here $U^{\perp}(\phi)$ is the radiation intensity corresponding to the normal polarization (with respect to the tissue) only, since it dominates close to the tissue boundary in the far-field, ref. Chapter 3.2. Because in the on-body far-field the amplitude ratio of the associated Green's functions for $E^{\perp}$ and $H^{\parallel}$ also is $\eta_0 = \mu_0\varepsilon_0$, the radiation intensity can be calculated as:

$$U^{\perp}(\phi) = \rho^2 \frac{1}{2} E^{\perp}(\phi) H^{\parallel}(\phi) = \frac{\rho^2 {E^{\perp}}^2(\phi)}{2\eta_0}. \tag{4.2}$$

To quantify the surface wave radiation solely, the mean intensity $\overline{U^{\perp}}$ for the directivity is only determined over ϕ in the plane parallel to the body surface as:

$$\overline{U^{\perp}} = \frac{1}{2\pi} \oint_{2\pi} U^{\perp}(\phi) \mathrm{d}\phi. \tag{4.3}$$

Other than in free-space, the radiation intensity $U^{\perp}$ is dependent on the distance because of the additional attenuation of the surface wave traveling along the tissue boundary. For the on-body far-field, this surface wave attenuation can be quantified by $2|F(\rho)|$ for the dominant Green's functions as shown in Chapter 3.2.

Thus, following the derivation in free-space, the on-body antenna gain can be defined as:

$$G_{\mathrm{FS}}(\theta,\phi) = \frac{U(\theta,\phi)}{P_{\mathrm{in}}/4\pi} \rightarrow G_{\mathrm{B}}(\phi) = \frac{U^{\perp}(\phi)}{P_{\mathrm{in}}|F(\rho)|^2/\pi}. \tag{4.4}$$

with P_{in} the power accepted at the antenna port. Through normalizing the surface wave attenuation, the defined on-body gain is independent of the measurement distance. To illustrate this, in Fig. 4.1(a) the standard free-space gain G_{FS} is depicted for the example of a short dipole antenna above a tissue half-space again, ref. Chapter 2.1.1. As can be seen there is a significant variation in the gain if calculated at different distances ρ. In contrast, the defined on-body gain G_{B}, as depicted in Fig. 4.1(b), is constant, independent of the measurement distance ρ.

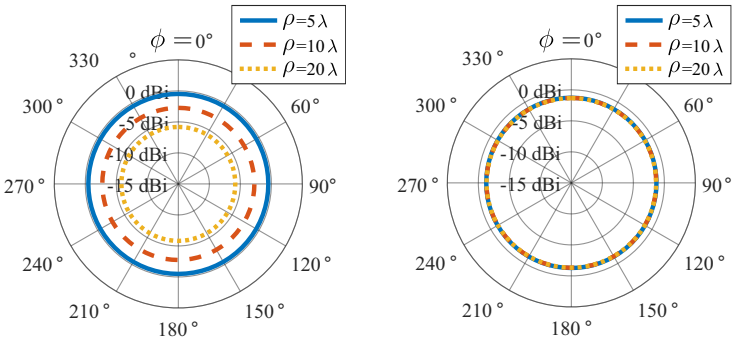

Figure 4.1: Antenna gain of short dipole antenna orientated normally at at height of $h = \lambda/4$ above an infinite half-space of muscle tissue calculated at different distances R: (a) Standard free-space gain G_{FS}; (b) On-body gain G_{B}.

The constant ratio between on-body gain and directivity also gives an adapted definition of the antenna radiation efficiency:

$$e_{\mathrm{B}} = \frac{G_{\mathrm{B}}}{D_{\mathrm{B}}} = \frac{\pi \overline{U^{\perp}}}{|F(\rho)|^2 P_{\mathrm{in}}}. \tag{4.5}$$

This measure approximates the ratio between the power accepted at the port and the power radiated in form of the surface wave. The normalization based on the surface wave attenuation factor $F(\rho)$ is only valid for antenna structures close to the tissue surface. Efficiency values greater than one can therefore also be calculated for higher heights. In Fig. 4.2 the on-body antenna radiation efficiency e_{B} is depicted in comparison to the standard antenna radiation efficiency e_{FS} for three short dipole antennas in dependency of the height h above the tissue surface. As can be seen, for the electric dipole orientated perpendicular to the tissue surface ($J_{\perp}$), and the magnetic dipole parallel to the tissue ($M_{\parallel}$), both measures have a comparable trend with increasing efficiency for increasing height h. However,

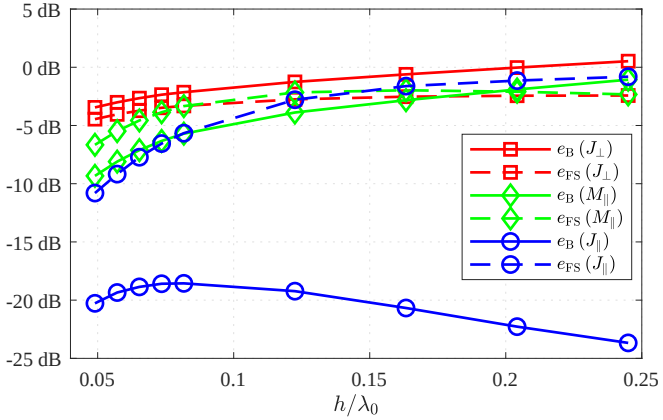

Figure 4.2: On-body efficiency e_{B} compared to standard antenna radiation efficiency e_{FS} for short dipole antennas in dependency of the height h above the tissue surface.

with the electric dipole parallel to the tissue ($J_{\parallel}$) the results differ significantly. As before, the free-space efficiency $e_{\mathrm{FS}}\left(J_{\parallel}\right)$ increases with increasing height h. In contrast, the on-body efficiency $e_{\mathrm{B}}\left(J_{\parallel}\right)$ is much smaller in magnitude, has a maximum at $h \approx 0.075\lambda_0$, and decreases thereafter with increasing height h. Physically interpreted, both efficiencies take equal account of near-field dielectric losses through the tissue. However, the free-space efficiency mainly is influenced by the field components radiated off the body, whereas the on-body antenna efficiency quantifies the excitation of the surface wave along the body. Thus, the on-body efficiency is an important relative indicator for on-body antennas, especially since the free-space radiation efficiency for on-body propagation gives partly contradictory results.

The relation between the on-body gain and the effective area (aperture) can be calculated by the same procedure as in free-space to[8]:

$$A_{\mathrm{e,B}} = \frac{\lambda^2}{4\pi} G_{\mathrm{B}}. \tag{4.6}$$

Finally, the transmission equation for on-body propagation can be reassembled to:

$$\frac{P_{\mathrm{r}}}{P_{\mathrm{t}}} = G_{\mathrm{B,t}} \underbrace{\left(\frac{\lambda \kappa_{\mathrm{SW}}}{4\pi\rho}\right)^2}_{L_{\mathrm{B}}^{-1}} G_{\mathrm{B,r}}. \tag{4.7}$$

In comparison to the original form of the equation (2.9), all three quantities, the antenna gains G_{B} of transmit and receive antenna as well as the path-loss factor L_{B} were newly defined for the on-body domain. Here κ_{SW} describes the surface wave attenuation, which depends on the body curvature along the path evaluated. For sufficiently flat sections of the path, it can be calculated as $\kappa_{\mathrm{SW}} = 2F(\rho)$, and for curved path sections the term can be determined by $\kappa_{\mathrm{SW}} = 2W(x,q)$ (ref. Chapter 3.4).

[8] The proof based on a Hertzian dipole can be found in Appendix C.

4.2 Implementation and Evaluation of Example Applications

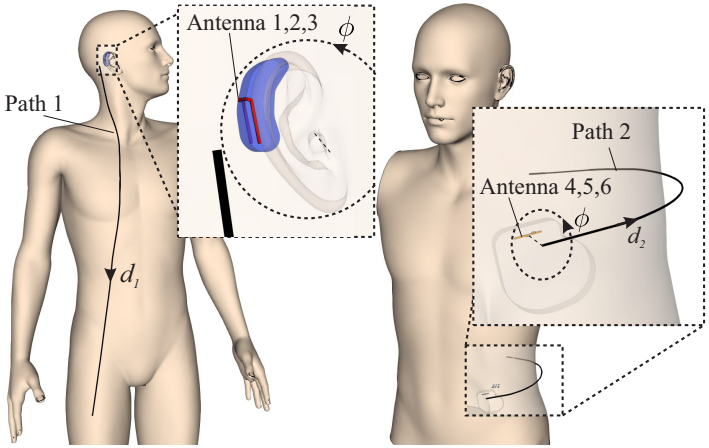

Figure 4.3: Evaluated example applications of a hearing aid antenna and a pacemaker [BM211].

For evaluating the defined parameters, two example applications are considered, one for a wearable and one for an implantable antenna. Simple dipole antennas are used since the focus is not on the antenna design but on the verification of the developed methods. Two different paths are evaluated, as can be seen in Fig. 4.3. Path 1 along the torso is chosen to be relatively flat. In contrast, path 2 around the torso contains curved sections and has no line-of-sight. For the implementation and verification both examples are modeled numerically using the FDTD-solver of Empire XPU [54].

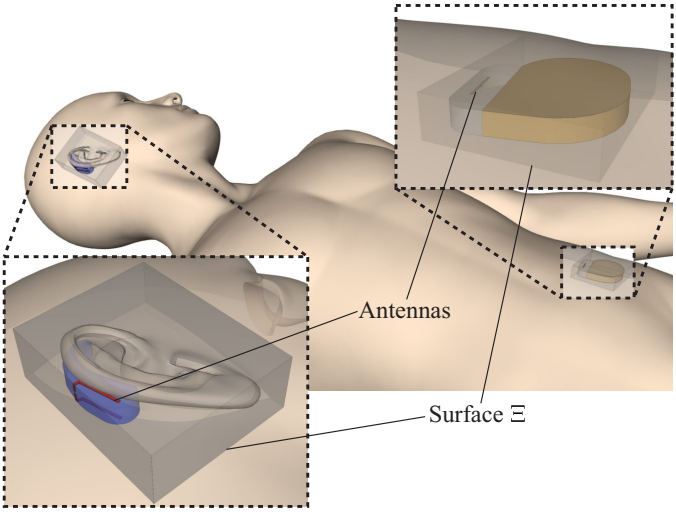

Figure 4.4: Enclosing surfaces Ξ of the near-field box for the scenarios: hearing aid antenna (left) and pacemaker (right) [BM211].

The implementation of the described methods for calculating the defined on-body antenna parameters can be divided into the following three steps:

1. **Calculation of the antenna's near-field**
   First the antenna's near-field on an enclosing surface Ξ in presence of the body phantom is calculated numerically. This is illustrated for the evaluated examples in Fig. 4.4. As can be seen, for the example of the hearing aid antenna, the pinna is also enclosed by Ξ and thus treated as part of the antenna. Furthermore, the surface Ξ intersects with tissue surface, which is taken account by considering negative values for the heights h (ref. Chapter 3.1.1) for these parts of Ξ in the following step 2. The same applies to the surface Ξ lying completely within the tissue for the implant application, ref. Fig. 4.4 (right).

For calculating the antenna's near-field often a large part of the body phantom can be excluded from the simulation model since the influence of distant parts on the near-field can be neglected. Thus, simulation times are accelerated, as e.g. for the hearing aid application only one half of the phantom's head must be included in the calculation.

2. **On-body near-field to far-field transformation**
   The on-body far-field of the analyzed antenna structure is calculated from the numerically calculated near-field (step 1) and the on-body Green's functions in Appendix A. Thereby, using surface equivalence (ref. Chapter 3.1.2) the angle-dependent radiated E-field above the tissue surface is calculated using (3.10). Using the prior knowledge from the definition of the on-body far-field, only the dominant component perpendicular to the tissue surface $E_{\perp}$ has to be determined. In addition to the relative distances between the points on Ξ and the observation point in the far-field, the absolute heights h of the points on Ξ above or below the tissue surface are included in the calculation. A sufficient calculation distance ρ for fulfilling the on-body far-field limits is calculated using the equations in Chapter 3.2. Furthermore the dielectric properties of the tissue tissue along which the waves propagate are considered in the calculation of the on-body far-fields.

3. **Calculation of the on-body antenna parameters**
   Finally, the on-body antenna parameters as described in Chapter 4.1 are calculated from the radiated E-field. The same dielectric properties of the tissue as in step 2 and the same calculation distance ρ have to be considered for calculating the surface wave attenuation factor $F(\rho)$ to ensure a correct normalization of on-body gain and efficiency.

4.2.1 Radiation of a Wearable Antenna along a Flat Path

As an example of a wearable antenna, a simplified hearing aid model as shown in Fig. 4.3 is considered. The antenna is designed as a conformal half-wave dipole on the hearing aid housing, which is modeled consisting of ABS plastic (permittivity $\varepsilon_\mathrm{r} = 2.7$, loss tangent $\tan\delta = 0.005$) at $f = 2.45$ GHz. To compare the effects of different antenna patterns along path 1 (ref. Fig. 4.3), the antenna is positioned on the housing in three different configurations (antenna 1-3), as can be seen in Fig. 4.5. The calculated on-body antenna gain for all three antenna configurations is depicted in Fig. 4.6. The minimum on-body far-field distance is calculated by (3.20) to $\rho_\mathrm{min} \approx 200$ mm for the maximum antenna height of $h = 17$ mm and the receiver height of $z = 10$ mm.

In the next step, the radiated fields of all three hearing aid antenna configurations along path 1 are evaluated to characterize e.g. the wireless link of a hearing aid to a smartphone. In Fig. 4.7(a) the path gain (PG) of the antennas calculated with the adapted Friis transmission equation (4.7) is compared to FDTD calculated data of the actual geometry as reference. Here, a receiver gain of $G_\mathrm{B,r} = 0$ dB is assumed. The propagation loss factor L_B is calculated assuming a flat body surface. As can be seen, the overall trend in the path gain is sufficiently modeled, even though locally noticeable deviations occur due to geometric irregularities compared to the ideally simplified flat body surface.

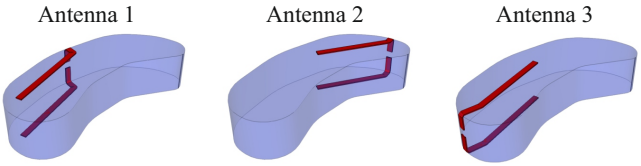

Figure 4.5: Conformal dipole on hearing aid housing in three different configurations [BM211].

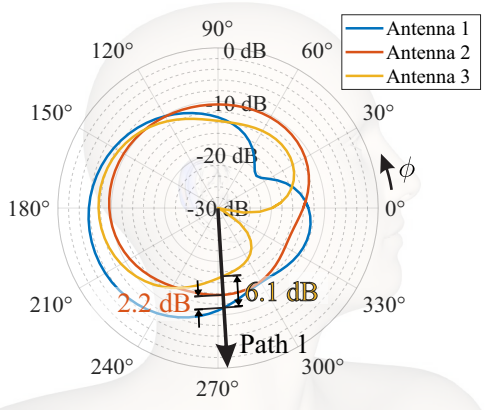

Figure 4.6: On-body gain of the three different hearing aid antenna configuration as depicted in Fig. 4.5. The on-body gain is calculated including the influence of the pinna [BM211].

Furthermore, the path gain for all three antennas deviates with the same pattern from the analytical model and the difference between the different antennas seems constant. In order to assess this better, in Fig. 4.7(b) the path gain is normalized to that of antenna 1. Here it can be seen that the difference in the established on-body gain in the path direction (ref. Fig. 4.6) precisely predicts the difference between the different antennas considered. Beyond the minimum far-field distance $\rho_{\min}$, the relative path gain predicted from the on-body gain deviates by less than 1 dB from the numerically calculated reference.

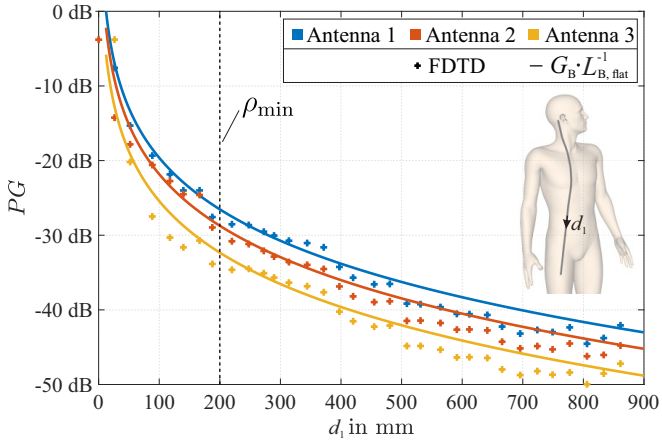

(a)

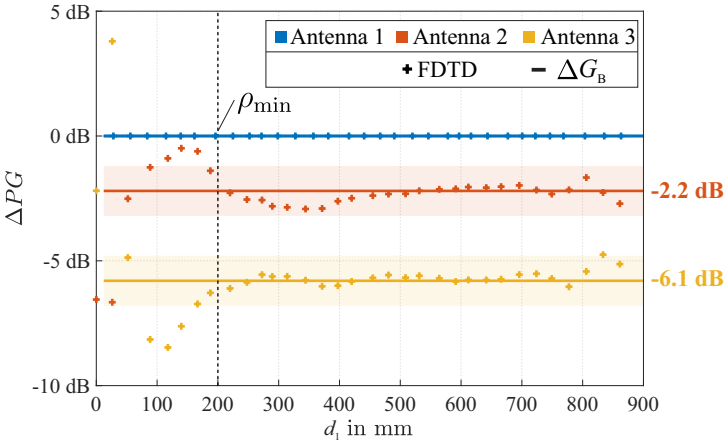

(b)

Figure 4.7: Antennas 1-3: (a) on-body path gain at a height of 10 mm above the tissue surface; (c) path gain difference with antenna 1 as reference. Shaded areas mark the deviation limited to ±1 dB [BM211].

4.2.2 Radiation of an Implantable Antenna along a Curved Path

As an example of an implantable antenna, the application of a pacemaker is evaluated, which is depicted in Fig 4.3. Therefore, the on-body propagation along path 2 around the torso which has a significant curvature is investigated. The antenna consists of a half-wave dipole encapsulated by a 1.3 mm thick substrate ($\varepsilon_r = 10.2$) implanted in a depth of 10 mm. For simplicity, no additional peripherals of the implant are modeled in the simulation. The minimum on-body far-field distance according to (3.20) in this case is $\rho_{min} \approx 75$ mm. To compare the propagation for different gain values, the antenna is rotated in the three different angles ($\Delta\phi = 30°$) in the plane parallel to the tissue surface. Consequently, as depicted in Fig. 4.8, the radiation pattern quantified in form of the on-body gain varies in direction of the evaluated path 2 by $\Delta G_{B,5} = 3.3$ dB

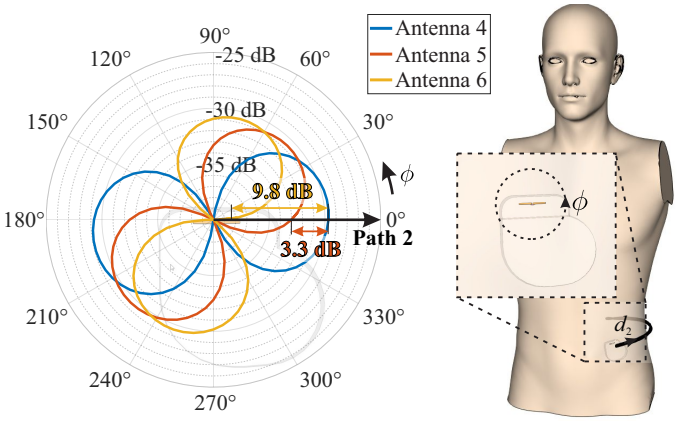

Figure 4.8: On-body gain G_B for the evaluated pacemaker antenna. Three different rotation angles are considered [BM211].

for antenna 5 and $\Delta G_{\mathrm{B},6} = 9.8\,\mathrm{dB}$ for antenna 6, provided that antenna 4 is used as reference. Looking at the path gain along path 2 in Fig. 4.9(a), one can see that it partially declines more rapidly than for the flat case because of the body curvature. A better estimate using the adapted on-body Friis equation (4.7) can be made by calculating the propagation loss factor L_{B} from the first creeping wave mode assuming a cylindrical curvature with a radius of 140 mm, as proposed in [28]. The deviation of the simplified model from the numerical data of the realistic geometry is still significantly higher compared to approximately flat path with the hearing aid application. However, all three antennas still show the same pattern in the path gain. Thus, by comparing the relative path gain with antenna 4 as reference as depicted in Fig. 4.9(b), again the difference in the on-body gain precisely predicts the path gain difference of the antennas in the numerically calculated realistic model. On closer evaluation, in the numerically calculated data, the influence of multi-path propagation becomes apparent (especially for antenna 6 which has the lowest gain along the direct path) which is not accounted for in the utilized analytical model.

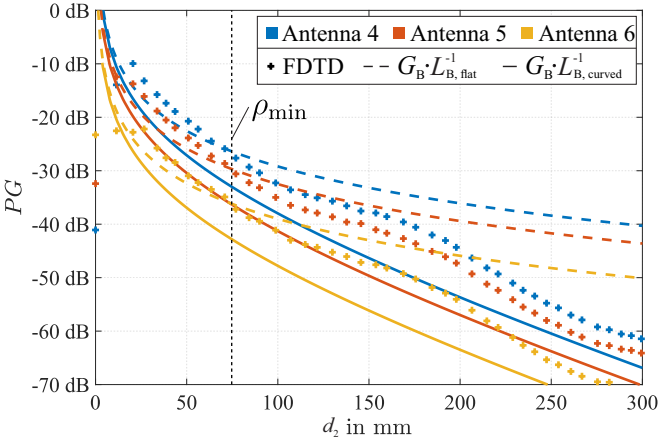

(a)

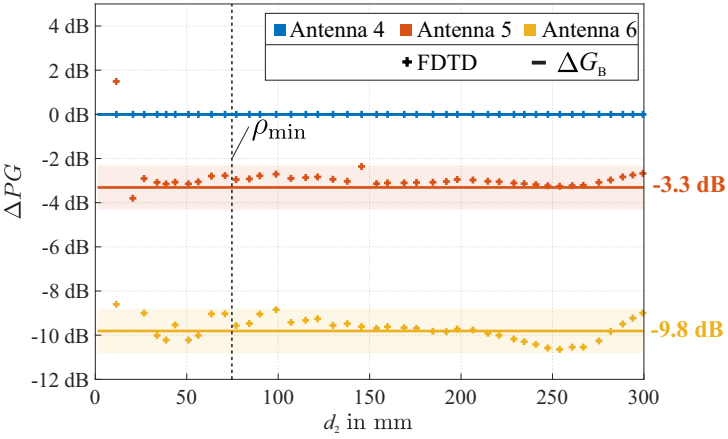

(b)

Figure 4.9: Antennas 4-6: (a) on-body path gain at a height of 10 mm above the tissue surface; (b) path gain difference with antenna 4 as reference. Shaded areas mark the deviation limited to ±1 dB [BM211].

4.3 On-Body Gain Measurement

Having defined adapted antenna parameters for on-body propagation, methods for their measurement can also be developed. For the standard free-space antenna parameters, the gain-transfer method, ref. Chapter 2.1.5, is the most commonly employed method for antenna gain measurements [6]. Through the newly defined on-body transmission equation (4.7), this method can also be adapted for measuring the on-body gain of an antenna under test (AUT). Fig. 4.10 outlines a corresponding test procedure. The transmission coefficient between a feed antenna and the AUT separated by the measurement distance R is measured at a tissue half-space in dependency of the AUT rotation angle ϕ. The unknown on-body antenna gain $G_{\mathrm{B,AUT}}$ of the AUT can be calculated from the difference of the transmission coefficient S_{21} compared to a measurement with a known calibration antenna $G_{\mathrm{B,cal}}$ (all parameters in log-scale / dB) as:

$$G_{\mathrm{B,AUT}} = |S_{21,\mathrm{AUT}}| - |S_{21,\mathrm{cal}}| + G_{\mathrm{B,cal}}. \tag{4.8}$$

For both measurements (calibration and AUT), the distance R to the feed antenna is kept constant. Thus, the necessary normalization of the distance-dependent surface wave attenuation factor $F(\rho)$, ref. (4.4), is achieved inherently.

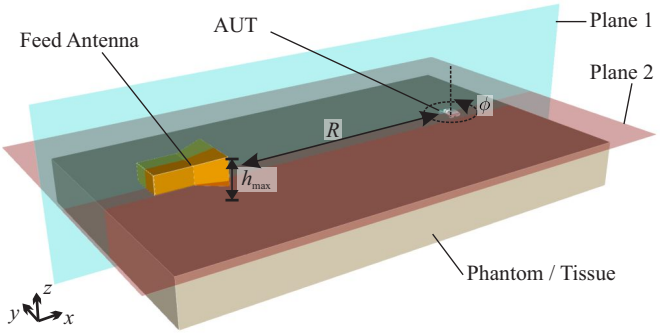

Figure 4.10: Measurement principle with planes of analyzed fields [BM212].

4.3.1 Antenna Test Range Design

Standard test ranges are designed such as the uniformity of the illuminating field over a given region within the range meets certain specifications. This region is usually referred to as the quiet zone (QZ) and is the region in which the AUT is to be placed [6]. For free-space measurements, the reference is usually a plane wave according to the far-field definition. Thus, the QZ is specified by the approximation to a plane wave. In Chapter 3, an adapted on-body far-field was defined, which subsequently is utilized as the reference for evaluating the QZ of the designed on-body antenna test range. Likewise, the limits for the on-body far-field region derived in Chapter 3 can be used directly to estimate the extent of the QZ of the designed antenna test range.

As illuminating feed antenna, a standard horn antenna (Seavey SGA-30 L, free-space gain $G = 8.1$ dBi at $f = 2.45$ GHz), ref. Fig 4.10, is used. It is placed at a center height of $h = 40$ mm above the tissue with normal polarization towards the tissue surface. Thereby, the highest point of the aperture is at $h_{\text{max}} = 70$ mm. Fig. 4.11(a) depicts the FDTD-calculated amplitude of the electric field radiated by the horn antenna above homogeneous muscle tissue ($\varepsilon_r = 52.7$, $\sigma = 1.74$ S/m). As can be seen, the fields in plane 1 (perpendicular to the tissue surface, ref. Fig. 4.10) differ from the on-body far-field reference E_{SW}[9], depicted in Fig. 4.11(b). The amplitude of the excited fields is also dependent on the height above the tissue boundary. With the dielectric parameters of the assumed muscle tissue at $f = 2.45$ GHz, the maximum height is calculated using (3.24) as $z_{\text{QZ,max}} = 92$ mm for limiting the amplitude deviation to 1 dB. Fig. 4.11(c) depicts the amplitude deviation between the excited fields as depicted in Fig. 4.11(a) and the surface wave reference as depicted in Fig. 4.11(b). It can be seen, that the estimation of the maximum height is sufficient for distances above approximately $R \geq 0.5$ m.

[9] For the definition of the on-body far-field reference E_{SW} see (3.17) in Chapter 3.

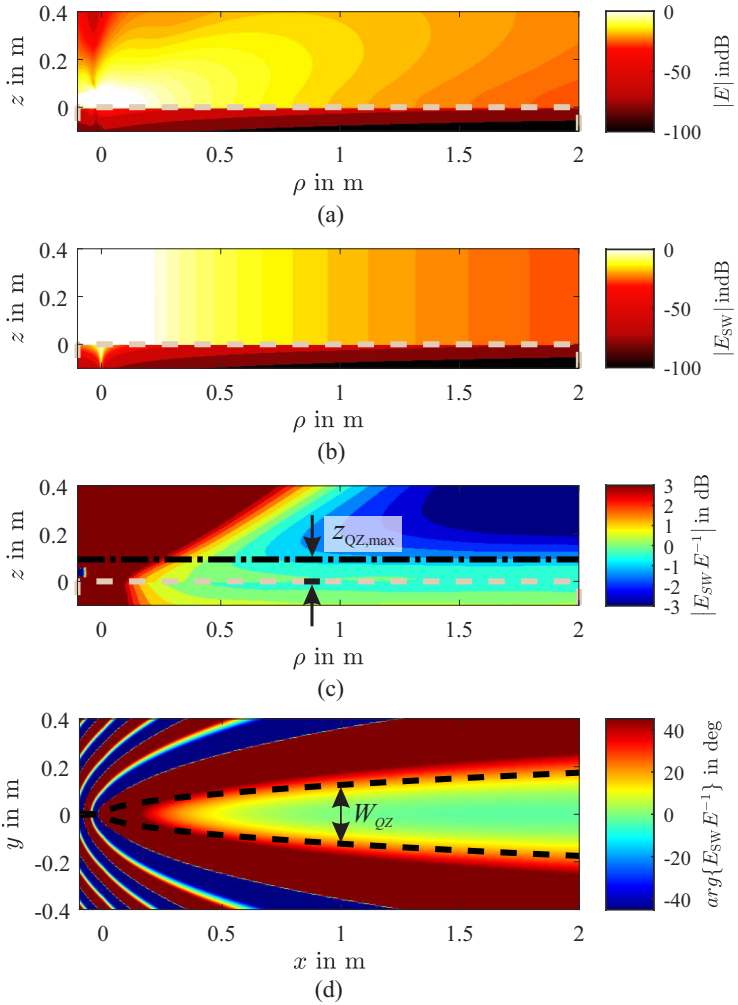

Figure 4.11: (a) Radiated E-field amplitude in plane 1; (b) On-body far-field reference amplitude E_{SW}; (c) Amplitude deviation, i.e. QZ. Dashed-dotted line: maximum height z_{max}; (d) Phase deviation in plane 2. Dashed line highlights maximum QZ width W_{QZ} [BM212].

For minimizing the necessary far-field distance according to (3.19) and (3.20), the highest point of possible antennas under test (AUTs) is further limited to $z_{\max} = 50\,\text{mm}$, which results in a measurement distance of $R \approx 1000\,\text{mm}$. In plane 2 (ref. Fig. 4.10), parallel to the tissue surface, the QZ for the on-body antenna test range is mainly limited by phase variations. Therefore, equivalently to free-space, the Fraunhofer far-field approximation (3.25) can be used to estimate the width of the QZ, as can be seen in Fig. 4.11(d). By rearranging (3.25) for the AUT diameter D and setting $\rho = R$, a maximum QZ width of $W_{\text{QZ,max}} = 247\,\text{mm}$ (maximum phase deviation of 22.5°) is obtained.

As described before, the defined on-body gain, ref. (4.4), needs to be measured above an infinite tissue half-space. However, a corresponding flat body phantom, ref. Fig. 4.10, can only be realized with finite size which should be kept to a minimum due to the cost and handling of the tissue-simulating material. Size and shape of the flat phantom for the designed measurement setup are therefore optimized by numerical simulations, starting with a rectangular shape, as illustrated exemplary in Fig. 4.12(a). Here, the flat phantom has a width of $W = 0.7\,\text{m}$ and the far end at $x = 1.4\,\text{m}$ is terminated with an absorbing boundary. As can be seen, a spatial interference pattern arises through reflections at the phantom edges. A solution for this in form of a tapered shape of the phantom can be adapted from the free-space case with tapered anechoic chambers [6], [55]. The taper angle of the flat phantom of $\alpha = 23.5°$ has been optimized numerically. As illustrated in Fig. 4.12, the spatial interference pattern varies less and the test zone is illuminated smoothly because of the reduced phase difference between direct propagating waves and the reflected wave at the phantom edge. At the same time, this solution significantly reduces the volume of necessary tissue-simulating material.

To enable automatic pattern measurements, the AUT needs to be rotated around the axes perpendicular to the tissue surface. To prevent the mechanical parts from coming in contact with the tissue-simulating liquid, a positioner is designed that

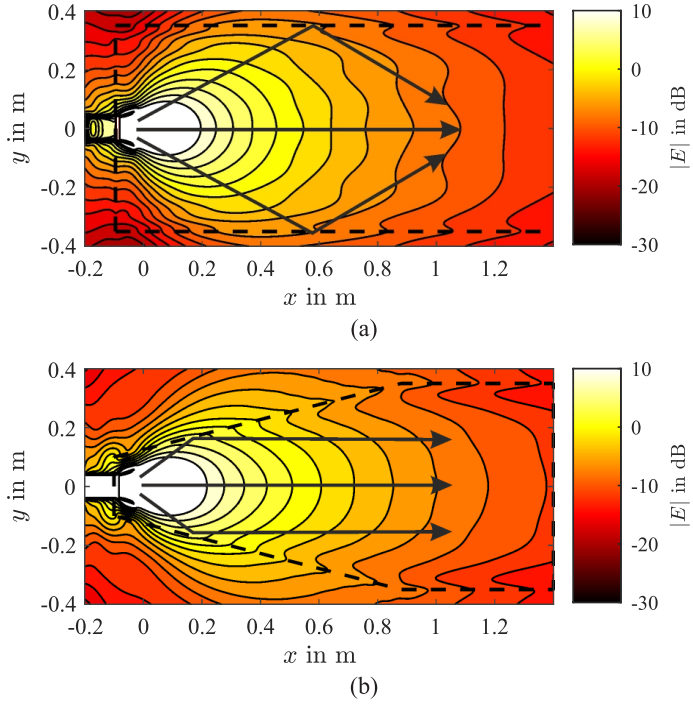

Figure 4.12: FDTD-simulated E-field in plane 2 (ref. Fig 4.10) at $z = 20\,\text{mm}$, (a) rectangular body phantom, (b) tapered body phantom [BM212].

is supported from above. However, with this setup the AUT fixture is in the line of sight between both antennas. Therefore, the fixture is optimized to be as electromagnetically transparent as possible. As a solution, a cylindrical cage is designed in the form of an iso-truss structure [56], ref. Fig. 4.13. It is manufactured by 3D printing of polylactic acid (PLA) plastic ($\varepsilon_r \approx 3$) and consists of rods with a diameter of $d = 5\,\text{mm}$. The results of numerical simulations as depicted in Fig. 4.14 show that the radar cross-section (RCS) of the designed iso-truss structure is only 12% of that of a cylinder with $t = 2\,\text{mm}$ wall thickness and the same diameter, height and material. Thus, the designed AUT positioner ensures very low reflectivity while maintaining mechanical stability.

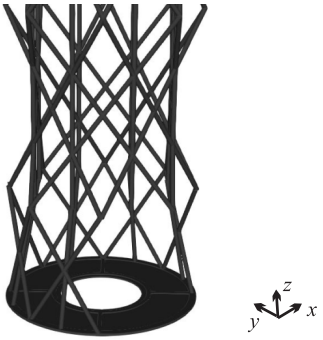

Figure 4.13: Designed iso-truss [56] AUT positioner

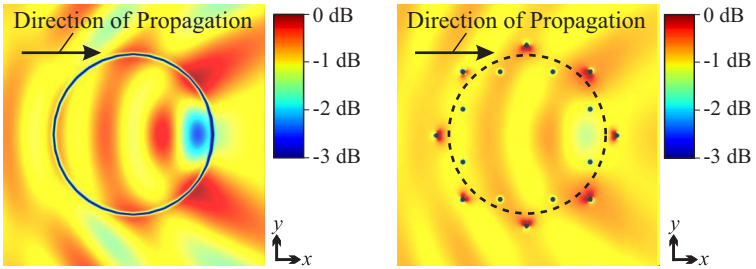

Figure 4.14: AUT positionier reflectivity analysis: (a) cylinder, wall thickness $t = 2\,\text{mm}$; (b) designed iso-truss structure.

The setup is realized using a body phantom constructed from a acrylic container filled with tissue-simulating liquid as can be seen in Fig. 4.15. Manufacturing from silicone-carbon-based mixture is also possible [7], which facilitates usability for the cost of reduced flexibility in regard of the dielectric properties. The absorption at the far end is achieved by utilizing a layer of pyramidal absorbers (Emerson & Cuming WAVASORB® VHP-12). The frame that supports the iso-truss structure as well as the other mechanical components are covered with pyramidal absorbers.

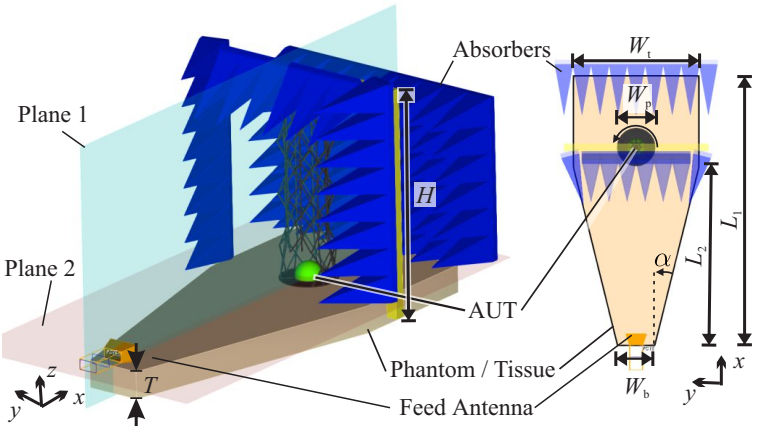

(a)

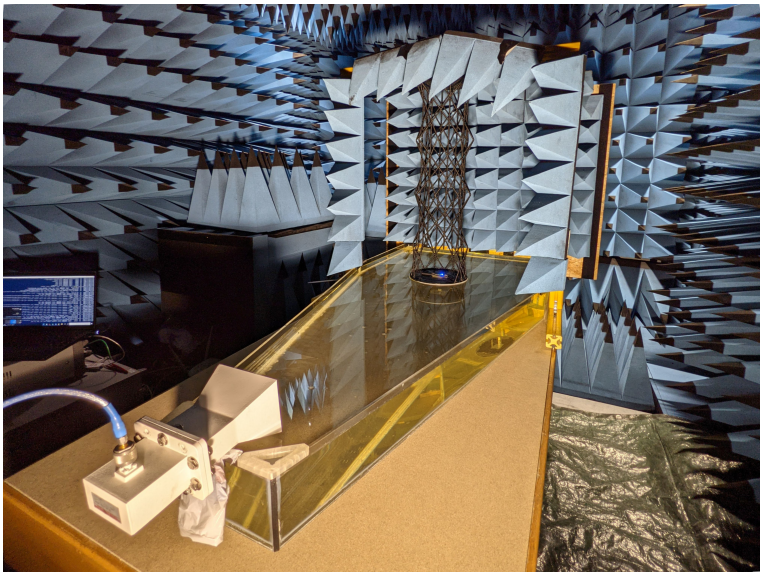

(b)

Figure 4.15: On-body antenna test range setup: (a) CAD drawing with dimensions and reference planes; (b) Picture of realized system [BM212].

Table 4.1: Antenna test range dimensions, ref. Fig. 4.15.

Parameter	Value (mm)
L_1	1500
L_2	1000
W_t	700
W_b	210
W_p	210
H	875
α	23.5°

All dimensions of the realized test range as depicted in Fig. 4.15 can be found in Table 4.1. Fig. 4.16 depicts the results of the numerically evaluated QZ of the complete system. The usable QZ inside the positioner (surrounded by the dash-dotted line) has a horizontal width of $W_\mathrm{QZ} = 200\,\mathrm{mm}$ and spans in height between $z_\mathrm{QZ} \in [-30\mathrm{mm}; 130\mathrm{mm}]$. As can be seen in Fig. 4.16(a) and (b), the amplitude deviation in the test zone of the final setup is $|E_\mathrm{SW}E^{-1}| \leq 1\,\mathrm{dB}$. Also, the maximum phase deviation is $\arg\{E_\mathrm{SW}E^{-1}\} \leq 10°$, ref. Fig 4.16(c) and Fig 4.16(d). Thus, overall the determined QZ dimensions correspond closely to the dimensions estimated analytically above. The reflections on the side walls could be reduced as well. Nevertheless, the QZ is slightly limited in its width, but this does not have any restrictions for the intended applications. In terms of QZ height above the tissue, the estimate is even slightly exceeded. The small extent in height of the QZ within the tissue is due to the reduced thickness of the phantom, which is chosen to minimize the amount of tissue-simulating fluid required. For typical implant applications like pacemakers, which are most often placed subcutaneously [57], the achieved test zone depth is still sufficient. Because of the tapered design, absolute gain measurements, e.g. with the three-antenna method [2], are not possible with designed antenna test range.

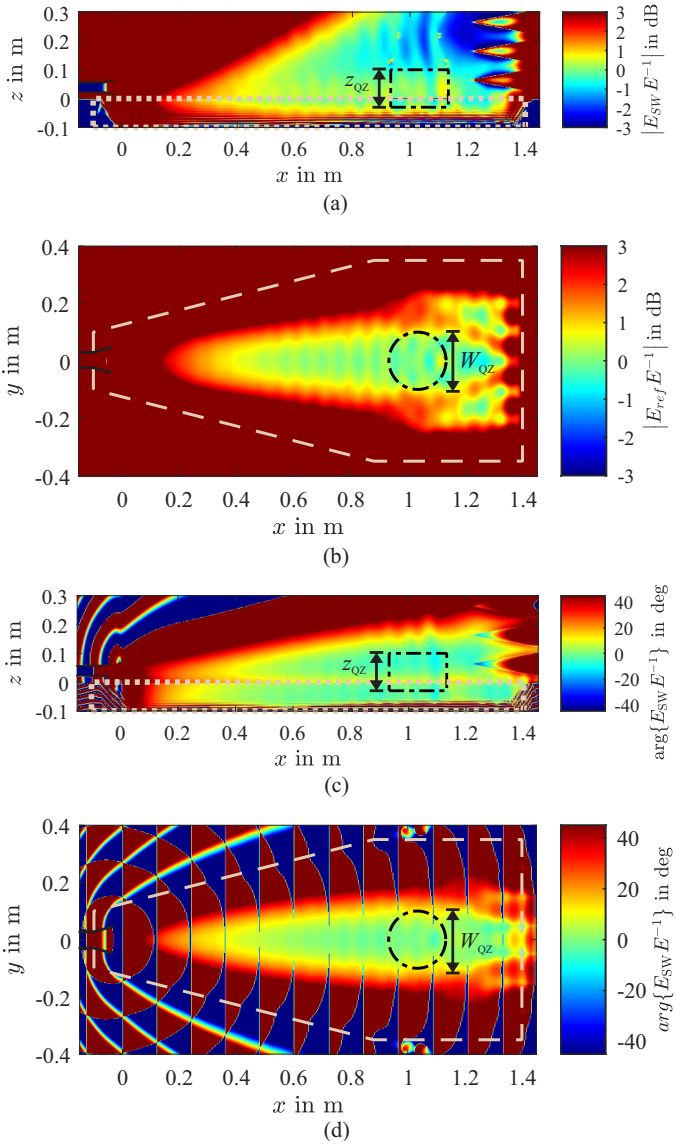

Figure 4.16: QZ: amplitude deviation with final setup: (a) Amplitude variation plane 1; (b) Amplitude variation plane 2; (c) Phase variation plane 1; (d) Phase variation plane 2; Usable QZ inside positioner surrounded by dash-dotted line, the dashed line marks the area of the body phantom [BM212].

4.3.2 Validation

For all measurements, a vertical quarter-wave wire monopole ($l = 28\,\text{mm}$), centrally positioned on a circular-shaped ground plate (diameter $d = 100\,\text{mm}$), is used as the calibration antenna. The associated omnidirectional on-body gain $G_{\text{B,cal}} = 0.25\,\text{dB}$ is determined numerically [BM211]. To realize the body phantom, the container as depicted in Fig. 4.15 is filled with 70 liters of tissue-simulating liquid. The target dielectric properties of $\varepsilon_r = 52.7$ and $\sigma = 1.7\,\text{S/m}$ at $f = 2.45\,\text{GHz}$ were determined assuming homogeneous muscle tissue using the database available for this purpose based on data by C. Gabriel [58]. Based thereon, the tissue-simulating liquid is made of a mixture of deionized water with 40 wt% sucrose according to the formulation in [59]. Its dielectric properties were measured using a coaxial probe ($\varepsilon_r = 52.5$ and $\sigma = 2.5\,\text{S/m}$). The influence of the increased conductivity compared to the target is assumed to be negligible, as the resulting increased path loss appears in all measurements including the calibration.

To validate the developed setup, the on-body pattern of a half-wave slot dipole antenna is measured, since its simple structure can be modeled precisely in the

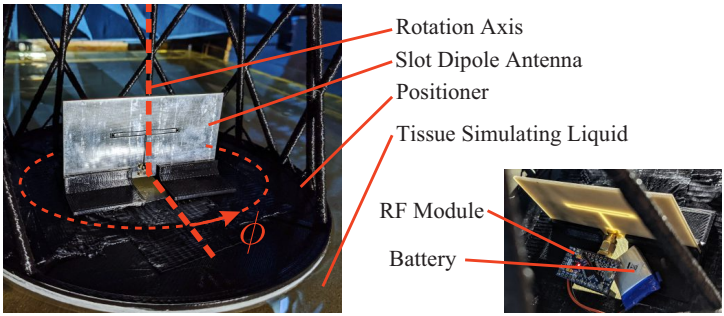

Figure 4.17: Validation measurement: slot dipole antenna with battery-powered RF module inside the positioner [BM212].

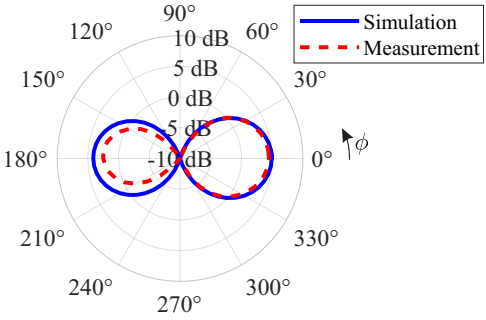

Figure 4.18: Validation measurement: on-body antenna gain pattern of slot dipole antenna [BM212].

numerical simulation used as a reference for the validation. In the measurement, the antenna's ground plate is oriented perpendicular to the tissue surface, ref. Fig 4.17. As can be seen, the antenna is attached to a battery-powered RF module emitting a continuous wave signal at $f = 2.45\,\text{GHz}$. This way, cable effects due to common-mode currents are omitted. The path loss $S_{21,\text{AUT}}$ is calculated from the measured output power of the module and the power received at the feed antenna.

Fig. 4.18 depicts the measured on-body gain pattern compared to the pattern obtained from the numerical simulation. The deviation for angles $\phi \in [90°; 270°]$ can be explained by the influence of the attached RF module feeding the antenna in the measurement, ref. Fig. 4.17. Apart from this, the results of the measurement of the slot dipole antenna with a deviation of 0.3 dB in peak gain reveal an excellent agreement with the simulated pattern and prove the successful implementation of the measurement principle for the desired on-body gain patterns.

4.4 Example Application: Implanted Pacemaker

To evaluate the applicability of the proposed test method using the flat-phantom antenna test range, we analyze the on-body performance of antennas embedded into a cardiac pacemaker. Since recent pacemakers support Bluetooth in the 2.4 GHz ISM-band for communication with standard consumer devices (e.g. smartphones), on-body propagation becomes an important factor with this application [60]. Hence, as depicted in Fig. 4.19 the on-body link between an implanted pacemaker and typical locations of a smartphone, e.g. carried in the pockets, are evaluated.

Three different antennas, a folded dipole, a monopole, and a slot dipole are integrated into the pacemaker as example antennas as can be seen in Fig. 4.20.

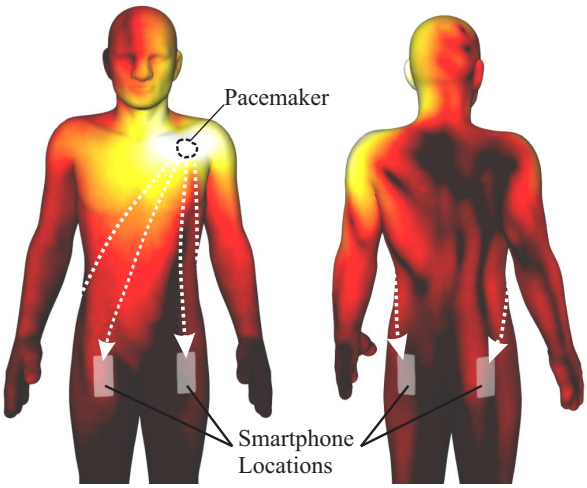

Figure 4.19: Example pacemaker application.

The antennas are realized on a PCB together with a Bluetooth-transceiver which is then encapsulated in epoxy resin, ref. Fig. 4.20. The pacemaker housing enclosing the battery and the lower half of the PCB is 3D-printed, electroplated with copper and finished with epoxy resin. With the developed antenna test range, the on-body gain of all three antennas placed at a depth of $h = -20\,\text{mm}$ inside the tissue-simulating liquid is measured. Therefore, a spectrum analyzer connected to the feed antenna measures the power of the Bluetooth advertising packets emitted by the Bluetooth-transceivers inside the pacemakers. Hence, results for the on-body gain at the three Bluetooth advertising channels at $f \in$[2.042 GHz, 2.426 GHz, 2.480 GHz] are gathered.

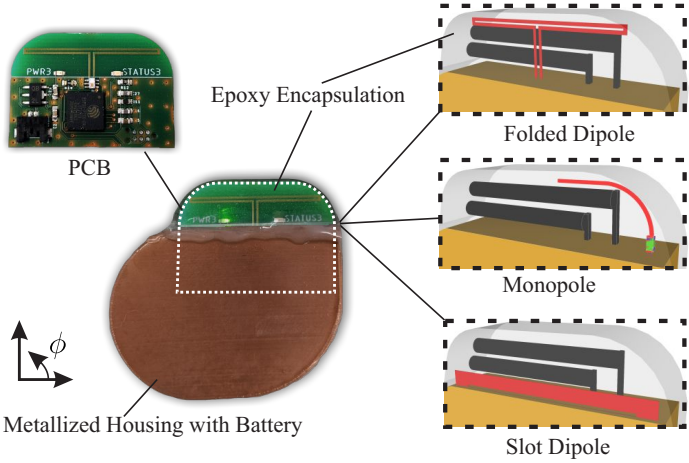

Figure 4.20: Cardiac pacemaker example application with three different antenna structures integrated [BM212].

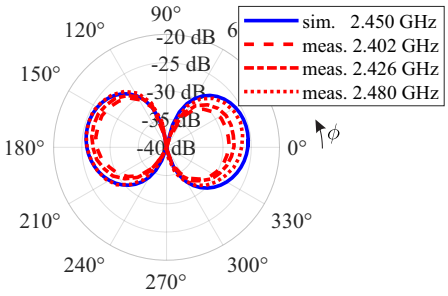

(a) Folded Dipole

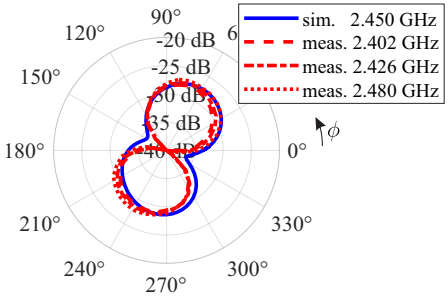

(b) Monopole

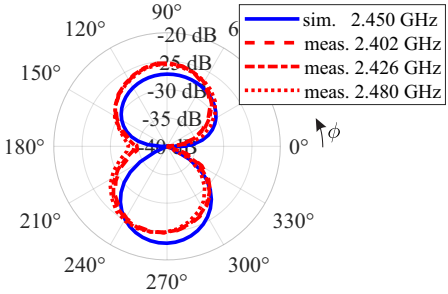

(c) Slot dipole

Figure 4.21: Measured on-body gain of pacemaker antennas compared to simulation results [BM212].

As can be seen in Fig. 4.21, the measured on-body gain of the antennas agrees reasonably well with the simulated values. The patterns of all three antennas are of similar shape, but rotated in the diagram resulting in different directions for lobes and nulls. In addition, the peak gain between the different structures differs with the monopole having the lowest peak gain ($G_{\mathrm{B,max}} = -26\,\mathrm{dB}$) and the slot dipole having the highest gain ($G_{\mathrm{B,max}} = -23.7\,\mathrm{dB}$) of all three antennas. We will come back to these observations later when we discuss the path loss performance of the in-situ tests.

To showcase the insights that the on-body patterns offer, in-situ path-loss measurements of the implanted pacemakers communicating with a Bluetooth node (e.g. Smartphone) located at different positions on the body are evaluated. In order to keep the complexity limited at this point, a cylindrical phantom having a diameter of $d = 300\,\mathrm{mm}$ and height of $l = 1000\,\mathrm{mm}$ is used for the in-situ tests. The phantom is built from a acrylic tube (wall thickness $t = 4\,\mathrm{mm}$) filled with tissue-simulating liquid with the same properties as in the on-body gain measurements.

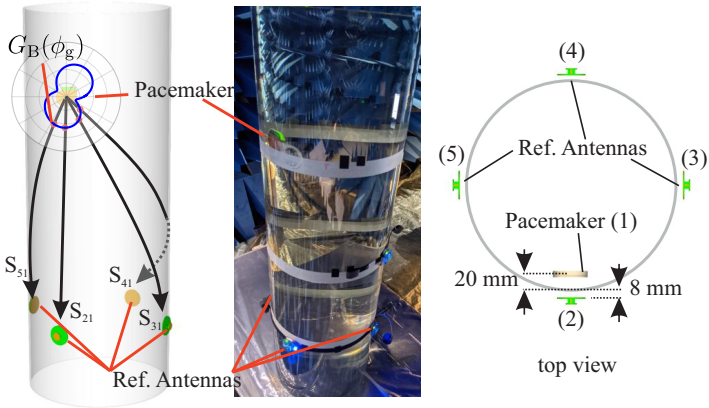

Figure 4.22: In-situ measurement setup for the pacemaker example application [BM212].

The pacemaker antennas are again placed at a depth of $h = -20\,\text{mm}$ inside the liquid. As reference antennas four top-loaded monopole antennas (omnidirectional on-body gain $G_B = 1.7\,\text{dB}$) are used which are also integrated with a Bluetooth transceiver on a single PCB as shown in Fig. 4.23. Thus, the path loss can be estimated over-the-air (OTA) with the Bluetooth received signal strength indicator (RSSI). This way, cable effects are avoided. The four reference antennas (ports 2-5) are placed circumferentially around the cylinder with an axial separation of 0.5 m to the location of the pacemaker, as can be seen in Fig. 4.22. To account for fading effects, the measurements are repeated five times, whereby each time the antennas are displaced circumferentially by about $\lambda/8$. Also, the path loss is measured in all three Bluetooth advertising channels and the results are combined for the plot in Fig. 4.24. Here, the measured value range of the path loss at each position of the reference antennas is displayed as a boxplot. As expected, due to fading, at some positions the measured path loss varies strongly within a range of up to 20 dB. This phenomenon is especially pronounced with antenna 4 which is located at the opposite side of the phantom with respect to the pacemaker, since the length and thus the path loss of the left and right-hand paths of the surface waves is equal here and the two propagation paths lead to a

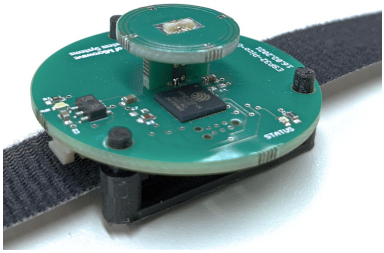

Figure 4.23: Reference antenna: top-loaded monopole integrated together with a Bluetooth-transceiver IC.

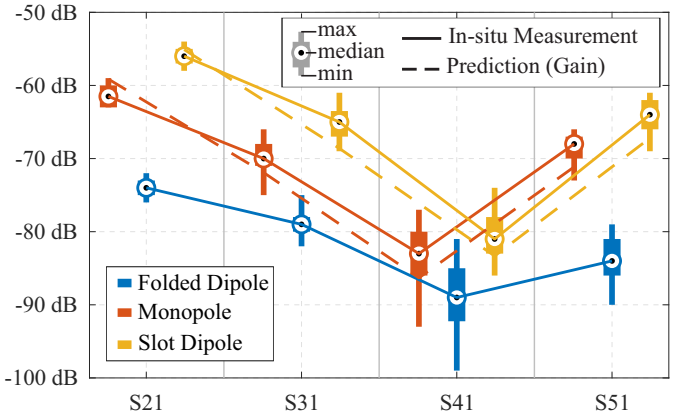

Figure 4.24: Results of the path loss measurements as depicted in Fig. 4.22 [BM212].

strong fading profile at this position. A meaningful comparison between the different antennas investigated only becomes possible by looking at the mean path loss from multiple measurements, ref. Fig. 4.24 (marked by circles with dots). Particularly, significant differences can be found with the antennas in positions 2 and 5. Here, the path loss differs by up to 20 dB in comparison between the different pacemaker antennas.

Now, it is interesting to notice that these effects on the path loss can be easily predicted from the measured on-body gain of the antennas in Fig. 4.21(a)-(c). Looking at the gain of the folded dipole antenna in Fig. 4.21(a), the poor performance of the link to antenna 2 can be explained by the null of the on-body pattern in the downward direction. The slot dipole has overall the highest gain in the downward direction, therefore the overall observed path loss is the lowest. For the monopole antenna, the gain lobe is directed downward to the left. Thus, the path loss to the left side (position 5) is reduced.

The illustrative interpretation as discussed above can be quantified for all antennas and all positions in the in-situ example. Based on the assumption that the on-body gain is in average proportional to the overall path loss, the measured path loss with the folded dipole antenna is used as a baseline. From the gain difference in direction of the geodesics to the reference antennas $G_{\mathrm{B}}(\phi_{\mathrm{g}})$, see Fig. 4.22, the path loss of the other two antennas is calculated (all parameters in log-scale / dB):

$$S_{21,\text{pred.,i}} = S_{21,\text{base}} + G_{\mathrm{B,i}}(\phi_{\mathrm{g}}) - G_{\mathrm{B,base}}(\phi_{\mathrm{g}}), \tag{4.9}$$

with $S_{21,\text{base}}$ and $G_{\mathrm{B,base}}$ being the measured path loss and on-body gain of the folded dipole antenna, and $G_{\mathrm{B,i}}$ the measured on-body gain of the monopole or slot dipole antenna, respectively.

The results are also plotted in Fig. 4.24, where the solid lines highlight the mean path loss obtained from the in-situ measurements, and the dashed lines depict the prediction from the gain difference added to the path loss of the folded dipole antenna. As can be seen, the overall performance can be predicted well with discrepancies of only a few dB. Also, the ranking of the performance of all three antennas is correct in the prediction at all positions.

4.5 Discussion

Based on the on-body far field as derived in Chapter 3, on-body antenna parameters have been developed. As shown by various examples, the on-body antenna parameters are beneficial as they enable a de-embedded characterization of the antenna itself, excluding any influence of the subsequent application. The specific quantification of an antenna's suitability for on-body propagation enables an objective evaluation of the antennas and the assessment of dedicated on-body antenna design specifications. Since the underlying principles of propagation along the dissipative body surface are similar even with curved body contours, the derived antenna parameters are also valid, as shown in the examples.

As evaluated in Chapter 3, for the on-body domain, surface waves traveling along the body's surface can be considered the dominating propagation mechanism in most cases. The derived on-body far-field as well as the modeling based on the on-body antenna parameters as described in this chapter, accordingly, also require that surface waves are the main propagation principle for any application to be considered. Therefore, as derived with the definition of the on-body far-field region in Chapter 3, the electrical height h of the antenna above the body surface must be small, which in the usually used WBAN frequency bands (low GHz range) is in accordance with the standard low profile requirements for portability. On the other hand, no limits need to be set for the implantation depth of in-body antennas since the corresponding Green's functions are assembled from the case with $h = 0$.

Furthermore, the on-body Green's functions utilized in the derivation of the on-body far-field in Chapter 3 as well as the on-body antenna parameters in this chapter were derived assuming a single homogeneous tissue. This is a reasonable simplification regarding the propagation properties at sufficiently low frequencies [22]. Due to the decreasing skin depth for higher frequencies, the Green's

functions must be adapted for considering a multilayered tissue model, for the necessary adjustments ref. [22], [45]. However, the simplifying assumption of a homogeneous half-space can be made at millimeter-wave frequencies again. In this case, the dielectric properties of the skin must be considered, as the penetration depth becomes so small that underlying tissues can be neglected [26]. Apart from the influence of tissue modeling on propagation, especially with implantable antennas, the antenna properties are strongly impaired by the surrounding tissue [61]. The homogeneous or layered tissue representation is to be seen critically here. However, the tissue in the immediate vicinity of the antenna can be modeled during the numerical calculation of the antenna's near-field, ref. Chapter 4.

Due to the developed measurement procedures, e.g., with the antenna range as designed in Chapter 4.3, high practical relevance of the developed methods is achieved. Thus, all advantages of the de-embedded on-body antenna characterization also apply to the validation of physical prototypes. For the development of these measurement systems, especially the defined far-field region is important in order to qualify the system and ensure agreement in the results compared to numerical calculated parameters. The proposed antenna range has been developed for a target frequency of 2.45 GHz. For lower frequencies, the cross-section of the required horn antenna increases and thus also the maximum height h of the antenna above the tissue surface as well as the necessary on-body far-field distance, ref. Chapter 3.3. The phantom required for the antenna range would therefore have to be enlarged. As discussed above, for higher frequencies, multilayered phantoms may be needed. In terms of realization complexity this is a benefit of the proposed measurement approach, as only a flat phantom is needed, compared to the complex body shapes used for in-situ measurements. A two-layer (fat and muscle) flat phantom, as required for the proposed measurement approach, has already been presented in [62]. Furthermore, for any application scenario considered, the body surface in the direct vicinity of the antenna must be sufficiently flat to correctly characterize the on-body gain. Otherwise, protruding

body parts, as e.g. the ear for hearing aid applications, can be taken into account as part of the antenna [BM211]. In the measurement, these need to be physically modeled and added to the positioner.

As shown by the examples evaluated in Chapter 4.2.1 and 4.2.2, the on-body antenna parameters and the determined transmission equation, analogous to the Friis equation in free space, can also be used to model the entire wireless system. In the same way, the antenna can be optimized based on the on-body gain by maximizing the on-body gain in the direction of the most relevant propagation path. However, the difficulty here lies in the determination of the channel model. The determination is only possible via analytical methods for clear separation from the antenna. In this case, the complex, variable body geometries and the complex interaction of the fields and the body tissue lead to a high modeling effort. Examples from the literature as evaluated in Chapter 2.2.2 show that such modeling is possible in principle, but it is costly and not universally possible for any application as described above. However, given the high effort of analytical channel modeling, a numerical solution may be more appropriate. For this, the reader is referred to the following Chapter 5. As the last evaluated example in Chapter 4.4 shows, for applications with an approximately static channel and with negligible fading, antenna optimization is possible even without the analytical calculation of a channel model.

Chapter 5

SWF Channel Modeling and Antenna De-Embedding

As shown in the previous chapters, modeling of antennas for the on-body domain is possible using adapted methods by characterizing the directional radiation properties. However, as the analysis of the state-of-the-art (ref. Chapter 2.2.2) shows, it is difficult to find a universal method for the analytical calculation of directional on-body channel models due to the great variety of applications.

Therefore, in this chapter, the developed on-body antenna parameters are complemented with a modeling approach based on spherical wave functions (SWF) to enable also de-embedded channel models. Here, the channel is characterized by the coupling between all SWF at the source and the receiver. The numerical implementation of this method enables a universal channel modeling method for any on-body applications. Furthermore, a possibility is derived to calculate optimal antenna characteristics for a given SWF channel model. By the combination of the SWF modeling with the previously developed on-body antenna parameters an antenna optimization method for the on-body domain is developed.[10]

[10]This chapter is based on the following publications: [Ber+22, BM19, MBM22] (©2022 IEEE).

5.1 SWF Modeling

Spherical wave functions represent a complete and orthogonal set of basis functions for solutions to Maxwell's equations. Any electrical field can be decomposed into a linear combination of SWF at an arbitrary origin point by [63]:

$$\mathbf{E} \approx k\sqrt{\eta_0} \sum_{j=1}^{J} \left(b_j \mathbf{F}_j^{(4)} + a_j \mathbf{F}_j^{(3)} \right), \tag{5.1}$$

where k is the wavenumber, η_0 is the wave impedance of free-space, and j is the mode index.[11] $\mathbf{F}_j^{(4)}$ represent outgoing SWF and $b_j \in \mathbb{C}$ are the associated weighting coefficients. Accordingly, $\mathbf{F}_j^{(3)}$ and $a_j \in \mathbb{C}$ represent incoming SWF.[12] For the mathematical definition of the term $\mathbf{F}_j^{(c)}$ ref. appendix D. Theoretically, an infinite number of SWF modes J is necessary for the description of arbitrary fields. However, it is well known that fields radiated by antennas can practically be characterized by a finite number of modes due to the radial cut-off property[13] of $\mathbf{F}_j^{(c)}$ [63].

As shown by Pirkl, the coupling between two antennas in arbitrary environments can be described utilizing spherical wave scattering matrices [64]. If this is applied to WBAN, the channel is partly formed by body tissue, as depicted in Fig. 5.1. If the link between a transmitting antenna 1 and a receiving antenna 2 is to be calculated, the transmission vector $\mathbf{T}_1 \in \mathbb{C}^{J\times 1}$ quantifies the transitional behavior between the incident wave v_1 at the physical port 1, and the vector $\mathbf{b}_1 \in \mathbb{C}^{J\times 1}$ consisting of all outgoing SWF coefficient b_j at antenna 1 (assuming $\mathbf{a}_1 = \mathbf{0}$) as:

$$\mathbf{b}_1 = \mathbf{T}_1 v_1 \,. \tag{5.2}$$

[11] The variable j is used here both as a running index (to remain compatible with the literature) and as the imaginary unit. As the index only occurs in subscripts, keeping them separate is possible.
[12] In contrast to [63], the time-dependence $e^{j\omega t}$ is utilized.
[13] See appendix E for more details on the cut-off property and the mode truncation.

$\mathbf{T}_1$ can be calculated numerically from the radiated fields of the transmitting antenna by assuming only coefficients for outgoing waves b_j in (5.1). The receiving vector $\mathbf{R}_2 \in \mathbb{C}^{1\times J}$ of antenna 2 can be defined equivalently (assuming $\mathbf{b}_2 = \mathbf{0}$) as:

$$w_2 = \mathbf{R}_2 \mathbf{a}_2, \tag{5.3}$$

with w_2 the outgoing wave at the physical port 2 and $\mathbf{a}_2 \in \mathbb{C}^{J\times 1}$ the SWF coefficient vector consisting of the coefficients a_j of all incoming SWF. For reciprocal antennas, $\mathbf{R}_2$ can be calculated from $\mathbf{T}_2$ and vice versa [63]. Incoming waves at the antennas are also partially re-radiated/backscattered, which is quantified e.g. for antenna 1 by the scattering matrix $\mathbf{S}_1 \in \mathbb{C}^{J\times J}$. Finally, the free-space input reflection coefficient at the physical port of e.g. antenna 1 is defined as Γ_1.

SWF channel modeling is based on the SWF scattering matrices $\mathbf{M}_{mn} \in \mathbb{C}^{J\times J}$, ref. Fig. 5.1. For example, the transmission from antenna 1 in form of the outgoing spherical waves $\mathbf{b}_1$ to the incoming waves $\mathbf{a}_2$ at antenna 2 is described by

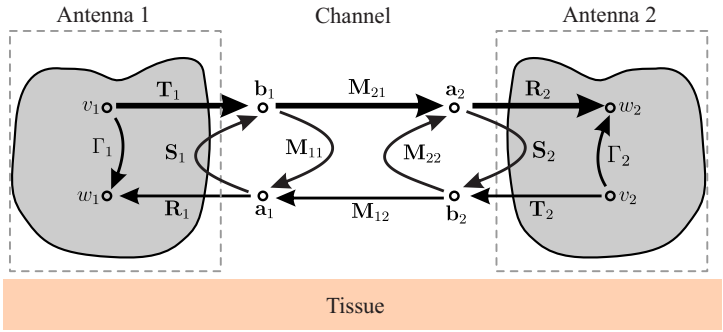

Figure 5.1: Antenna coupling between two antennas in the presence of body tissue. The SWF scattering matrices $\mathbf{M}_{mn}$ describe the mode-to-mode transmission and reflection behavior of the channel. Antennas are characterized by their SWF transmitting and receiving behavior denoted by the vectors $\mathbf{T}$ and $\mathbf{R}$. [Ber+22]

(assuming $\mathbf{b}_2 = 0$):

$$\mathbf{a}_2 = \mathbf{M}_{21}\,\mathbf{b}_1. \tag{5.4}$$

Based on SWF modeling, the near-field coupling of the antennas with the body tissue can be described as backscattering of the channel and can be characterized by:

$$\mathbf{a}_1 = \mathbf{M}_{11}\mathbf{b}_1. \tag{5.5}$$

As shown by Pirkl [64], the SWF scattering matrices of the channel can be calculated numerically. In the most simple case, with ideally matched antennas ($\Gamma = 0$) and a channel with negligible back scattering ($\mathbf{M}_{11} = \mathbf{M}_{22} \approx \mathbf{0}$), the narrow-band transmission coefficient S_{21} can be calculated as [65]:

$$S_{21} = w_2 v_1^{-1} = \mathbf{R_2}\,\mathbf{M_{21}}\,\mathbf{T_1}. \tag{5.6}$$

As can be seen from (5.6), the system is now separated into three building blocks for antennas and channel, similar as with the Friis transmission equation (2.9). Once the channel is characterized with $\mathbf{M}_{21}$, the transmission coefficient with any combination of antennas $\mathbf{R}_2$, $\mathbf{T}_1$ can be calculated by simply carrying out the matrix multiplication in (5.6). Thus, for optimizing the antenna for a specific application the channel matrices $\mathbf{M}_{21}$ to all possible receiver locations can be calculated first. Then, the link to all considered receiving locations can be calculated using (5.6) with every design iteration from a single simulation of the transmitting antenna by recalculating $\mathbf{T}_1$.

5.2 SWF Antenna De-Embedding in Presence of a Backscatterer

A difficulty that arises specifically when applying SWF antenna de-embedding for WBAN is that due to the near-field coupling of the antennas with the tissue, the assumption ($\mathbf{M}_{11}$=$\mathbf{M}_{22} \approx \mathbf{0}$) is not valid. Therefore, the system response (5.6) becomes [64]:

$$S_{21} = \mathbf{R}_2 \underbrace{(\mathbf{I} - \mathbf{M}_{22}\mathbf{S}_2)^{-1}}_{\mathbf{K}_2} \mathbf{M}_{21} \underbrace{(\mathbf{I} - \mathbf{S}_1\mathbf{M}_{11})^{-1}}_{\mathbf{K}_1} \mathbf{T}_1, \tag{5.7}$$

where the matrices $\mathbf{K}_1$ and $\mathbf{K}_2$ account for multiple scattering between the antennas and their environment. The influence of the backscattering from the receiving antenna 2 to antenna 1 through $\mathbf{M}_{12}$, ref. Fig. 5.1, is neglected. Compared to (5.6), determining all necessary parameters of channel and antennas in (5.7) increases the computational effort significantly [64]. To make the SWF de-embedding approach for WBAN more straightforward and applicable with standard commercial simulation software, an alternative, single-step antenna de-embedding scheme is derived in the following. The antenna de-embedding problem as depicted in Fig. 5.1 can be reduced to the one shown in Fig. 5.2(a) if the influence of the second antenna on the input reflection coefficient of the first antenna can be neglected. The outgoing waves $\mathbf{b}_1$ of the transmitting antenna are then determined by:

$$\mathbf{b}_1 = \mathbf{T}_1 v_1 + \mathbf{S}_1 \mathbf{a}_1. \tag{5.8}$$

If the radiated fields of an antenna are characterized trough $\mathbf{a}_1$ and $\mathbf{b}_1$, in (5.8) there are two unknowns: $\mathbf{S}_1$ and $\mathbf{T}_1$. Thus, a direct solution as above in (5.2) is not possible. To circumvent this problem, the radiating antenna is virtually removed from the scenario and replaced by equivalent currents ($\mathbf{J}_{\text{eq}}$, $\mathbf{M}_{\text{eq}}$) on an enclosing

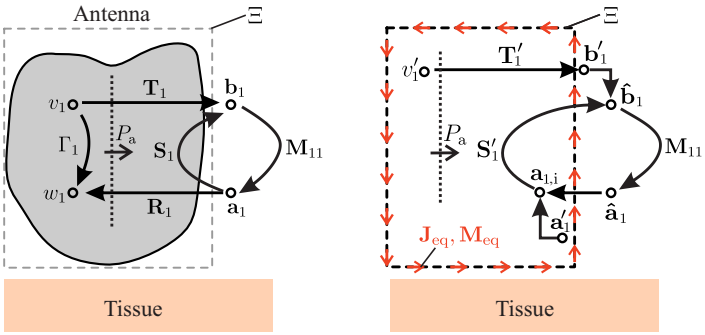

Figure 5.2: Antenna scattering matrix in WBAN scenario. (a) Original scenario; (b) Surface equivalence theorem: equivalent currents $\mathbf{J}_{eq}, \mathbf{M}_{eq}$ on enclosure Ξ excite outgoing waves $\mathbf{b}_1'$ and incoming waves $\mathbf{a}_1'$ [Ber+22]

surface Ξ, ref. Fig. 5.2(b), according to the surface equivalence theorem [52][14]. The interior of the surface Ξ is now assumed to be empty space, such as the antenna's SWF scattering matrix becomes equal to the unity matrix $\mathbf{S}_1' = \mathbf{I}$, because the origin reflects every incoming SWF as the corresponding outgoing SWF (similar to an open termination with guided waves).

Furthermore, the currents $\mathbf{J}_{eq}$ and $\mathbf{M}_{eq}$ are determined with the constraint that they excite only outgoing waves ($\mathbf{a}_1' = 0$, ref. Fig. 5.2(b)). If now the outgoing waves excited by $\mathbf{J}_{eq}$ and $\mathbf{M}_{eq}$ are chosen as [MBM22]:

$$\mathbf{b}_1' = \mathbf{b}_1 - \mathbf{a}_1, \tag{5.9}$$

[14] Same procedure as with the on-body propagation modeling, ref. Chapter 3.1.2.

the overall SWF coefficients $\hat{\mathbf{b}}_1$ and $\hat{\mathbf{a}}_1$ in the equivalent setup, ref. Fig. 5.2(b), and thus the fields outside Ξ remain equal to the original setup in Fig 5.2(a):[15]

$$\hat{\mathbf{b}}_1 = \mathbf{b}'_1 + \mathbf{I}\mathbf{a}_1 = \mathbf{b}_1; \qquad \hat{\mathbf{a}}_1 = \mathbf{M_{11}}\hat{\mathbf{b}}_1 = \mathbf{a}_1. \tag{5.10}$$

The computational complexity of (5.8) is reduced, since $\mathbf{T}'_1$ is now readily available from:

$$\mathbf{b}'_1 = \mathbf{T}'_1 v'_1. \tag{5.11}$$

To keep the accepted port power P_a constant between the original domain, ref. Fig. 5.2(a) and the equivalent problem, ref. Fig. 5.2(b), the virtual port signal in (5.11) is defined as $v'_1 = \sqrt{2P_\mathrm{a}} = \sqrt{|v_1|^2 - |w_1|^2}$.

Instead of obtaining the coefficients a_j and b_j separately, the coefficients b'_j of the vector $\mathbf{b}'_1$ in (5.9) can be calculated directly from the near field of the antenna using a regular wave $\mathbf{F}_j^{(1)}$:

$$b'_j = b_j - a_j = \frac{2k}{j\sqrt{\eta}} \left\langle \mathbf{E}, \mathbf{F}_j^{(1)*} \right\rangle. \tag{5.12}$$

Here, the SWF decomposition is performed on the surface Ξ with the notation:

$$\langle \mathbf{u}, \mathbf{v} \rangle = \oiint_\Xi \{\mathbf{u} \times (\nabla \times \mathbf{v}) - \mathbf{v} \times (\nabla \times \mathbf{u})\} \, \mathbf{n}_\Xi \, \mathrm{d}\Xi, \tag{5.13}$$

where $\mathbf{n}_X i$ is the surface normal pointing out of the closed surface Ξ.

Using regular SWF in the decomposition is also numerically superior compared to calculating **b** or **a** independently, as Santiago et al. have recently shown [66]. The receive vector $\mathbf{R}'_2$ of the equivalent problem can be found from $\mathbf{T}'_2$ using reciprocity [63]. Finally, for adopting the channel response S_{21} in (5.4) to the

[15] It is interesting to note here that although the excited currents radiate only outwards, the fields inside Ξ are non-zero and consist of the incoming waves $\mathbf{a}_{1,\mathrm{i}} = \mathbf{M}_{11}\mathbf{b}$.

modified coefficients $\mathbf{b}'$, an alternative mode-to-mode transmission matrix $\mathbf{M}'_{21}$ is defined as:

$$\mathbf{a}'_2 = \mathbf{M}'_{21}(\mathbf{b}_1 - \mathbf{a}_1) = \mathbf{M}'_{21}\mathbf{b}'_1, \tag{5.14}$$

where $\mathbf{a}'_2$ are the incoming waves at the location of the receiving antenna in the equivalent problem with removed antennas, ref. Fig. 5.2(b).

By resolving the loop between $\mathbf{M}_{11}$ and $\mathbf{S}$ in Fig. 5.2(b) according to signal flow graph theory, the relation to the original SWF channel transmission matrix is determined as:

$$\mathbf{M}'_{21} = \left(\mathbf{I} - \mathbf{M}_{22}\mathbf{S}'_2\right)^{-1} \mathbf{M}_{21} \left(\mathbf{I} - \mathbf{S}'_1\mathbf{M}_{11}\right)^{-1}. \tag{5.15}$$

As can be seen from the equation, the adapted SWF channel transmission matrix $\mathbf{M}'_{21}$ already includes the influence of the backscattering of the channel for the equivalent problem with removed antennas. The channel response of the equivalent problem is then calculated as:

$$S_{21} = \mathbf{R}'_2\mathbf{M}'_{21}\mathbf{T}'_1. \tag{5.16}$$

Concluding, (5.7) has been rearranged to the simple form (5.16) with only three parameters to be determined as in (5.6).

5.3 Antenna Optimization Using SWF

Up to this point, the SWF antenna de-embedding for WBAN is used solely as a modeling approach for enabling an efficient assessment of the behavior of different antennas in a channel. In contrast to the concept of using directional channel models and optimizing antennas by means of their on-body gain as described in Chapter 4, antenna optimization with SWF modeling still is trial and error. However, as will be shown in the following, SWF modeling can also be used for antenna optimization.

To optimize the transmitting antenna, the goal is to maximize the power of the incoming waves $\mathbf{a}'_2$ at the receiver position. Without loss of generality, the Euclidean norm of the outgoing wave coefficient vector can be set to $\|\mathbf{b}'_1\|_2 = 1$ and the optimization problem can be formulated as:

$$\max \|\mathbf{a}'_2\|_2 = \max_{\|\mathbf{b}'_1\|_2=1} \|\mathbf{M}'_{21}\mathbf{b}'_1\|_2 \,. \tag{5.17}$$

Assuming a known SWF channel transmission matrix $\mathbf{M}'_{21}$, the optimal excitation $\mathbf{b}'_{1,\text{opt}}$ is sought. By using the definition of the spectral norm, the optimum can be calculated analytically as [67]:

$$\max_{\|\mathbf{b}'_1\|_2=1} \|\mathbf{M}'_{21}\mathbf{b}'_1\|_2 = \sqrt{\left\|\mathbf{M}'^{\mathrm{H}}_{21}\,\mathbf{M}'_{21}\right\|_2} = \sqrt{\lambda_{\max}}, \tag{5.18}$$

where $\lambda_{\max}$ is the largest eigenvalue of $\mathbf{M}'^{\mathrm{H}}_{21}\,\mathbf{M}'_{21}$. Finally, the corresponding eigenvector is the optimal excitation $\mathbf{b}'_{1,\text{opt}}$. For calculating the transmission coefficient (5.16) with the optimal excitation, $\mathbf{T}'_{1,\text{opt}}$ is calculated using (5.11) as:

$$\mathbf{T}'_{1,\text{opt}} = \frac{1}{\sqrt{2P_{\text{a}}}}\mathbf{b}'_{1,\text{opt}}. \tag{5.19}$$

If the optimal antenna is assumed to be lossless, the accepted power P_a is identical to the radiated power P_rad going through Ξ in Fig. 5.2(b) and can be calculated:

$$P_\mathrm{a} = P_\mathrm{rad} = \frac{1}{2}\left(\|\hat{\mathbf{b}_1}\|_2^2 - \|\hat{\mathbf{a}_1}\|_2^2\right) . \tag{5.20}$$

Using the signal flow graph in Fig. 5.2(b), this can be written as:

$$P_\mathrm{a} = \frac{1}{2} + \mathrm{Re}\left\{\left(\left(\mathbf{I} - \mathbf{M}_{11}\right)^{-1}\mathbf{M}_{11}\mathbf{b}_1'\right)^\mathrm{H}\mathbf{b}_1'\right\} . \tag{5.21}$$

While the vector $\mathbf{T}'_{1,\mathrm{opt}}$ already represents the optimal solution (in a spherical basis), antenna designers typically do not think in terms of spherical wave coefficients, so $\mathbf{T}'_{1,\mathrm{opt}}$ is a quite abstract parameter. Therefore, a visualization of the calculated optimal antenna properties for a given channel will be derived. For this matter, the on-body gain as defined in Chapter 4 is calculated for the optimal antenna. Hence, for each individual spherical mode j to be considered, equivalent currents $(\mathbf{J}_j, \mathbf{M}_j)$ on surface Ξ, ref. Fig.5.2(b), are defined analytically:

$$\mathbf{J}_j = \mathbf{n} \times \left(\frac{ikv}{\sqrt{\eta}}\mathbf{F}_{\bar{j}}^{(4)}(\mathbf{r}_\Xi)\right) , \tag{5.22}$$

$$\mathbf{M}_j = -\mathbf{n} \times \left(k\sqrt{\eta}v\mathbf{F}_j^{(4)}(\mathbf{r}_\Xi)\right) , \tag{5.23}$$

with i being the imaginary unit and $\mathbf{r}_\Xi$ the position vectors on the surface Ξ. The on-body far fields radiated by the optimal antenna can then be calculated by:

$$\mathbf{E} = \oiint_\Xi \sum_{j=1}^{J} b'_{j,\mathrm{opt}}\left(\overline{\mathbf{G}}_\mathrm{J}\cdot\mathbf{J}_j + \overline{\mathbf{G}}_\mathrm{M}\cdot\mathbf{M}_j\right)\mathrm{d}\Xi \tag{5.24}$$

where $\overline{\mathbf{G}}_\mathrm{J}$ and $\overline{\mathbf{G}}_\mathrm{M}$ denote the dyadic Green's functions for the on-body case approximated by a tissue half-space as derived in Chapter 3, and $b'_{j,\mathrm{opt}}$ the individ-

ual coefficients in $\mathbf{b}'_{\text{opt}}$. The on-body gain can then be calculated using (4.4), ref. Chapter 4.

5.4 Example Application: Antenna for Eye-Wear Applications

An antenna for eye-wear applications in the 2.4 GHz ISM-band is designed and tested as an example in the following to implement and evaluate the methods as derived above. The antenna is supposed to be integrated in the right glasses temple as can be seen in Fig. 5.3(a). Thus, the available antenna integration space has a volume of $(d_x \times d_y \times d_z) = (60 \times 10 \times 7.5)\,\text{mm}^3$, respectively $(0.5 \times 0.08 \times 0.06)\,\lambda^3$ at $f = 2.45\,\text{GHz}$.

In the following, the node with the antenna integrated into the glasses is referred to as the transmitter. The RF link from the glasses to a receiver (e.g. a smartphone), which is assumed to be carried in a trouser pocket, is optimized. Given the selected application, the antenna optimization is performed exclusively for the transmitter. As the receiver, the same top-loaded monopole antenna as in Chapter 4.3.2 (isotropic on-body gain $G_{\text{B}} = 1.7\,\text{dB}$) is utilized as a simplified placeholder, e.g. of a smartphone. Four different possible positions of the receiver are considered, ref. Fig. 5.3(b). The modeling approach should take the influence of posing and different anatomies into account. Therefore, considering different anatomies, three different body phantoms are chosen as depicted in Fig. 5.3(c), an average tall woman ($h = 1.6\,\text{m}$) and man ($h = 1.8\,\text{m}$) are considered, as well as a particularly tall, portly man ($h = 2\,\text{m}$). As can be seen in Fig. 5.3(d), with regard to posing, five different head rotation angles are considered, since this parameter is assumed to have the biggest effect on the on-body propagation in the chosen example. Thus, in total 60 different channel matrices are considered.

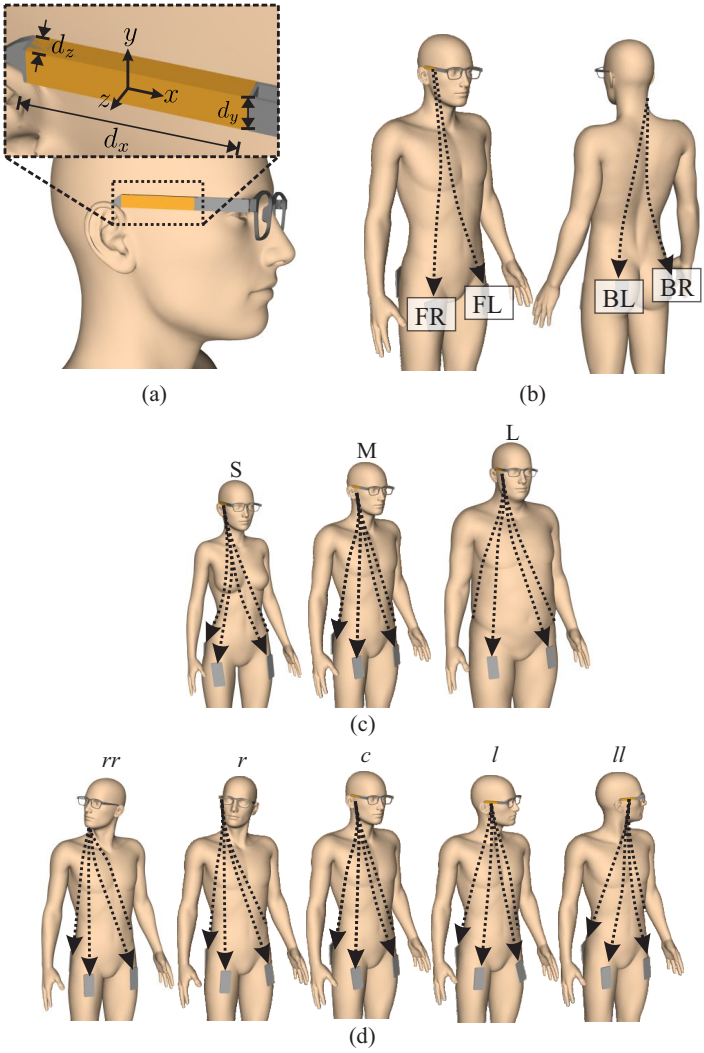

Figure 5.3: Example application of antenna for eye-wear application: (a) Antenna integration volume; (b) Receiver locations: front-left (FL) to back-right (BR); (c) Anatomies: small (S) to large (L); (d) Body poses (head rotation): right-right (*rr*) to left-left (*ll*) [Ber+22]

5.4.1 SWF Channel Modeling

For the channel modeling with regard to antenna de-embedding as derived in Chapter 5.2, the transmission matrix $\mathbf{M}'_{21}$ needs to be calculated. The numerical calculation procedure is realized as a sequential excitation of each SWF mode in place of the antenna by a near-field source, which is usually part of standard EM modeling software. The implementation is outlined in Fig. 5.4. Here, the near-field source must be transparent and non-scattering so that the incoming waves can pass through unhindered. This is necessary so that the assumptions made for the equivalent problem, ref. Fig 5.2(b), are valid. The surface Ξ_1, that encloses the transmitting antenna, is used for the excitation, ref. Fig. 5.4 (top left).

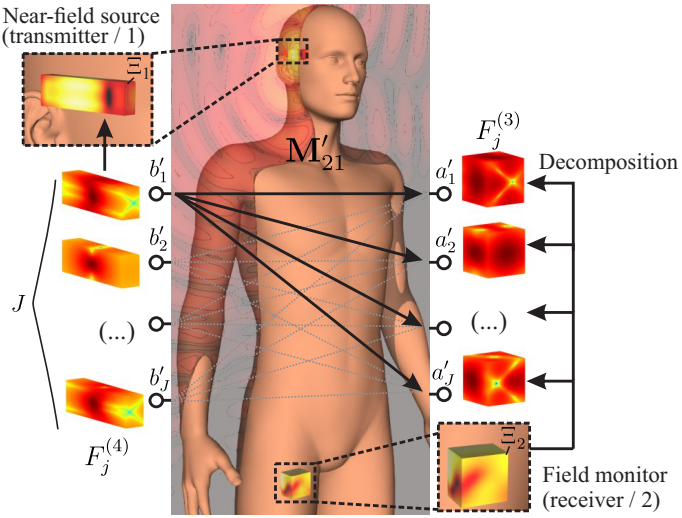

Figure 5.4: SWF channel modeling: A near-field source is used to excite the SWF modes b_j sequentially (top left). At the receiver position (bottom right), the incident fields are recorded and decomposed into vectors of incoming waves **a** [Ber+22].

Based on (5.1), for each mode j, the fields to excite on Ξ_1 are calculated as:

$$\mathbf{E}_j = k\sqrt{\eta}\mathbf{F}_j^{(4)}, \tag{5.25}$$

where compared to (5.1) a single entry j is set as $b_j = 1$ and all other entries in $\mathbf{b}_1$ are zero. The radiated fields are calculated numerically for each excited mode individually. Thus, in total, J simulations need to be performed. In the presented implementation, this is done using the FDTD solver of EMPIRE XPU [54]. In the simulations, the fields on the enclosing surfaces Ξ_2 around each receiving antenna location are recorded, ref. Fig. 5.4 (bottom right). These fields on Ξ_2 represent the incoming waves at the receiver and thus are decomposed into vectors of incoming wave coefficients $\mathbf{a}_2'$. Because a single mode b_j' is excited in each simulation, each vector $\mathbf{a}_2'$ directly forms a column of the channel matrix $\mathbf{M}_{21}'$. In Fig. 5.4 (center), this is outlined by the arrows connecting a single excited outgoing spherical wave b_j' with each incoming mode a_j' at the receiver.

5.4.2 Antenna Optimization

To find optimal antennas as discussed in Chapter 5.3, additionally the channel's spherical mode reflection property in form of $\mathbf{M}_{11}$ in (5.21) needs to be determined. For this purpose, the total fields on the surface Ξ_1 enclosing the antenna resulting from the simulation are also recorded when the individual modes b_j' are excited and decomposed into $\hat{\mathbf{b}}_1$, ref. Fig. 5.2(b). Assembling all column vectors $\hat{\mathbf{b}}_1$ in the matrix $\hat{\mathbf{B}}_1$, the channel reflection matrix can be calculated as:

$$\mathbf{M}_{11} = \mathbf{I} - \hat{\mathbf{B}}_1^{-1}. \tag{5.26}$$

Due to the small antenna integration volume with the largest dimension of about $d = 0.5\lambda$ in the example application, ref. Fig. 5.3, it can be assumed that the antenna is mainly represented by the first six spherical wave modes

(corresponding to small electric and magnetic dipoles). Hence, the channel matrices $\mathbf{M}'_{21}$ for the antenna optimization are also calculated for the first six spherical wave modes only. The utilized near-field source has an edge length of 16 mm, with its center coinciding with the center of the antenna integration space. In Fig. 5.5, one of the calculated channel matrices is shown as an example. For the antenna optimization, the columns with the largest norm (the highest power at the receiver) are now sought. At this point, it is not yet possible to define clear antenna design goals (e.g. for exciting a selected mode), as obviously multiple solutions exist and multiple modes are to be combined eventually. However, based on the channel matrices $\mathbf{M}'_{21}$, optimal properties for the transmitting antenna can be calculated using the optimization method derived in Chapter 5.3.

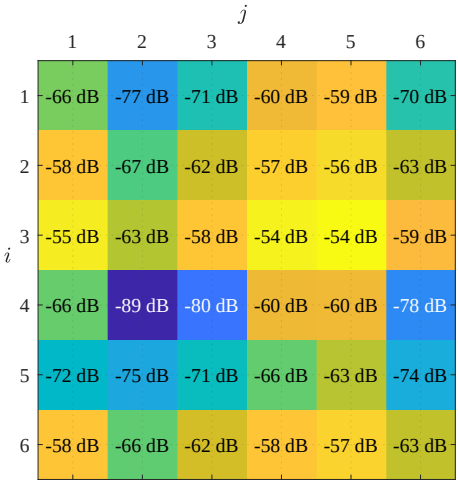

Figure 5.5: Magnitudes of the entries of a transmission matrix $\mathbf{M}'_{21}$ (example: receiver FL with phantom M/c, ref. Fig. 5.3). The columns j correspond to the excitation of $\mathbf{b}'$ at the transmitter, rows i to the incoming waves $\mathbf{a}'$ at the receiver [Ber+22]

In general, the optimal solution $\mathbf{b}'_{\text{opt}}$ may consist of an arbitrary combination of excited spherical waves. To realize such a general antenna, both TE and TM modes would have to be excited simultaneously by that antenna. This requires so-called Huygens antennas, whose design is very challenging [68]. Therefore, the solution space is restricted and the optimization is performed individually for either only TE or TM Modes.

The optimal spherical wave excitation $\mathbf{b}'_{\text{opt}}$ is calculated individually for all channel matrices $\mathbf{M}'_{21}$ of the evaluated example as depicted in Fig. 5.3. A global optimum $\mathbf{b}'_{\text{opt,g}}$ can then be defined by the superposition of the individual optimal antenna properties:

$$\mathbf{b}'_{\text{opt,g}} = \sum_{k=1}^{60} p_k \mathbf{b}'_{\text{opt},k}, \tag{5.27}$$

whereby k is the index describing the scenarios, ref. Fig. 5.3, p_k is the weighting (e.g. based on the likelihood) of the k^{th} scenario and $\mathbf{b}_{\text{opt},k\prime}$ is the optimum in the individual scenario. In this case, it is assumed that all scenarios are equally weighted ($p_k = 1/60$). In the chosen example, the optimum calculated for TE-mode excitation gives a higher power of incoming waves at the receivers on average. Therefore, only this optimum is considered in the following.

Fig. 5.6(a) depicts the global optimum for TE-mode excitation $\mathbf{b}'_{\text{opt,TE}}$ which is calculated using (5.27). From the first six SWF as depicted in Fig. 5.6(a), the weighting coefficients $\mathbf{g}_{\text{opt,TE}}$ for equivalent dipoles can also be obtained [63] as depicted in Fig. 5.6(b). As can be seen, for the chosen example, the solution of the optimization using only TE modes can be approximated very well by a single x-directed magnetic dipole, which can be used subsequently as an antenna design guideline. However, the design guideline for the optimal antenna cannot always be expected to be as clear as in the chosen example. In those cases, the on-body gain pattern for the optimal excitation can be calculated using (5.22) - (5.24) and (4.4).

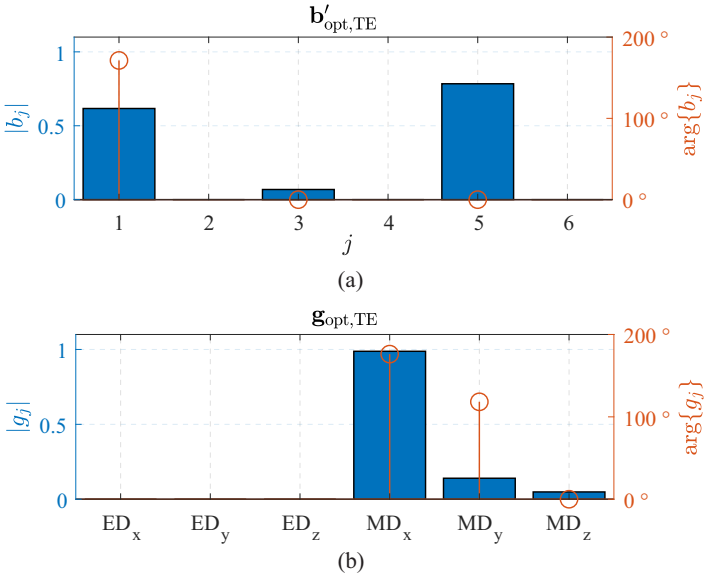

Figure 5.6: Optimized spherical wave excitation for the example application (weighted superposition, ref. (5.27)): (a) optimal TE-mode excitation; (b) associated weighting coefficients for small magnetic (MD) and electric (ED) dipoles [Ber+22].

5.4.3 Antenna Design

Based on the calculated optimal excitation for the example application, the antenna can be designed. An antenna that realizes an x-directed magnetic current required for the optimal antenna, is depicted in Fig. 5.7(a). It consists of two parallel metal plates (realized on an FR4 substrate) with a length of approximately 0.5λ, which are connected to each other through multiple pins at both ends. The excited E-field distribution with its maximum at the center of the antenna in x-direction is outlined in the xz-cut of the antenna structure in Fig. 5.7(b). The radiated fields can equivalently be represented by an x-directed magnetic half-wave dipole of magnetic currents $\mathbf{M}$ which are also outlined in Fig. 5.7(b).

The relationship to the optimal antenna is particularly evident in the on-body gain pattern as depicted in Fig. 5.8. For the magnetic dipole antenna structure, the on-body gain is calculated directly from the simulated antenna's near field as described in [BM211]. The on-body gain for the optimal antenna is calculated by (5.22)-(5.24) and (4.4). As can be seen, the chosen magnetic dipole antenna has an on-body gain pattern very similar to the optimum case. However, due to losses of the antenna structure, the gain is reduced by approximately 2 dB compared to the theoretical optimum.

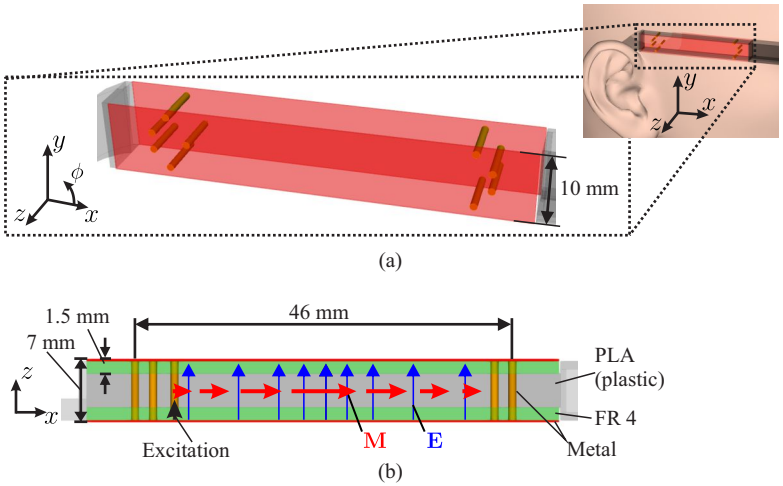

Figure 5.7: Magnetic dipole antenna design for example eyewear application: (a) Antenna structure (b) xz-cut of the designed antenna with excited **E**-fields and equivalent magnetic currents **M**. [Ber+22]

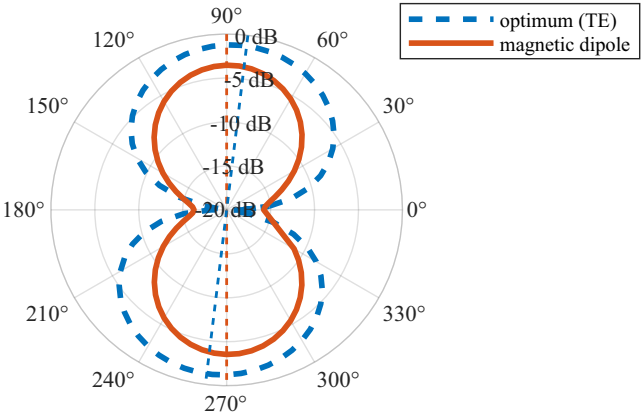

Figure 5.8: On-body gain [BM211] (xy-plane) of the optimal TE mode excitation (ref. Fig. 5.6), compared to magnetic dipole design (ref. Fig. 5.7). The dashed lines mark the axes with maximum gain. [Ber+22]

5.4.4 Antenna Channel Embedding

To evaluate the behavior of the chosen antenna design inside the different SWF channel models, first, the antenna's near field is extracted from a simulation as depicted in Fig. 5.9. Secondly, the antenna's radiated fields are decomposed into $\mathbf{b}'$. In the evaluated example, the field monitor Ξ surrounding the antenna, respectively the near-field source in the channel simulation, has an edge length of 62 mm. To find a sufficient truncation for the number of modes J utilized for modeling the designed antenna, the convergence of the decomposition can be checked based on the norm $\|\mathbf{b}'\|_2$ for different truncation numbers.

As depicted in Fig. 5.10, the power of the excitation $\|\mathbf{b}'\|_2$ converges to a limit with increasing J. Since the exact value of this limit is not known[16], the SWF decomposition is performed step-wise with an increasing mode truncation number J.[17]

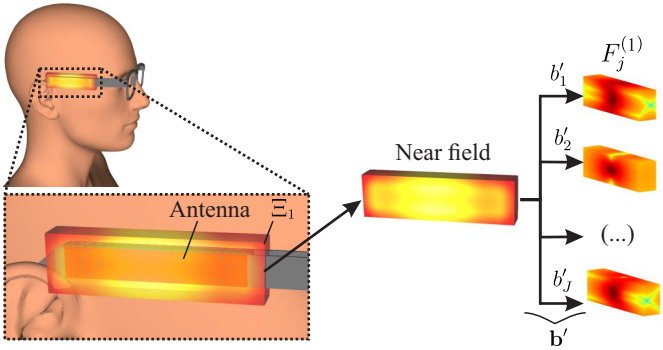

Figure 5.9: SWF antenna modeling: The near field of the antenna is first extracted from a simulation and the fields are then decomposed using (5.12) [Ber+22]

[16] For the SWF mode truncation see also Appendix E.

[17] It makes sense to use complete sets of a certain grade of SWF, e.g. $J = 6$ for dipole modes only and $J = 16$ to additionally include all quadrupole modes, etc., ref. [63].

With every step n for increasing J the relative difference of $\|\mathbf{b}'\|_2$ with the previous step $(n-1)$ is evaluated:

$$\Delta\|\mathbf{b}'\|_2 = \frac{\|\mathbf{b}'_n\|_2 - \|\mathbf{b}'_{n-1}\|_2}{\|\mathbf{b}'_n\|_2}. \tag{5.28}$$

Thus, this quantity approaches zero when convergence is achieved. Evaluating the convergence with the designed magnetic dipole antenna in Fig. 5.10, it can be concluded that as expected the antenna mainly excites SWF modes up to $J = 6$. However, at the next higher number of $J = 16$ the difference is still about $\Delta\|\mathbf{b}'\|_2 \approx 20\,\%$. A possible reason for this is that the phase center of the antenna is not congruent with the origin of the SWF decomposition [63]. Therefore, $J = 30$ is used for the embedding of the antennas in the following.

Finally, the antenna's transmission vector $\mathbf{T}'$ is calculated from $\mathbf{b}'$ according to (5.11) by normalizing it to the accepted power P_a, which is readily available from the numerical simulation of the antenna conducted for calculating the near field as depicted in Fig. 5.9. The monopole antenna, which is used at the receiver side, is characterized equivalently to calculate $\mathbf{R}'$. As mentioned before, the receiving

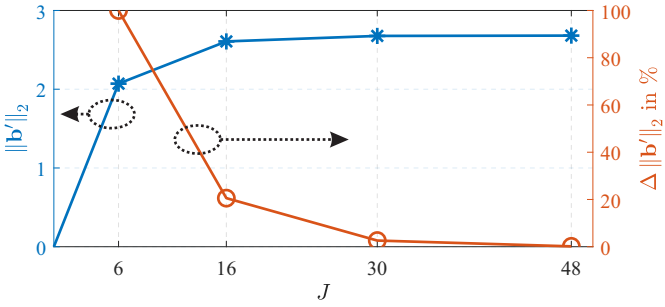

Figure 5.10: Convergence of the SWF antenna decomposition in dependence of mode truncation of the magnetic dipole antenna [Ber+22]

antenna (e.g. integrated inside a smartphone) cannot be adjusted concerning the chosen example application and is thus not evaluated in the analysis.

With all parameters in (5.16) determined, the transmission coefficient S_{21} can be calculated with the designed antenna embedded into the different channels to evaluate the antenna's performance with regard to posing. In Fig. 5.11, the results calculated for the antenna embedded into all considered channels are visualized. The results of the magnitude of the transmission coefficient to the four receiver locations (FL-BR, ref. Fig. 5.3) are depicted in separate plots. Each of the four plots in Fig. 5.11 depicts the transmission coefficient to one of the receivers in dependency of the body pose (ll-rr, ref. Fig 5.3). With regard to varying anatomy, the average of the results with the three different sized phantoms (ref. Fig. 5.3) is considered in Fig. 5.11. The illustrated results reveal that the average transmission coefficient varies by up to 30 dB due to different body poses considered in the evaluation. At the receivers located in front of the torso (FL, FR), the highest magnitudes of the transmission coefficient are observed in the pose ll with the head turned all the way to the left so that the antenna integrated into the right glasses temple is facing to the front of the torso. Conversely, in the pose rr, the transmitter and receiver are on different sides of the body, hence their transmission coefficients are the lowest. With the receivers on the backside (BL, BR), this behavior is reversed.

To validate the results obtained from the SWF modeling, in Fig. 5.11, the transmission coefficient obtained from a conventional FDTD simulation of the whole system for each scenario is depicted as well. As can be seen, only marginal deviations can be observed between the FDTD results and the SWF modeling approach. Additionally, the results calculated for the optimal TE mode excitation, ref. Sec. 5.4.2, are depicted. The very similar slopes of the pose-dependent transmission coefficients show the close relationship of the designed magnetic dipole antenna to the optimal TE mode excitation. Only at the receiver position BR, significant deviations of the slope with the designed antenna compared to the

theoretical optimum can be observed. This can be attributed to the fact that the radiation pattern of the optimum antenna is slightly tilted compared to the straight vertical orientation of the designed magnetic dipole antenna, ref. Fig 5.8. The influence of this tilt becomes more obvious if the optimal radiation pattern is explicitly calculated for the link with receiver BR (tilt of about 30°, not shown), rather than the overall optimum as depicted in Fig. 5.8.

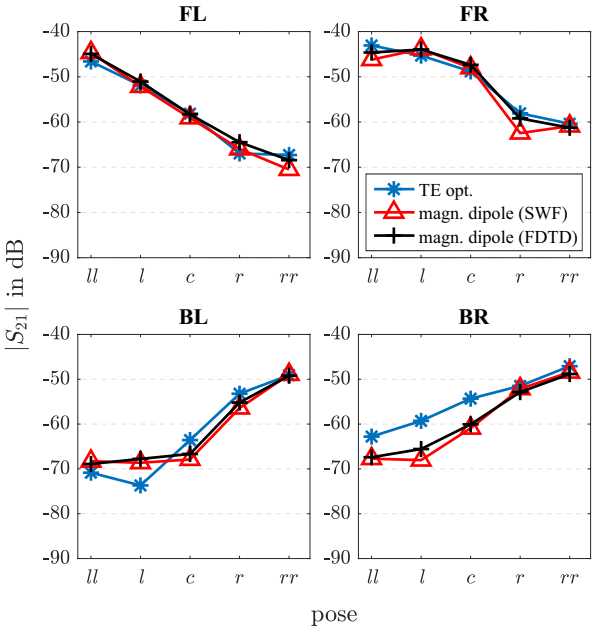

Figure 5.11: Transmission coefficient $|S_{21}|$ (average of different anatomies) to different receivers (FL-BR) in dependency of the body pose (*ll*-*rr*) with magnetic dipole antenna compared to theoretical optimal TE-mode antenna [Ber+22]

5.5 Antenna Performance Evaluation

In the following, on the one hand, the implemented approach of SWF antennas and channel modeling for the selected example is further validated in comparison to a measurement campaign. On the other hand, it is shown how the system performance with different antennas can be predicted efficiently using the SWF modelling (without measurements) by embedding an antenna candidate into many different channel scenarios. Therefore, two additional antenna designs are evaluated for the eye-wear example application as described above. In addition to the designed magnetic dipole antenna (ref. Fig. 5.7) based on the SWF antenna optimization, a standard folded half-wave dipole antenna as well as an inverted-F antenna (IFA) as depicted in Fig. 5.12 are utilized.

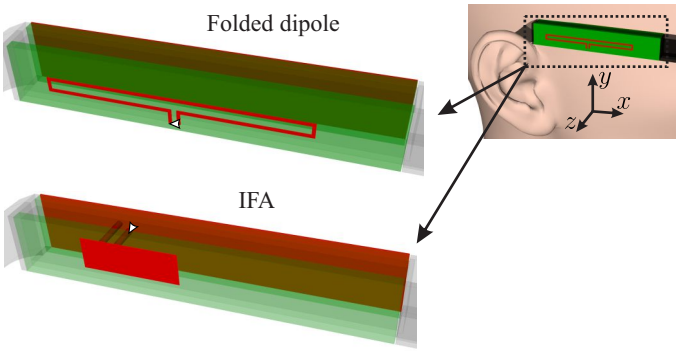

Figure 5.12: Additional antenna designs for evaluation of the SWF modeling method [Ber+22]

5.5.1 Measurement Setup

Physical prototypes of all three antennas were realized as depicted in Fig. 5.13(a) and integrated along with a battery-powered Bluetooth transmitter circuit (Espressif ESP32-PICO-D4) into the glasses temples. Likewise, the four receivers are equipped with active Bluetooth transceivers. The transmission coefficients are estimated over-the-air (OTA) with the Bluetooth received signal strength indicator (RSSI). This way, cable effects are avoided. Measurements are performed with five human test subjects (all male, body heights: $h \in [172; 176; 178; 189; 192]$ cm) inside an anechoic chamber as depicted in Fig. 5.13(b). With each test subject, multiple measurements in the five different body poses as defined in Fig. 5.3 are taken. To compensate for uncertainties in the measurements with regard to the transmitting power of the transceivers and possible antenna mismatching, a calibration factor is introduced for each antenna. It is calculated as the average magnitude of the transmission coefficient obtained from the numerical simulations divided by the average of all measured RSSI values.

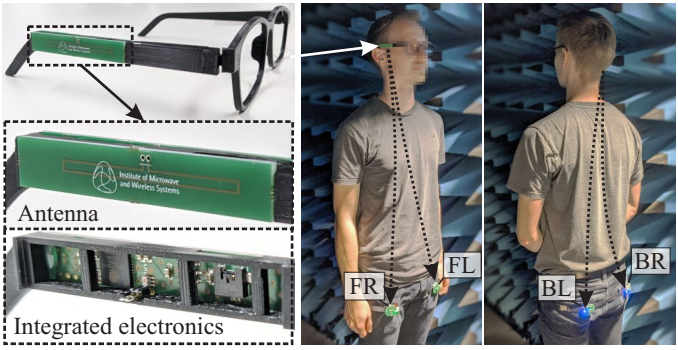

(a) (b)

Figure 5.13: (a) Physical prototype of the evaluated antennas; (b) Measurements with human test subjects inside an anechoic chamber [Ber+22]

As illustrated in Fig. 5.14, the measured and calibrated transmission coefficients for each scenario are evaluated statistically. The average transmission coefficient (depicted as bold markers) is calculated depending on the pose at each receiver by combining the results of all five test subjects. The results in Fig. 5.14 also reveal that presumably due to fading, the observed transmission coefficient in individual measurements is partly (10 - 20) dB below the calculated average.

5.5.2 KPI: Connection Loss Probability

To further evaluate the antenna performance, the probability of connection losses is identified as a simplified key performance indicator (KPI) for the considered application. Assuming a common value for the maximum dynamic range of 90 dB of the RF link (receiver sensitivity of -90 dBm and transmit power of 0 dBm), and the measured deviation of individual values from the average of up to 20 dB, an average transmission coefficient $|S_{21}| < -70\,\text{dB}$ can be assumed to potentially cause connection losses. Accordingly, assuming that all poses are equally likely, the KPI can be calculated as the percentage of poses with $|S_{21}| < -70\,\text{dB}$. In Fig. 5.14, this lower limit for the average transmission coefficient is outlined by a dashed line. If the results with the two different antennas as depicted in Fig. 5.14 are evaluated in this regard, pose rr represents such a case in which with the folded dipole antenna the average transmission coefficient drops below the -70 dB limit and also individual measured values are very close to the sensitivity limit. However, with the magnetic dipole antenna, which is designed based on the optimization, the average is increased by about 10 dB, whereby the connection can be assumed to remain stable even in the critical pose rr.

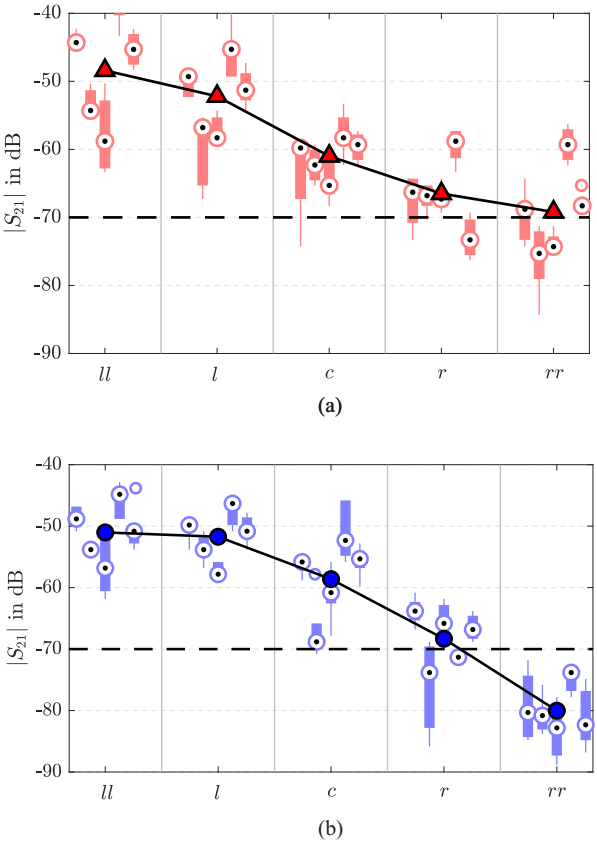

Figure 5.14: Distribution of the measured transmission coefficients at receiver FL: (a) Magnetic dipole; (b) Folded dipole. At each body pose (ll-rr), five boxplots depict the statistical distribution of the results of the individual measurements with the different test subjects. The calculated average transmission coefficient per pose is depicted by the bold markers. The dashed line outlines the limit for the calculation of the KPI. [Ber+22]

5.5.3 Evaluation

Fig. 5.15 compares the measured average transmission coefficients of all three antennas considered. As can be seen, significant differences between the three antennas exist, even if the general behavior concerning the posing is similar. By calculating the SWF transmission vector $\mathbf{T}'$ also for the additional two antennas from their near field, these can also be embedded into the beforehand calculated channel matrices. The resulting average transmission coefficients derived using the SWF modeling are depicted in Fig. 5.16. As can be seen, the main trends compared to those from the measurement in Fig. 5.15 are clearly the same. With the magnetic dipole antenna, the highest average transmission coefficients are found and thus the optimization goal is fulfilled. Depending on whether SWF modeling or measurement is considered, there is only one pose with a risk of connection losses.

The folded dipole antenna shows the worst performance in the calculated and measured transmission coefficients. Interestingly, this antenna also shows a drop in the transmission factor to the receiver FR when the transmitter and receiver are on the same side of the body (pose ll). This behavior equally occurs in the measurement and the SWF modeling. In both measurement and SWF modeling, there are four poses with potential signal losses with the folded dipole. The transmission coefficients with the IFA are noticeably low for the receivers at the front (FL, FR), whereas at the back (BL, BR) it partly even outperforms the magnetic dipole antenna. Related to poses with potential signal losses, three cases are counted in the results of the measurement and SWF modeling with the IFA, while one case is counted at different positions in SWF modeling and measurement.

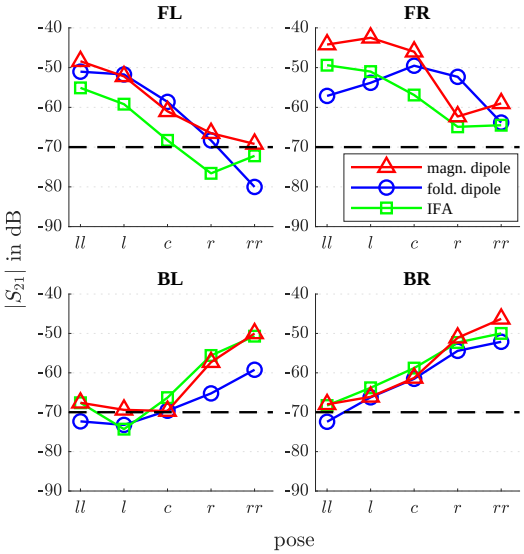

Figure 5.15: Measurement: average transmission coefficient in dependency of the body pose. The dashed line outlines the limit for the calculation of the KPI. [Ber+22]

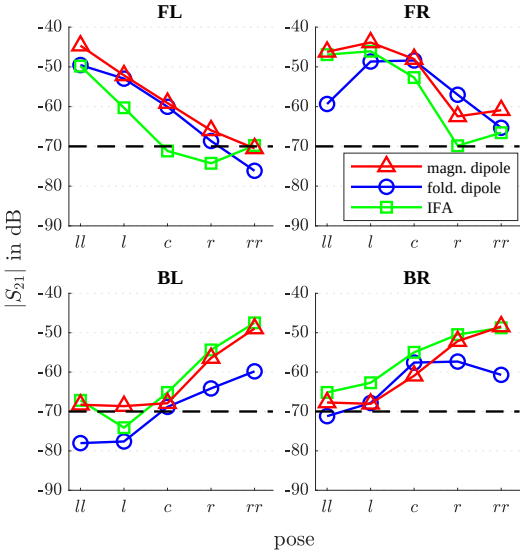

Figure 5.16: SWF modeling: average transmission coefficient in dependency of the body pose. The dashed line outlines the limit for the calculation of the KPI. [Ber+22]

Table 5.1: Antenna Performance Evaluation [Ber+22]

	magnetic dipole	folded dipole	IFA
KPI (SWF)[1]	5% (1)	20% (4)	15% (3)
KPI (meas.)[1]	0% (0)	20% (4)	15% (3)

[1] The KPI is calculated as the percentage of poses with potential connection losses, lower is better. The value in brackets indicates the absolute number of cases.

In Tab. 5.1, the results of the calculated KPIs are summarized for all three antennas. For the calculation of the relative probability of connection losses, the total number of 20 equally likely poses and receiver locations is considered here. The comparison by means of the more complex analysis of the curves in Fig. 5.15 and Fig. 5.16 can thus be translated into a quantitative factor. Its calculation with SWF modeling purely based on numerical near-field data of the evaluated antennas is very fast compared to time-consuming measurements or conventional scenario-specific simulations of the entire system, with the obtained results showing very good agreement.

5.6 Discussion

Compared to the modeling using the on-body antenna parameters developed in Chapter 4, with the modeling based on SWF as derived in this chapter, channels of any complexity can be described since the method could be implemented numerically. The numerical calculation with the SWF modeling also includes the propagation channel, which could only be determined analytically in a costly process when modeling with the on-body antenna parameters. The computational effort to determine the channel models with the SWF modeling is also not negligible as simulations have to be performed for each mode to be considered. However, the simulations can be automated to a large extent. Thus, as shown with the example

above, it is also possible to perform modeling for quasi-dynamic on-body channels. The body's movement and, accordingly, the varying propagation channel can be modeled frame-wise. Also, the influence of all other factors like varying body sizes or varying antenna positions can be calculated exemplary as it is demonstrated with the example evaluated. Once the channel models have been determined, the embedding process for the antennas employing simple matrix multiplication is very efficient. Subsequently, as shown, a statistical evaluation of the antenna performance in different channels is easily possible.

The SWF modeling has no limitations for the applications due to its theoretical basis. However, for efficient numerical evaluation, certain assumptions have been made, which must also be considered when using this method to obtain correct results. To solve the near-field coupling problem between the antenna and the body tissue, respectively, the channel, it was assumed that the antenna scattering matrix corresponds to the unity matrix in the alternative arrangement with the antenna replaced by equivalent currents. This assumption is only valid if the interior of the enveloping surface Ξ used for the equivalence principle corresponds to free space when the antenna is replaced, and no reflections occur at its boundary surface. Therefore, implanted antennas cannot be modeled with this method so far. Furthermore, the numerical solution always is an approximation since the SWF expansion theoretically represents an infinite series. As shown, real problems can always be described sufficiently accurately with a finite number of modes. However, an estimate of this number depends on many factors, in particular on the exact numerical implementation, such as the size and spatial position of the near-field reference surfaces and antennas considered. Thus, an adaptive convergence check has been implemented as described in Chapter 5.4.4.

In addition, when exciting the individual SWFs for the channel modeling, it must be taken into account that large spatial field gradients are generated at higher modes, which must be considered to avoid excessive numerical errors. This property should also be taken into account when choosing the reference surface Ξ en-

closing the antenna. In order to calculate as few modes as possible, it is desirable to place the antenna as centrally as possible within Ξ, respectively the coordinate system used.[18] In contrast, the field gradient on the surface increases with decreasing surface when the individual modes are excited. Hence, other than with the implementation of the on-body antenna parameters, the choice of the reference surface Ξ is always a trade-off and should be considered in the modeling.

Another significant advantage of the SWF modeling is that, based on a calculated channel model, the characteristics of the optimum antenna can be calculated that lead to the largest possible magnitude of the transmission parameter. However, this information for the optimum antenna is available in an unintuitive form as a vector with complex coefficients when modeling with SWF. Similarly, the channel models consist of complex-valued matrices, so that little information about the physical transmission behavior can be obtained. On the other hand, the antenna characterization with both the SWF modeling as well as with the on-body antenna parameters is based on the near-field of the antenna in the presence of the surrounding body tissue. Accordingly, as shown, a combination of both developed methods could be implemented so that the antenna characteristics can also be analyzed in the form of an intuitive radiation pattern when using the SWF method.

[18] This leads to the smallest possible minimum sphere, see Appendix E.

Chapter 6
Conclusion

The objective of this research is to develop antenna de-embedding methods for on-body propagation that enable an educated antenna design for such applications. As the problem analysis revealed, the standard antenna characterization methods are not applicable for the on-body domain due to the near-field interaction between the antenna and the body tissue as part of the propagation channel. Furthermore, existing approaches in literature for solving this issue as discussed in Chapter 2 are either specific for certain geometries, antennas, etc., or lack interpretability, especially with regard to optimized antenna designs. Hence, this work aims to develop universal methods that can be readily applied to antenna optimization. For this purpose, two different approaches have been developed.

First, in Chapter 3, an on-body propagation model was derived. Therefore, the body is approximated as an infinite tissue half-space. Due to this very strong simplification, the derived model by itself can only be used for practical problems to a very limited extent. On the other hand, the derived solutions allow a good understanding of the occurring propagation mechanisms. Also, based on the simplified solutions, an on-body far-field and associated boundaries could be derived. The on-body antenna parameters as derived in Chapter 4 are advantageous as they allow de-embedded characterization of the antenna itself and eliminate

any influence of the subsequent application. The specific quantification of an antenna's suitability for on-body propagation enables an objective evaluation of the antennas and the assessment of dedicated on-body antenna design specifications. Due to the developed measurement procedures, e.g., with the antenna range as designed in Chapter 4.3, high practical relevance of the developed methods is achieved. As shown by the examples evaluated, the on-body antenna parameters and the determined transmission equation, analogous to the Friis equation in free space, can also be used to model the entire wireless system. In the same way, the antenna can be optimized based on the on-body gain by maximizing the on-body gain in the direction of the most relevant propagation path. However, the difficulty here lies in the determination of the channel model. The determination is only possible via analytical methods for clear separation from the antenna. In this case, the complex, variable body geometries and the complex interaction of the fields and the body tissue lead to a high modeling effort. Examples from the literature show that such modeling is possible in principle, but it is costly and not universally possible for any application as described above.

At this point, the advantage of the second method developed becomes apparent. With the modeling based on SWF as derived in Chapter 5, channels of any complexity can be described since the method could be implemented numerically. Thus, it is also possible to perform frame-wise modeling of the body's movement and all other influencing factors like varying body sizes or varying antenna positions. In contrast to previous methods, where the entire system had to be recalculated for each antenna to be investigated, the major numerical effort with SWF modeling is incurred only once for the determination of the channel models. Any antennas, or iterations during an antenna design process, can then be embedded into the channel model using a simple matrix multiplication, which, compared to standard methods, also correctly reproduces the near-field coupling. For the characterization of the antennas, the near-field of the antenna in the presence of the body tissue is used as before for the calculation of the on-body antenna

parameters. As has been shown, SWF modeling is also very well suited for antenna optimization. Based on the channel model, the optimal characteristics of the antennas for minimizing the path loss can be determined. To make this information intuitively usable for the antenna design and to compare real antenna designs with the theoretical optimum, a link to the on-body antenna parameters was established in Chapter 5, which allows an evaluation of the on-body pattern also on the basis of the SWF coefficients.

With the combination of the two methods developed, the objectives set for this work can be well achieved, as shown by the results of the different examples studied. Compared to previous work, this work provides more general methods, with limitations tolerable for most of today's applications. In future work, the developed on-body antenna parameters could be used for standardized antenna characterization methods and test procedures for wearable and implantable antennas since, compared to previous approaches, a clear definition has been found that also allows good measurability of the parameters. The SWF modeling efficiently enables a detailed antenna performance evaluation, which significantly simplifies antenna optimization, especially for on-body systems with many influencing factors. A future automated implementation using standard EM-modeling software would promote the use of the method for practical applications. Also, it is desirable to broaden the applicability of the SWF modeling method concerning implanted antennas.

This work was initiated within the framework of the project "Models for the optimized development of antennas worn on the body and integrated into implants," which was funded by the German Research Foundation (DFG). In addition, a successful industrial cooperation has already resulted in a first practical application of the methods and the development of a patented antenna design. Further transfer of the developed methods for industrial applications is therefore desirable.

Bibliography

For the author's publications (alphabetic citation style), see the list at page XV.

[1] P. S. Hall and Y. Hao, *Antennas and Propagation for Body-Centric Wireless Communications, Second Edition*. Artech House, 2012.

[2] C. A. Balanis, *Antenna Theory: Analysis and Design*. USA: Wiley, 2016.

[3] "IEEE Standard for Local and metropolitan area networks - Part 15.6: Wireless Body Area Networks", *IEEE Std 802.15.6-2012*, Feb. 2012. DOI: 10.1109/IEEESTD.2012.6161600.

[4] J. A. Afonso, A. J. F. Maio, and R. Simoes, "Performance Evaluation of Bluetooth Low Energy for High Data Rate Body Area Networks", *Wireless Personal Communications*, vol. 90, no. 1, pp. 121–141, Sep. 2016. DOI: 10.1007/s11277-016-3335-4.

[5] Medtronic, *Cardiac Device Features - BlueSync Technology*, en, [Online], Mar. 2021. [Online]. Available: https://www.medtronic.com/us-en/healthcare-professionals/therapies-procedures/cardiac-rhythm/cardiac-device-features/bluesync-technology.html (visited on 03/08/2021).

[6] "IEEE Standard Test Procedures for Antennas", *ANSI/IEEE Std 149-1979*, 1979. DOI: 10.1109/IEEESTD.1979.120310.

[7] "Test Plan for Wireless Device Over-the-Air Performance", CTIA, Tech. Rep. Version 3.8.2, Apr. 2019.

[8] "Guidelines for Limiting Exposure to Electromagnetic Fields (100 kHz to 300 GHz)", *Health Physics*, vol. 118, no. 5, pp. 483–524, 2020. DOI: 10.1097/HP.0000000000001210.

[9] "IEC/IEEE International Standard - Measurement procedure for the assessment of specific absorption rate of human exposure to radio frequency fields from hand-held and body-mounted wireless communication devices – Part 1528: Human models, instrumentation, and procedures (Frequency range of 4 MHz to 10 GHz)", IEC/IEEE, Tech. Rep., 2020. DOI: 10.1109/IEEESTD.2020.9231298.

[10] H. Friis, "A Note on a Simple Transmission Formula", *Proceedings of the IRE*, vol. 34, no. 5, pp. 254–256, 1946. DOI: 10.1109/JRPROC.1946.234568.

[11] "IEEE Standard for Definitions of Terms for Antennas", *IEEE Std 145-2013 (Revision of IEEE Std 145-1993)*, 2014.

[12] S. Salous, *Radio Propagation Measurement and Channel Modelling*, en. John Wiley & Sons, 2013.

[13] M. Gallo, P. S. Hall, Q. Bai, Y. I. Nechayev, C. C. Constantinou, and M. Bozzetti, "Simulation and measurement of dynamic on-body communication channels", *IEEE Transactions on Antennas and Propagation*, vol. 59, no. 2, pp. 623–630, 2011. DOI: 10.1109/TAP.2010.2093498.

[14] J.-i. Naganawa, K. Wangchuk, M. Kim, T. Aoyagi, and J.-i. Takada, "Simulation-Based Scenario-Specific Channel Modeling for WBAN Cooperative Transmission Schemes", *IEEE Journal of Biomedical and Health Informatics*, vol. 19, no. 2, pp. 559–570, Mar. 2015. DOI: 10.1109/JBHI.2014.2326424.

[15] T. Uusitupa and T. Aoyagi, "Analysis of dynamic on-body communication channels for various movements and polarization schemes at 2.45 GHz", *IEEE Transactions on Antennas and Propagation*, vol. 61, no. 12, pp. 6168–6179, Dec. 2013. DOI: 10.1109/TAP.2013.2281369.

[16] Q. Wang, T. Tayamachi, I. Kimura, and J. Wang, "An on-body channel model for UWB body area communications for various postures", *IEEE Transactions on Antennas and Propagation*, vol. 57, no. 4, pp. 991–998, Apr. 2009. DOI: 10.1109/TAP.2009.2014526.

[17] Q. H. Abbasi, A. Sani, A. Alomainy, and Y. Hao, "Experimental Characterization and Statistical Analysis of the Pseudo-Dynamic Ultrawideband On-Body Radio Channel", *IEEE Antennas and Wireless Propagation Letters*, vol. 10, pp. 748–751, 2011. DOI: 10.1109/LAWP.2011.2162811.

[18] S. Swaisaenyakorn, S. W. Kelly, and J. C. Batchelor, "A Study of Factors Affecting Wrist Channel Characteristics for Walking Postures Using Motion Capture", *IEEE Transactions on Antennas and Propagation*, vol. 62, no. 4, pp. 2231–2237, Apr. 2014. DOI: 10.1109/TAP.2014.2300859.

[19] P. Yang, Y. Shao, P. Wang, and J. Zhang, "Analysis of Polarization Characteristics for Dynamic On-body Channel at 28 GHz", in *2021 15th European Conference on Antennas and Propagation (EuCAP)*, Mar. 2021, pp. 1–5. DOI: 10.23919/EuCAP51087.2021.9411145.

[20] T. Kumpuniemi, M. Hämäläinen, K. Y. Yazdandoost, and J. Iinatti, "Human body shadowing effect on dynamic UWB on-body radio channels", *IEEE Antennas and Wireless Propagation Letters*, vol. 16, pp. 1871–1874, 2017. DOI: 10.1109/LAWP.2017.2656246.

[21] K. Ali, A. Brizzi, S. Lee, G. Yang, A. Alomainy, and Y. Hao, "Quantitative analysis of the subject-specific on-body propagation channel based on statistically created models", *IEEE Antennas and Wireless Propagation Letters*, vol. 14, pp. 398–401, 2015. DOI: 10.1109/LAWP.2014.2362412.

[22] A. Lea, P. Hui, J. Ollikainen, and R. G. Vaughan, "Propagation Between On-Body Antennas", *IEEE Transactions on Antennas and Propagation*, vol. 57, no. 11, pp. 3619–3627, Nov. 2009. DOI: 10.1109/TAP.2009.2031917.

[23] Q. Zhang, J. Sarrazin, M. Casaletti, P. De Doncker, and A. Benlarbi-Delaï, "Assessment of on-body skin-confined propagation for body area network", *IEEE Antennas and Wireless Propagation Letters*, vol. 16, pp. 2610–2613, 2017. DOI: 10.1109/LAWP.2017.2735631.

[24] K. Ali, F. Keshmiri, A. Brizzi, Y. Hao, and C. Craeye, "Body area networks at radio frequencies: Creeping waves and antenna analysis", *Comptes Rendus Physique*, Radio science for connecting humans with information systems / L'homme connecté, vol. 16, no. 9, pp. 789–801, 2015. DOI: 10.1016/j.crhy.2015.10.005.

[25] M. Grimm and D. Manteuffel, "Norton surface waves in the scope of body area networks", *IEEE Transactions on Antennas and Propagation*, vol. 62, no. 5, pp. 2616–2623, May 2014. DOI: 10.1109/TAP.2014.2307347.

[26] N. Chahat, G. Valerio, M. Zhadobov, and R. Sauleau, "On-Body Propagation at 60 GHz", *IEEE Transactions on Antennas and Propagation*, vol. 61, no. 4, pp. 1876–1888, Apr. 2013. DOI: 10.1109/TAP.2013.2242034.

[27] A. Fort, F. Keshmiri, G. R. Crusats, C. Craeye, and C. Oestges, "A body area propagation model derived from fundamental principles: Analytical analysis and comparison with measurements", *IEEE Transactions on Antennas and Propagation*, vol. 58, no. 2, pp. 503–514, 2009. DOI: 10.1109/TAP.2009.2025786.

[28] T. Alves, B. Poussot, and J. Laheurte, "Analytical propagation modeling of BAN channels based on the creeping-wave theory", *IEEE Transactions on Antennas and Propagation*, vol. 59, no. 4, pp. 1269–1274, Apr. 2011. DOI: 10.1109/TAP.2010.2096184.

[29] F. Keshmiri and C. Craeye, "Moment-method analysis of normal-to-body antennas using a green's function approach", *IEEE Transactions on Antennas and Propagation*, vol. 60, no. 9, pp. 4259–4270, Sep. 2012. DOI: 10.1109/TAP.2012.2207053.

[30] A. M. Eid and J. W. Wallace, "Accurate Modeling of Body Area Network Channels Using Surface-Based Method of Moments", *IEEE Transactions on Antennas and Propagation*, vol. 59, no. 8, pp. 3022–3030, Aug. 2011. DOI: 10.1109/TAP.2011.2158971.

[31] Z. Ma, J. Sarrazin, L. Petrillo, T. Mavridis, P. D. Doncker, and A. Benlarbi-Delaï, "Antenna radiation characterization for on-body communication channel using creeping wave theory", in *2015 9th European Conference on Antennas and Propagation (EuCAP)*, Apr. 2015, pp. 1–4.

[32] D. P. Chrissoulidis and J. Laheurte, "Dyadic green's function of a non-spherical model of the human torso", *IEEE Transactions on Microwave Theory and Techniques*, vol. 62, no. 6, pp. 1265–1274, Jun. 2014. DOI: 10.1109/TMTT.2014.2318021.

[33] D. Ma and W. X. Zhang, "Analytic Propagation Model for Wireless Body-Area Networks", *IEEE Transactions on Antennas and Propagation*, vol. 59, no. 12, pp. 4749–4756, Dec. 2011. DOI: 10.1109/TAP.2011.2165473.

[34] N. P. B. Kammersgaard, S. H. Kvist, J. Thaysen, and K. B. Jakobsen, "Ear-to-ear propagation model based on geometrical theory of diffraction", *IEEE Transactions on Antennas and Propagation*, vol. 67, no. 2, pp. 1153–1160, Feb. 2019. DOI: 10.1109/TAP.2018.2882587.

[35] R. Chandra and A. J. Johansson, "A Link Loss Model for the On-Body Propagation Channel for Binaural Hearing Aids", *IEEE Transactions on Antennas and Propagation*, vol. 61, no. 12, pp. 6180–6190, Dec. 2013. DOI: 10.1109/TAP.2013.2283270.

[36] S. H. Kvist, J. Thaysen, and K. B. Jakobsen, "Ear-to-ear on-body channel model for hearing aid applications", *IEEE Transactions on Antennas and Propagation*, vol. 63, no. 1, pp. 344–352, Jan. 2015. DOI: 10.1109/TAP.2014.2368578.

[37] N. P. B. Kammersgaard, S. H. Kvist, J. Thaysen, and K. B. Jakobsen, "Geometrical theory of diffraction formulation for on-body propagation", *IEEE Transactions on Antennas and Propagation*, vol. 67, no. 2, pp. 1143–1152, Feb. 2019. DOI: 10.1109/TAP.2018.2882596.

[38] S. Kim, J. S. Ho, and A. S. Y. Poon, "Wireless power transfer to miniature implants: Transmitter optimization", *IEEE Trans. Antennas Propag*, vol. 60, no. 10, pp. 4838–4845, 2012. DOI: 10.1109/TAP.2012.2207341.

[39] L. Song and Y. Rahmat-Samii, "An end-to-end implanted brain–machine interface antenna system performance characterizations and development", *IEEE Transactions on Antennas and Propagation*, vol. 65, no. 7, pp. 3399–3408, 2017. DOI: 10.1109/TAP.2017.2700163.

[40] D. U. Agu, M. Leece, J. Alcala-Medel, A. Sahdev, J. Lim, M. Olsen, B. Ngan, Y. Kim, and Y. Li, "Investigation of dominant wave mechanism and optimal antenna excitation for body-centric wireless propagations", *Progress In Electromagnetics Research C*, vol. 104, pp. 1–11, 2020. DOI: 10.2528/PIERC20051605.

[41] S. Dumanli and C. J. Railton, "On-Body Transmission at 5.2 GHz: Simulations Using FDTD With a Time Domain Huygens' Technique", *IEEE Transactions on Antennas and Propagation*, vol. 59, no. 10, pp. 3910–3917, Oct. 2011. DOI: 10.1109/TAP.2011.2163786.

[42] S. Dumanli and C. J. Railton, "Analysis of Coupled Tilted Slot Antennas in FDTD Using a Novel Time Domain Huygens Method With Application to Body Area Networks", *IEEE Transactions on Antennas and Propagation*,

vol. 60, no. 4, pp. 1987–1994, Apr. 2012. DOI: 10.1109/TAP.2012.2186256.

[43] A. Sani, Y. Zhao, Y. Hao, A. Alomainy, and C. Parini, "An Efficient FDTD Algorithm Based on the Equivalence Principle for Analyzing On-body Antenna Performance", *IEEE Transactions on Antennas and Propagation*, vol. 57, no. 4, pp. 1006–1014, Apr. 2009. DOI: 10.1109/TAP.2009.2014581.

[44] M. Grimm and D. Manteuffel, "On-body antenna parameters", *IEEE Transactions on Antennas and Propagation*, vol. 63, no. 12, pp. 5812–5821, Dec. 2015. DOI: 10.1109/TAP.2015.2482499.

[45] J. R. Wait, "The ancient and modern history of EM ground-wave propagation", *IEEE Antennas and Propagation Magazine*, vol. 40, no. 5, pp. 7–24, Oct. 1998. DOI: 10.1109/74.735961.

[46] S. Razafimahatratra, J. Sarrazin, G. Valerio, F. Sarrazin, M. Casaletti, P. d. Doncker, and A. Benlarbi-Delai, "Input impedance of an aperture over a lossy half-space: Application to on-body antenna performance at 60 ghz", en, *Progress In Electromagnetics Research, PIER C*, vol. 83, pp. 161–178, Apr. 2018. (visited on 06/22/2020).

[47] J. Naganawa, J. Takada, T. Aoyagi, and M. Kim, "Antenna Deembedding in WBAN Channel Modeling Using Spherical Wave Functions", *IEEE Transactions on Antennas and Propagation*, vol. 65, no. 3, pp. 1289–1300, Mar. 2017. DOI: 10.1109/TAP.2017.2655006.

[48] R. Barake, A. Harmouch, and M. Kenaan, "Study on the validity of the formalism of norton to describe the propagation of electromagnetic waves on the surface of the body", en, *Journal of Communications Technology and Electronics*, vol. 61, no. 8, pp. 952–956, Aug. 2016. DOI: 10.1134/S1064226916080039.

[49] K. A. Michalski and H.-I. Lin, "On the far-zone electromagnetic field of a vertical Hertzian dipole over an imperfectly conducting half-space with extensions to plasmonics", en, *Radio Science*, vol. 52, no. 7, pp. 798–810, 2017. DOI: 10.1002/2017RS006299. (visited on 06/22/2020).

[50] K. A. Norton, "The Propagation of Radio Waves over the Surface of the Earth and in the Upper Atmosphere", *Proceedings of the Institute of Radio Engineers*, vol. 24, no. 10, pp. 1367–1387, Oct. 1936. DOI: 10.1109/JRPROC.1936.227360.

[51] P. R. Bannister, "Extension of finitely conducting earth-image-theory results to any range", Naval Underwater Systems Center New London Ct, Tech. Rep. NUSC-TR-6885, Jan. 1984. [Online]. Available: http://www.dtic.mil/docs/citations/ADA139144 (visited on 02/28/2017).

[52] C. A. Balanis, *Advanced Engineering Electromagnetics, 2nd Edition*. Wiley, 2012.

[53] J. R. Wait, "The Electromagnetic Fields of a Horizontal Dipole in the Presence of a Conducting Half-Space", *Canadian Journal of Physics*, vol. 39, no. 7, pp. 1017–1028, Jul. 1961. DOI: 10.1139/p61-111. (visited on 02/27/2017).

[54] *EMPIRE XPU Software*. [Online]. Available: http://www.empire.de.

[55] H. King, F. Shimabukuro, and J. Wong, "Characteristics of a tapered anechoic chamber", *IEEE Transactions on Antennas and Propagation*, vol. 15, no. 3, pp. 488–490, May 1967. DOI: 10.1109/TAP.1967.1138921.

[56] L. R. Francom and D. W. Jensen, "Three-dimensional iso-tross structure", US5921048A, Jul. 1999.

[57] A. Johansson, "Wireless Communication with Medical Implants: Antennas and Propagation", *Department of Electroscience, Lund University*, Jan. 2004.

[58] D. Andreuccetti, R. Fossi, and C. Petrucci, "An internet resource for the calculation of the dielectric properties of body tissues in the frequency range 10 hz - 100 ghz", IFAC-CNR, Florence (Italy), Tech. Rep., 1997. [Online]. Available: http://niremf.ifac.cnr.it/tissprop/.

[59] S. Castelló-Palacios, A. Vallés-Lluch, C. Garcia-Pardo, A. Fornes-Leal, and N. Cardona, "Formulas for easy-to-prepare tailored phantoms at 2.4 GHz ISM band", in *2017 11th International Symposium on Medical Information and Communication Technology (ISMICT)*, Feb. 2017, pp. 27–31. DOI: 10.1109/ISMICT.2017.7891760.

[60] P. R. Roberts and M. H. ElRefai, "The Use of App-based Follow-up of Cardiac Implantable Electronic Devices", *Cardiac Failure Review*, vol. 6, Apr. 2020. DOI: 10.15420/cfr.2019.13. (visited on 05/05/2021).

[61] D. Nikolayev, M. Zhadobov, and R. Sauleau, "Impact of tissue electromagnetic properties on radiation performance of in-body antennas", *IEEE Antennas and Wireless Propagation Letters*, vol. 17, no. 8, pp. 1440–1444, 2018. DOI: 10.1109/LAWP.2018.2848943.

[62] M. Barbi, C. Garcia-Pardo, A. Nevárez, V. Pons Beltrán, and N. Cardona, "UWB RSS-Based Localization for Capsule Endoscopy Using a Multilayer Phantom and In Vivo Measurements", *IEEE Transactions on Antennas and Propagation*, vol. 67, no. 8, pp. 5035–5043, Aug. 2019. DOI: 10.1109/TAP.2019.2916629.

[63] J. E. Hansen, *Spherical Near-field Antenna Measurements*. IET Digital Library, Jan. 1988. DOI: 10.1049/PBEW026E.

[64] R. J. Pirkl, "Spherical Wave Scattering Matrix Description of Antenna Coupling in Arbitrary Environments", *IEEE Transactions on Antennas and Propagation*, vol. 60, no. 12, pp. 5654–5662, Dec. 2012. DOI: 10.1109/TAP.2012.2211851.

[65] A. A. Glazunov, M. Gustafsson, A. F. Molisch, and F. Tufvesson, "Physical modelling of multiple-input multiple-output antennas and channels by means of the spherical vector wave expansion", en, *IET Microwaves, Antennas and Propagation*, vol. 4, no. 6, pp. 778–791, Jun. 2010. DOI: 10.1049/iet-map.2009.0057. (visited on 08/17/2021).

[66] X. G. Santiago, M. Hammerschmidt, S. Burger, C. Rockstuhl, I. Fernandez-Corbaton, and L. Zschiedrich, "Decomposition of scattered electromagnetic fields into vector spherical wave functions on surfaces with general shapes", eng, *Phys. Rev. B*, vol. 99, p. 045 406, 2019. DOI: 10.1103/PhysRevB.99.045406.

[67] E. Kiltz, "Complexity, theoretic lower bounds on cryptographic functions", Ph.D. dissertation, Ruhr-Universität Bochum, Universitätsbibliothek, 2004.

[68] M.-C. Tang, H. Wang, and R. W. Ziolkowski, "Design and Testing of Simple, Electrically Small, Low-Profile, Huygens Source Antennas With Broadside Radiation Performance", *IEEE Transactions on Antennas and Propagation*, vol. 64, no. 11, pp. 4607–4617, Nov. 2016. DOI: 10.1109/TAP.2016.2606552.

[69] P. R. Bannister, "New formulas that extend Norton's farfield elementary dipole equations to the quasi-nearfield range", Naval Underwater Systems Center New London Ct, Tech. Rep. NUSC-TR-6883, Jan. 1984. [Online]. Available: http://www.dtic.mil/docs/citations/ADA139057 (visited on 02/28/2017).

[70] A. Sommerfeld and F. Renner, "Strahlungsenergie und erdabsorption bei dipolantennen", *Annalen der Physik*, vol. 433, no. 1, pp. 1–36, 1942. DOI: 10.1002/andp.19424330102.

Appendix

A Definition of the On-Body Green's Functions

In the following the on-body Green's functions as discussed in Chapter 3.1.2 are listed. Here, the far-field approximation $|\gamma_0 R_1| \gg 1$ from [69] was used, which is sufficient for the necessary near-field to far-field transformation during the calculation of the on-body antenna parameters. The original solution for magnetic dipoles in [51] is based on the current loop representation $[m_l] = \mathrm{Am}^2$ which can be converted to magnetic current dipoles $[m] = \mathrm{Vm}$ with $m = j\omega\mu_0 m_l$. [52]. The complete version valid also in the near-field can be derived from the solutions in [51].

$$a_0 = \begin{cases} z - h & \text{if } h > 0, z > 0 \\ z & \text{if } h \leq 0, z > 0 \\ h & \text{if } h > 0, z \leq 0 \\ 0 & \text{if } h \leq 0, z \leq 0 \end{cases} \tag{A.1}$$

$$a_1 = \begin{cases} z + h & \text{if } h > 0 \\ z & \text{if } h \leq 0 \\ h & \text{if } h > 0, z \leq 0 \\ 0 & \text{if } h \leq 0, z \leq 0 \end{cases} \tag{A.2}$$

$$R_n = \sqrt{\rho^2 + a_n^2} \tag{A.3}$$

$$S_n = \sin(\psi_n) = \frac{a_n}{R_n} \tag{A.4}$$

$$C_n = \cos(\psi_n) = \frac{\rho}{R_n} \tag{A.5}$$

$$Q_n = \begin{cases} R_n^{-1} e^{-\gamma_0 R_n} & \text{if } h \geq 0, z \geq 0 \\ R_n^{-1} e^{-\gamma_0 R_n + \gamma_1 h} & \text{if } h < 0, z \geq 0 \\ R_n^{-1} e^{-\gamma_0 R_n + \gamma_1 z} & \text{if } h \geq 0, z < 0 \\ R_n^{-1} e^{-\gamma_0 R_n + \gamma_1 (h+z)} & \text{if } h < 0, z < 0 \end{cases} \tag{A.6}$$

$$A = \frac{1 + \Gamma_\perp}{2} + \frac{1 - \Gamma_\perp}{2} F(w) \tag{A.7}$$

$$k_\perp = \begin{cases} 1 & \text{if } h \geq 0 \\ \Delta_{\mathrm{m}}^2 & \text{if } h < 0, \end{cases} \tag{A.8}$$

$$k_z = \begin{cases} 1 & \text{if } z \geq 0 \\ \Delta_{\mathrm{m}}^2 & \text{if } z < 0, \end{cases} \tag{A.9}$$

Electric currents **J**:

$$G_{\mathrm{J},\parallel}^{\mathrm{E},\rho} = -S_0^2 Q_0 + \left[\Gamma_\perp S_1^2 + (1-\Gamma_\perp)\Delta_{\mathrm{m}}^2 F(w)\right] Q_1 \tag{A.10}$$

$$G_{\mathrm{J},\perp}^{\mathrm{E},\rho} = k_\perp S_0 C_0 Q_0 \tag{A.11}$$
$$+k_\perp \left[\Gamma_\perp S_1 - (1-\Gamma_\perp)\Delta_{\mathrm{m}} F(w)\right] C_1 Q_1$$

$$G_{\mathrm{J},\parallel}^{\mathrm{E},\phi} = Q_0 + \Big[-1 + \frac{2}{\gamma_0 n^2 R_1}(1 + A + \gamma_1 R_1 S_1)\Big] Q_1 \tag{A.12}$$

$$G_{\mathrm{J},\parallel}^{\mathrm{E},\mathrm{z}} = k_z S_0 C_0 Q_0 - k_z \left[\Gamma_\perp S_1 - (1-\Gamma_\perp)\Delta_{\mathrm{m}} F(w)\right] C_1 Q_1 \tag{A.13}$$

$$G_{\mathrm{J},\perp}^{\mathrm{E},\mathrm{z}} = -k_z k_\perp C_0^2 Q_0 - k_z k_\perp \left[\Gamma_\perp + (1-\Gamma_\perp) F(w)\right] C_1^2 Q_1 \tag{A.14}$$

Magnetic currents **M**

$$G_{\mathrm{M},\parallel}^{\mathrm{E},\rho} = S_0 Q_0 + \left[\Gamma_\perp S_1 - (1-\Gamma_\perp)\Delta_{\mathrm{m}} F(w)\right] Q_1 \tag{A.15}$$

$$G_{\mathrm{M},\parallel}^{\mathrm{E},\phi} = -S_0 Q_0$$
$$-\Big[S_1 + \frac{2}{n}\Big(S_1^2 - \frac{1}{\gamma_0 R_1}(1 + A - 3S_1^2)\Big)\Big] Q_1 \tag{A.16}$$

$$G_{\mathrm{M},\perp}^{\mathrm{E},\phi} = k_\perp C_0 Q_0 - k_\perp \Big[1 - \frac{2}{\gamma_0 n^2 R_1}(1 + \gamma_1 R_1 S_1)\Big] C_1 Q_1 \tag{A.17}$$

$$G_{\mathrm{M},\parallel}^{E,z} = k_z C_0 Q_0 + k_z \left[\Gamma_\perp + (1-\Gamma_\perp) F(w)\right] C_1 Q_1 \tag{A.18}$$

B Derivation of the On-Body Far-Field Region

In the following, the complete derivation of the far-field distance $\rho_{\Delta\Gamma}$ (3.20), ref. Chapter 3 is presented.

$$\Gamma_\perp = \frac{\sin(\psi_1) - \Delta_m}{\sin(\psi_1) + \Delta_m} \xrightarrow{\psi_1 \to 0} \Gamma_\perp \approx \frac{\psi_1 - \Delta_m}{\psi_1 + \Delta_m} \tag{B.1}$$

$$\Gamma_\perp \approx \frac{\psi_1 - \mathrm{Re}\{\Delta_m\} - j\mathrm{Im}\{\Delta_m\}}{\psi_1 + \mathrm{Re}\{\Delta_m\} + j\mathrm{Im}\{\Delta_m\}} \tag{B.2}$$

$$\arg\left\{\Gamma_\parallel(\rho_{\Delta\Gamma})\right\} \geq \frac{\pi}{2} \quad \text{if} \;\; \psi_1 < \mathrm{Re}\{\Delta_m\} \tag{B.3}$$

$$\psi_1 = \arctan\left(\frac{z+h}{\rho}\right) \xrightarrow{\rho \gg z+h} \psi_1 \approx \frac{z+h}{\rho} \tag{B.4}$$

$$\Delta_m = \frac{\gamma_0}{\gamma_1} = \frac{j\beta_0}{\alpha_1 + j\beta_1} \tag{B.5}$$

$$\mathrm{Re}\{\Delta_m\} = \frac{\beta_0\beta_1}{{\alpha_1}^2 + {\beta_1}^2} = \frac{|\gamma_0|}{{|\gamma_1|}^2}\beta_1 \tag{B.6}$$

$$\frac{|\gamma_0|}{{|\gamma_1|}^2}\beta_1 \approx \frac{{|\gamma_0|}^2}{{|\gamma_1|}^2}\sqrt{\varepsilon_{r,1}} = {|\Delta_m|}^2\sqrt{\varepsilon_{r,1}} \tag{B.7}$$

$$\psi_1 < \mathrm{Re}\{\Delta_m\} \rightarrow \frac{z+h}{\rho} \leq {|\Delta_m|}^2\sqrt{\varepsilon_{r,1}} \rightarrow \rho \geq \frac{z+h}{{|\Delta_m|}^2\sqrt{\varepsilon_{r,1}}} \tag{B.8}$$

C Relation: On-Body Antenna Effective Area - On-Body Gain

The derivation is based on the procedure for free-space according to [2] where it is shown that the effective area A_e of the isotropic antenna can be calculated from the ratio between gain and effective area of any other antenna. In the following, it is proved at the example of a normal Hertzian dipole above the tissue half-space that this relationship stays the same for the newly defined on-body gain according to (4.6).

Under the condition of maximum power transfer (conjugate matching) and a lossless antenna structure the effective area of a short dipole antenna can be calculated as:

$$A_\mathrm{e} = \frac{(E_\mathrm{i} \cdot l)^2}{8 W_\mathrm{i} R_\mathrm{r}}, \tag{C.1}$$

where E_i and W_i are the electric field strength and power density of the incoming wave. R_r is the antenna's radiation resistance, which depends on the dipole's length l and in the on-body case also on its height h above the tissue. A solution for this can be found in [70] as:

$$R_\mathrm{r} = \eta_0 \left(\frac{l}{\lambda}\right)^2 \cdot s(h), \tag{C.2}$$

with η_0 the impedance of free space, λ the wavelength and $s(h)$ the factor defining the dependency on the height h above the tissue. As evaluated in Chapter 3, in the on-body far-field the fields can locally be approximated by a plane wave. Thus, the incoming wave's power density becomes:

$$W_\mathrm{i} = \frac{E_\mathrm{i}^2}{2\eta_0}. \tag{C.3}$$

This reduces the expression for the on-body effective area of a normal Hertzian dipole to:

$$A_{\mathrm{e,B}} = \frac{\lambda^2}{4\pi s(h)}. \tag{C.4}$$

To calculate the on-body gain of the normal Hertzian dipole, its radiated E-field in the on-body far-field can be approximated by:

$$E = \frac{p\gamma_0\eta_0}{4\pi R} \cdot 2F(\rho). \tag{C.5}$$

The electric dipole moment p can be related to the accepted power P_{in} using the relationships in [70] as:

$$p = \omega\sqrt{\frac{P_{\mathrm{in}}8\pi\varepsilon_0}{c_0\gamma_0^4 s(h)}}. \tag{C.6}$$

According to (4.4) this leads to the on-body gain of a normal Hertzian dipole as:

$$G_{\mathrm{B}} = s^{-1}(h). \tag{C.7}$$

Finally, the effective area of the isotropic antenna (4.6) for the derived on-body antenna parameters is calculated as the ratio between the effective area (C.4) and gain (C.7) of the Hertzian dipole.

D Definition of the Spherical Wave Functions

The spherical wave function (SWF) $\mathbf{F}_j^{(c)}$ are defined in a spherical coordinate system (ρ,ϕ,θ) in dependence of the running index j[19] and the order c as [63]:[20]

$$\mathbf{F}_{1,m,n}^{(c)}(\mathbf{r}) = \frac{1}{2\sqrt{\pi}} \frac{1}{\sqrt{n(n+1)}} \left(-\frac{m}{|m|}\right)^m z_n^{(c)}(k_0\rho) e^{jm\phi} \left\{ \frac{jm\overline{P}_n^{|m|}(\cos\theta)}{\sin\theta} \mathbf{e}_\theta - \frac{\mathrm{d}\overline{P}_n^{|m|}(\cos\theta)}{\mathrm{d}\theta} \mathbf{e}_\phi \right\} \tag{D.1}$$

and

$$\begin{aligned} \mathbf{F}_{2,m,n}^{(c)}(\mathbf{r}) = & \frac{1}{2\sqrt{\pi}} \frac{1}{\sqrt{n(n+1)}} \left(-\frac{m}{|m|}\right)^m e^{jm\phi} \\ & \cdot \left\{ n(n+1) \frac{z_n^{(c)}(k_0\rho)}{k_0\rho} \overline{P}_n^{|m|}(\cos\theta) \mathbf{e}_\rho \right. \\ & \left. + w_n^{(c)}(k_0\rho) \left(\frac{\mathrm{d}\overline{P}_n^{|m|}(\cos\theta)}{\mathrm{d}\theta} \mathbf{e}_\theta + \frac{jm\overline{P}_n^{|m|}(\cos\theta)}{\sin\theta} \mathbf{e}_\phi \right) \right\}, \end{aligned} \tag{D.2}$$

where the multi-index j is resolved to three single indices n, m, s.

This is done through the relations:

$$j = 2(n(n+1) + m - 1) + s, \tag{D.3}$$

$$n \in \mathbb{N}, \tag{D.4}$$

[19] The variable j is used here both as a running index (to remain compatible with the literature) and as the imaginary unit. As the index only occurs in subscripts, keeping them separate is possible.

[20] In contrast to [63], the time-dependence $e^{j\omega t}$ is assumed here.

$$m \in \{-n, ..., -1, 0, 1, ...n\}, \tag{D.5}$$

and

$$s \in \{1, 2\}. \tag{D.6}$$

Finally, the radial dependencies are defined containing the spherical Bessel (J), Neumann (Y) or Hankel (H) functions of the first and second order as:

$$z_n^{(1)}(k\rho) = j_n(k\rho) = \sqrt{\frac{\pi}{2k\rho}} J_{n+1/2}(k\rho) \tag{D.7}$$

$$z_n^{(2)}(k\rho) = y_n(k\rho) = \sqrt{\frac{\pi}{2k\rho}} Y_{n+1/2}(k\rho) \tag{D.8}$$

$$z_n^{(3)}(k\rho) = h_n^{(1)}(k\rho) = \sqrt{\frac{\pi}{2k\rho}} H_{n+1/2}^{(1)}(k\rho) \tag{D.9}$$

$$z_n^{(4)}(k\rho) = h_n^{(2)}(k\rho) = \sqrt{\frac{\pi}{2k\rho}} H_{n+1/2}^{(2)}(k\rho) \tag{D.10}$$

$$w_n^{(c)}(k\rho) = \frac{1}{k\rho} \frac{\mathrm{d}}{\mathrm{d}(k\rho)} \{k\rho z_n^{(c)}(k\rho)\}. \tag{D.11}$$

E SWF Radial Cut-Off / Mode Truncation

The radial cut-off property of the SWF can be interpreted by visualizing the radiation as taking place in a spherical waveguide [63]. The waveguide extends from the radius of the minimum sphere circumscribing the antenna ρ_0 to infinity. Other than with a conventional waveguide, the cross-section of the spherical waveguide increases with ρ. Hence, more and more spherical modes may propagate if ρ increases. If various modes excited by the antenna at ρ_0 are assumed to have the same order of magnitude, it can be observed that all modes with $n > k\rho_0$ are heavily attenuated with increasing ρ. This is also visualized in Fig. 6.1 where the amplitude of the Hankel function $h_n^{(1)}(k\rho)$, as an example for the radial dependency of the SWF (ref. D), is depicted in dependency of $k\rho$ and for different n. In Fig. 6.1(a) the graphs where normalized to 0 dB at $k\rho_0 = 10$. As can be seen, the function with $n = 20$ is attenuated by about 80 dB compared to the one with $n = 5$ for increasing distances $k\rho$. However, if the normalization is performed at $k\rho_0 = 100$ as depicted in Fig. 6.1(b) the function with $n = 20$ compared to the one with $n = 5$ stays at the same order of magnitude. Thus, in dependency of the minimum sphere ρ_0 modes above a certain boundary can be neglected for SWF decomposition in (5.1).

For free-space propagation, the boundary for the mode truncation can be estimated by the empirical rule [63]:

$$N = [k\rho_0] + n_1, \tag{E.1}$$

where ρ_0 is the radius of the minimum sphere enclosing the antenna structure, and n_1 an empirical factor that depends on the location of the coordinate system and the accuracy required. The square brackets indicate the largest integer smaller than or equal to $k\rho_0$. N is the maximum order of the spherical Bessel, or Hankel

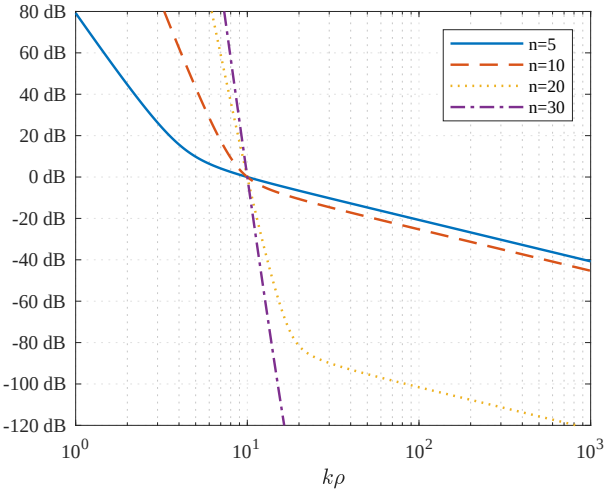

(a)

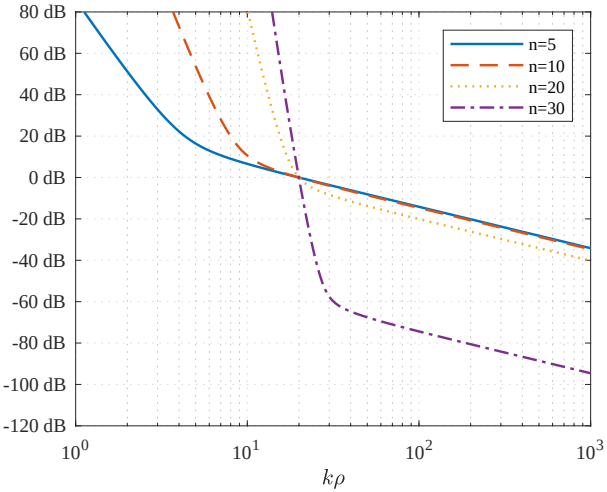

(b)

Figure 6.1: Amplitude variation of $h_n^{(1)}(k\rho)$: (a) normalized at $k\rho_0 = 10$; (b) normalized at $k\rho_0 = 20$ [63].

functions. The number of associated modes in (5.1) is calculated as:

$$J = 2N(N + 2). \tag{E.2}$$

With on-body propagation, the validity of the rule is reduced due to the near-field coupling with the tissue. Therefore, an adaptive convergence check has been introduced as described in Chapter 5.4.4.

Curriculum Vitae

Academic Education

01/2017-01/2022	Leibniz University Hannover Ph.D. Electrical Engineering and Information Technology
10/2014-12/2016	Leibniz University Hannover M.Sc. Electrical Engineering and Information Technology Thesis: „Investigation of Load Mismatch for an Efficient Power Amplifier and Implementation of an Adaptive Matching Network to Compensate“
10/2011-12/2014	Leibniz University Hannover B.Sc. Electrical Engineering and Information Technology Thesis: „Development and Evaluation of an Amplifier Unit for Active GPS Antennas to be Integrated in Automotive Installation Spaces Using 3D-MID Technology“

Work Experience

Since 02/2022	Volkswagen AG Antenna Development Development Engineer
01/2017-01/2022	Leibniz University Hannover Institute of Microwave and Wireless Systems Research Associate
01/2013-12/2016	Leibniz University Hannover Institute of Electrical Engineering and Measurement Technology Student Assistant
05/2014-06/2016	Leibniz University Hannover Institute of Microwave and Wireless Systems Student Assistant
10/2015-02/2016	Rosenberger Hochfrequenztechnik Internship

Publications

Journal articles

L. Berkelmann, H. Jäschke, L. Mörlein, L. Grundmann and D. Manteuffel: „Antenna Optimization for WBAN Based on Spherical Wave Functions De-Embedding," *IEEE Transactions on Antennas and Propagation*, 2022

L. Berkelmann and D. Manteuffel: „Antenna Parameters for On-Body Communications with Wearable and Implantable Antennas," *IEEE Transactions on Antennas and Propagation*, 2021

L. Berkelmann and D. Manteuffel: „Characterization of Wearable and Implanted Antennas: Test Procedure and Range Design," *IEEE Transactions on Antennas and Propagation*, 2021

L. Berkelmann, A. Bader, S. Meshksar, A. Dierks, G. Hatipoglu Majernik, J. K. Krauss, K. Schwabe, D. Manteuffel, A. Ngezahayo: „Tumour-treating fields (TTFields): Investigations on the mechanism of action by electromagnetic exposure of cells in telophase/cytokinesis," *Scientific Reports, Volume 9, Article number: 7362*, 2019

Conference papers

L. Mörlein, L. Berkelmann and D. Manteuffel: „Antenna De-Embedding in FDTD Using Spherical Wave Functions by Exploiting Orthogonality," *2022 16th European Conference on Antennas and Propagation (EuCAP 2022)*

L. Berkelmann and D. Manteuffel: „Implantable Antenna Design for Surface-Wave Based In-Body to On-Body Communication," *2021 IEEE International Symposium on Antennas and Propagation and USNC-URSI Radio Science Meeting - (AP-S/URSI 2021)*

L. Berkelmann and D. Manteuffel: „On-Body Antenna Radiation Pattern Measurement," *International Conference on Electromagnetics in Advanced Applications (ICEAA 2021)*

S. Harke, L. Berkelmann, A. Ngezahayo and D. Manteuffel: „In-Vitro Exposure Setup for Tumor Treating Fields," *2020 IEEE International Engineering in Medicine and Biology Conference (EMBC 2020)*

L. Berkelmann and D. Manteuffel: „Slot Antenna Design with Optimized On-Body Pattern for Eyewear Applications," *2019 IEEE International Symposium on Antennas and Propagation and USNC-URSI Radio Science Meeting - (AP-S/URSI 2019)*

S. Meshksar, L. Berkelmann and D. Manteuffel: „Evaluation of Bannisters Subsurface-to-Air Model for Implanted Antennas," *2019 IEEE International Symposium on Antennas and Propagation and USNC-URSI Radio Science Meeting (AP-S/URSI 2019)*

L. Berkelmann, A. Bader, S. Meshksar, A. Ngezahayo and D. Manteuffel: „In Vitro Exposure System for Tumor Treating Fields," *2019 IEEE International Engineering in Medicine and Biology Conference (EMBC 2019)*

L. Berkelmann, T Martinelli, A Friedrich and D. Manteuffel: „Design and Integration of a Wearable Antenna System for On- and Off-Body Communication Based on 3D-MID Technology," *2018 12th European Conference on Antennas and Propagation (EUCAP 2018)*

S. Probst, L. Berkelmann, B. Lüers, B. Geck, D. Manteuffel: „Investigation of the Dynamic Load Modulation of an Inverse Class-F Power Amplifier with an Adaptive Matching Network," *2018 IEEE Radio & Wireless Week (RWW), Power Amplifiers for Radio and Wireless Applications (PAWR)*, 2018

A. Friedrich, L. Berkelmann, T. Martinelli, B. Geck, O. Klemp, I. Kriebitzsch: „Active Three-Dimensional GPS Patch Antenna Using MID-Technology," *European Microwave Conference 2015 (EuMC 2015)*

Patents

C. Grabowski, A. Pfrommer, L. Berkelmann, D. Manteuffel: „Circuit board for a hearing aid," *DE102019219484, EP3836565, US20210185461, applicant: Sivantos Pte. Ltd.*, 2021